NOTE TO USERS

Page(s) not included in the original manuscript and are unavailable from the author or university. The manuscript was scanned as received.

193

This reproduction is the best copy available.

UMI®

DISSERTATION

OPTOFLUIDIC INTRACAVITY SPECTROSCOPIC BIOSENSING SYSTEM FOR SINGLE CELL IDENTIFICATION

Submitted by

Hua Shao

Electrical and Computer Engineering Department

In partial fulfillment of the requirements

For the Degree of Doctor of Philosophy

Colorado State University

Fort Collins, Colorado

Fall 2007

COLORADO STATE UNIVERSITY

October 31, 2007

WE HEREBY RECOMMEND THAT THE DISSERTATION PREPARED UNDER OUR SUPERVISION BY HUA SHAO ENTITLED OPTOFLUIDIC INTRACAVITY SPECTROSCOPIC BIOSENSING SYSTEM FOR SINGLE CELL IDENTIFICATION BE ACCEPTED AS FULFILLING IN PART REQUIREMENTS FOR THE DEGREE OF DOCTOR OF PHILOSOPHY.

Committee on Graduate Work

Adviser

Department Head

ABSTRACT OF THE DISSERTATION

OPTOFLUIDIC INTRACAVITY SPECTROSCOPIC BIOSENSING SYSTEM

FOR SINGLE CELL IDENTIFICATION

Low cost and label-free identification of single biological cells is of broad interest in a variety of fields, including clinical diagnostics, drug discovery, food safety, environmental monitoring, biology, and homeland security. The goal of this dissertation is to develop a low-cost biosensing system for label-free identification of single biological cells by combining optical and microfluidic techniques. Optical refraction of cells is closely related to cell size, shape, type, and biological states, providing sensitive probes for cell identification. Biological cells inside an optofluidic cavity modify the optical cavity modes, providing a probe for optical properties of the cells that can be used for cell differentiation. In this work, the perturbation effects on an optofluidic cavity transmission spectra induced by cells due to their larger refractive indices than the surrounding media were investigated.

Passive optofluidic plane-plane Fabry-Pérot (FP) cavities fabricated on Pyrex glass substrates with a low temperature thermocompressive gold-to-gold diffusion bonding technique were used in the spectroscopic experiments. Complete fabrication processes for gold-patterned optofluidic cavities with HfO_2/SiO_2 dielectric mirrors using low cost transparency photomasks were developed and characterized. Critical fabrication steps that affect the optofluidic cavity's performance were examined by scanning electron microscopy, atomic force microscopy, and optical spectroscopy. Theoretical modeling of cavity finesse reduction due to mirror roughness and tilt shows good agreement with the measured value. An optofluidic cavity with a cavity finesse of above 40 and a mirror tilt $<1^0$ was demonstrated.

A customized microscopic system was designed to measure the transmission spectra of the optofluidic cavity. Transmission spectra taken from various microspheres and biological cells excited by an LED at 890 nm are quantitatively different in terms of the number, relative position, and relative wavelength offsets of transverse modes that can be use for cell recognition. For example, intracavity transmission spectra of canine lymphoma cells are distinct from noncancerous lymphocytes, indicating the potential of this technique for cancer detection. The amount of transverse mode shift with respect to the bare cavity mode provides useful information on the refractive indices of cells that are important for cell differentiation. High order transverse modes induced by the transverse optical confinement of spheres and cells were found to be more effectively excited with tilted illuminations.

Experiments were complemented by theoretical modeling of the transmission spectra of a cell-loaded FP cavity. Both the longitudinal optical path length change and the lateral optical confinements were thoroughly studied. Paraxial Gaussian beam resonator analysis provides insightful understanding of the effects of cavity length on resonator stability and transverse mode spacing. The range of cavity lengths for stable operation was found and should be considered in sensor design. Analysis of transverse mode spacing due to Guoy phase shift again indicated that a short cavity length would minimize transverse mode spacing variation with the longitudinal positions of the cell. A simplified double homogenous sphere model for cancerous cells was developed to study the spectral changes induced by the nuclei, which are important factors in pre-cancerous detection. The effective index method allows extraction of refractive index and nuclear size relationships from wavelength shifts and shows the impact of transverse mode confinement. Theoretical extraction from the experimental spectra indicates that the nuclei of cancerous cells are larger than those of normal ones. However, full numerical modeling based on the finite-difference time-domain (FDTD) method using commercial software did not produce consistent results.

Two different fluid flow control mechanisms were explored to stabilize cells and microspheres within the microfluidic cavity. Pressure driven flow allows a simple microfluidic system to be used while dielectrophoretic (DEP) trapping with electrical fields allows cell immobilization in a more controllable way. Square well shaped dielectrophoretic traps were integrated onto the microfluidic chip by patterning ~10μm wide gold electrodes using a transparency mask. DEP trapping of various types of single microspheres and cells within optofluidic cavities was demonstrated with a 16 MHz, 10 Vpp AC voltage. Effects of DEP trapping on the bare cavity spectra were investigated by varying the AC voltages applied between the microelectrodes. The experimental results indicated that thermal effect was the major factor that caused a red shift of the bare cavity modes with an increase in trapping voltage. Future work is suggested including burying gold microelectrodes beneath the dielectric coatings to reduce the bio-contamination of the electrodes and investigating spectroscopic properties of DEP trapped biological cells.

In summary, the biosensing system developed in this work may provide a low-cost, label-free optical technique for recognizing cells in a microfluidic environment.

Hua Shao
Electrical and Computer Engineering Department
Colorado State University
Fort Collins, CO 80523
Fall 2007

TABLE OF CONTENTS

Chapter 1

Introduction

This dissertation describes the development of optofluidic intracavity spectroscopy for single cell detection. This technique identifies and differentiates single biological cells within a Fabry-Pérot (FP) cavity by passing the cell through the fluidic channels and measuring the transmission spectrum of the cell.

This chapter begins with an introduction to the motivation of the project. This will lead to the introduction of the overall project goal, an optofluidic intracavity spectroscopic (OFIS) biosensing system for probing the spectroscopic features of many types of single cells. A brief overview of the spectroscopic features of cells within an optofluidic FP cavity and an outline of the rest of the dissertation will conclude the chapter.

1.1 Motivation

Photonic biological and chemical sensors have become critical components in optical information system applications in medicine, environmental monitoring, and security. The use of biosensors in the detection of toxins, bacteria or virus and fighting against the dangers posed by chemical and biological terrorism is of great interest. Biosensors thus find a wide range of applications in:

- Clinical diagnosis (e.g. blood glucose monitoring)
- Pharmaceutical and drug screening
- Bioprocess monitoring (e.g. fermentation in-situ monitoring)

- Environmental screening and monitoring (e.g. air, water, and soil pollution)
- Food and beverage quality industry (e.g. fish freshness assay)
- Farm, garden, and veterinary analysis (e.g. pesticide usage control)
- Homeland security

Optical effects provide plentiful information of the biological cells. The effective refractive index of a cell is a function of its size, shape, and intracellular components and can be used to measure its biological state [1]. For example, an enlarged nucleus has been used as an indication for pre-cancer in clinical diagnosis [2]. Conventional microscopic imaging can determine nuclear size but requires the use of stains to enhance contrast of the chromatin. Flow cytometry is another traditional technology that simultaneously measures and then analyzes multiple physical characteristics of single particles, usually cells, as they flow in a fluid stream through a beam of light. Since different cell types can be distinguished by quantitating structural features, flow cytometry can also be used to count cells of different types in a mixture. However, flow cytometry relies either on fluorescent labeling reagents or angle resolved scattering to differentiate cells, it is relatively expensive ($\geq$\$100,000) and also require certain professional skills to operate. Therefore, developing low cost and label-free cell identification sensing systems will greatly reduce the system cost of the current commercially available flow cytometers.

Biological cells inside an optical resonator modify the cavity modes, providing a probe for optical properties of the cells and their nuclei that can be used for cell recognition. Previous work on single cell detection using optical resonators includes the biocavity laser based biosensor developed by P. L. Gourley [3] and the electrically

injected fluidic laser diode (FILD) based biosensor developed in our group [4]. However, the fabrication of such active optical resonator based sensors is challenging, requiring high gain to overcome the loss induced by the cell in order to reach threshold. This work is motivated by the benefits of a passive cavity interferometric system that retains mode spectrum dependence on cells in a resonator but does not require laser gain media inside the cavity. Instead, transmission spectra are obtained by illuminating the passive cavity system with an external continuum light source such as an LED or bright incandescent lamp easing the requirements on cavity finesse and loss. The passive cavity based intracavity spectroscopic biosensor is also expected to simplify the analysis of cell induced transverse mode spectral changes by eliminating the complexities associated with an active laser cavity such as mode confinement factors, material gain, and various losses.

1.2 Organization of the dissertation

This project is focused on integrating optical detection with microfluidics, thereby realizing non-destructive, label-free, on-chip detection of single biological cells in a fluidic environment. Biological cells inside an optofluidic cavity modify the optical cavity modes, providing probes for optical properties of the cells that can be used to detect and differentiate single cells. The biosensing system developed in this work utilizes optical refraction and diffraction effects to produce characteristic intracavity transmission spectra of single biological cells in an optical resonator.

An optofluidic intracavity spectroscopic (OFIS) biosensor has been designed and fabricated on glass wafers, and was illuminated by an external broadband LED or

incandescent source to excite the transmission spectrum of the fluidic Fabry-Pérot cavity. Theoretical modeling as well as experimental work was used to design and characterize the biosensors. Experimental results on different types of biological cells and standard microspheres are presented. Effects of the lateral optical confinement of cancerous cells within passive microfluidic Fabry-Pérot cavities were investigated. Different theoretical models were developed and compared with the experimental results in an attempt to better understand and confirm the experimental work.

1.3 Overview of the report

In order to give the reader a basic understanding of biosensors, background information on general biosensors, including a literature review on single cell detection techniques, single micrometer sized particle on-chip trapping, and microfluidic device sealing techniques, will be presented in Chapter 2. This is followed by a background introduction of the fundamental physics of Fabry-Pérot interferometers, a literature review of intracavity spectroscopic techniques, and a brief introduction of the sensing concept of OFIS in Chapter 3. Physics of intracavity single cell spectroscopic detection will be discussed in this chapter together with factors influencing the sensitivity of the technique such as mirror surface roughness and parallelism, and beam collimation. A complete device fabrication process and characterization of the optofluidic cavities will be described in Chapter 4. The optical experimental setup, spectra of single standard microspheres and biological cells will be presented in Chapter 5. To confirm the experimental results, theoretical analysis and computer simulations of the modal calculations of the microfluidic biosensors have been done and are discussed in detail in

Chapter 6. Lastly, a brief summary of the contributions regarding the presented work and suggestions for future research work concludes the dissertation.

References

[1] J. Beuthan, O. Minet, J. Helfmann, M. Herrig, and G. Muller, "The spatial variation of the refractive index in biological cells", *Phys. in Medicine and Biology*, vol. 41, no. 3, pp. 369, 1996.

[2] V. Backman, M. B. Wallace, and L. T. Arendt, "Detection of preinvasive cancer cells", *Nature*, vol. 406, pp. 35, 2000.

[3] P. L. Gourley and A. E. McDonald, "Semiconductor microlasers with intracavity microfluidics for biomedical application", *Proc. SPIE 2978*, pg. 186-196, 1997.

[4] D. Kumar, H. Shao, and K. L. Lear, "Microfluidic cavity surface emitting laser based biosensor", *IEEE LEOS 17th Annual Meeting*, vol. 1, pp.118–119, November 7-11, 2004.

Chapter 2

Background

This chapter begins with an introduction of biosensing technology followed by a literature review of micrometer sized bioparticle detection including both non-optical and optical techniques. Since optical properties of cells consist in large part of the spectroscopy, the relationship between cellular structure and their optical properties will also be presented. Flow cytometry is a commercially available technique that has been widely used to sort and detect biological cells. Therefore, a brief introduction of flow cytometry will be presented in this chapter to familiarize readers with this important cell detection technique. An important aspect of cell identification is fluidic flow control, which affects the detection speed and the capability of on-chip cell positioning. Some commonly used cell trapping techniques, such as optical trapping, dielectrophoretic trapping, and optoelectronic trapping, will be introduced to help improve the overall sensor performance. Device sealing is critical for both fluidic flow control and the optical quality of the Fabry-Pérot (FP) cavities since the spectral resolution of the cavity is highly dependent on the etalon's parallelism, requiring strong bonding. The last part of this chapter focuses on an overview of microfluidic device sealing techniques.

2.1 General biosensor background

In the past two decades, the biological and medical fields have seen great advances in the development of biosensors. Biosensors are analytical devices that can detect chemical or biological species or a microorganism or directly monitor a bioprocess and

provide either qualitative or quantitative results about an analyte. The basic components of a biosensor are bio-recognition elements and physico-transducers. Combined, these form a biotransducer. Some important components of biosensors are discussed in the following paragraphs.

2.1.1 Bio-recognition elements

The bio-recognition elements are biological organisms such as enzymes, antibodies, nucleic acids, bacteria, single cell organisms or even whole tissues of higher organisms. They are often immobilized to increase their local concentration near an optical sensing element and to allow them to be reused. Some of the molecular bioreceptors used for biorecognition in biosensitization are described here.

Enzymes: Enzymes are microorganisms that selectively catalyze with specific reactants or antigens and thus provide selectivity in terms of biorecognition. In addition, the reaction of certain analytes/substrates with enzymes can also provide optical transduction by producing a product that absorbs at a different wavelength (change in absorption), or is fluorescent (fluorescence sensor).

Antibodies: Antibodies are proteins that selectively bind with an antigen or analyte because of their geometric (site) compatibility. Very often an antibody-antigen pair's selective association in terms of their conformational compatibility is represented as a lock (antibody) and key (antigen) combination. This specific physical association can

also produce an optical response that can be intrinsic such as a change in the optical property of the antibody or the antigen.

2.1.2 Physico-transducer

In general, transducers take many forms and dictate the physicochemical parameters that will be measured. Thus, the transducer may be optically-based, measuring such changes as optical absorption, fluorescence, or refractive index. It may be mass-based, measuring the change in mass that accompanies a biologically derived binding reaction. Additionally, it may be thermally based (measuring the change in enthalpy), heat or impedance based (measuring the change in electrical properties that accompanies the analyte/bio-recognition layer interaction) [1].

2.1.3 Issues in biosensor technology

Properly designed and manufactured, biosensor devices may be conveniently mass-produced. The potential lower cost per test is a compelling advantage over conventional flow cytometry. While detection limit and sensitivity are often cited as important impediments to success, issues in biosensor technology are (i) time-dependent stability of the bio-recognition layer, (ii) reproducibility of the activity of the bio-recognition layer, (iii) vulnerability of the biotransducer to fouling and interferences, (iv) market sizes for biosensor-based measurement devices, and (v) appropriateness of the recognition/transduction device and form-factor of the integrated system to the targeted market [1].

2.1.4 Future directions in biosensor technology

Future directions in biosensor technology are (i) increased range of analytes addressed, (ii) movement towards completely integrated systems possessing sample handling, microfluidics, detection and display (possibly telemetry), (iii) renewed emphasis on whole cell and tissue biosensors, (iv) use of embedded systems, and (v) telecommunications capability.

Gaining the fundamental knowledge of the general types of biosensors, we are going to focus our attention on the biosensors that are designed specifically for single cell identification in the following sections.

2.2 Literature review of single cell identification

Rapid detection of single cells is of broad interest in a variety of fields, including molecular biology, medicine, national security, and environmental monitoring. Unfortunately, analysis of single cells is an often-difficult process from a technical perspective. At the present time, most studies tend to be focused on multiple cells, where averages from populations are correlated to behaviors, gene expressions, and processes of interest. Multiple-cell measurements are more compatible with the limitations of existing instrumentation technology. However, the need for a wide variety of sensing and measurement techniques to analyze cells at a single-cell level is more and more in demand in the biological research community.

Several techniques including mass-sensitive mechanical metrology [2] and fluorescence spectroscopy [3] have been used for single cell recognition, but these involve expensive equipment or time-consuming sample preparation. Over the past few

years, the analysis of living cells with the use of micro-fabricated structures attracted increased attention. Extensive review of the latest single cell identification techniques can be found in reference [4-6]. The following sections talk about cellular structures and prior work in single cell detection.

2.2.1 Cellular structures

Biological cells are essentially an assembly of molecules where water, amino acids, carbohydrates (sugar), fatty acids, and ions account for 75-80% of the matter in cells. The remainder of cell mass is accounted for by macromolecules, also called polymers, which include peptides/proteins, polysaccharides, DNA, RNA, and phospholipids. These macromolecular polymers organize to form cells. To contain these molecules, a semi-permeable membrane surrounds them to form a cell.

The structure of a cell can be described in terms of various subcellular compartments and the constituent chemical species they contain. The main structural components of a cell are:

- Plasma membrane, which defenses the outer boundary of a cell. This is present in all cells.
- Cell wall, which exists in the prokaryotic cells as well as in the eukaryotic cells of plants but not animals.
- Cytoplasm, which represents everything within a cell, except the nucleus.
- Cytosol, which is the fluid of the cytoplasm.
- Organelle, which is the name used for a sub cellular compartment in a cell where a specific cellular function takes place.

- Nucleus, which contains the chromosomes (genetic information).

Cells come in many shapes, sizes, and compositions. There are more than 200 different types of cells present in the human body. The common types are epithelial cells, which form the lining on the inner surfaces of the body; blood cells present in blood; nerve cells, which are responsible for communication within the body; sensory cells, which detect sound and light; germ cells, which are responsible for cell reproduction; and stem cells, which are cells waiting to be assigned functions.

Various sensing mechanisms have been developed to detect single cells based on the differences in cellular structures discussed above. Table 2.1 lists some of the techniques and the corresponding sensing mechanisms. In the following sections, the review of prior work on the single cell detections will be presented in two different categories, the non-optical methods and the optical methods.

Table 2.1 Summary of single cell detection techniques.

Method	Mechanism	Cell type	Year	Properties
Electrochemical	chemical properties	wheat callus cells	2005 [1]	destructive type analyte consumption
Mechanical oscillator	mass	E. Coli	2004 [2]	needs modeling time-consuming
Light addressable potentiometer	pH, ion exchange, chemical components	rat Cortical cells	2005 [3]	optical probing surface treatment
Raman spectroscopy	chemical components	RBC	2003 [4]	time-consuming
Cavity ring-down spectroscopy	absorption	mammalian cells	2004 [5]	surface treatment optical imaging
Fluorescence spectroscopy	size, shape chemical components	RBCs	2003 [6]	labeling time-consuming
Intracavity spectroscopy	size, shape, and refractive index	blood cells	1997 [7]	complicated device fabrication
Thermal lens spectroscopy	absorption chemical components	cyto-chrome c	2002 [8]	optical scanning/imaging

2.2.2 Non-optical methods for single cell detection

2.2.2.1 Mass spectrometry

A mass spectrometer ionizes the sample inside the spectrometer and analyzes the motion of the various ions in an electric field to sort them out by their mass-to-charge ratios. The basic principle of mass spectroscopy is that isotopes of different masses move differently in a given electromagnetic field. Mass spectroscopy has been successfully used for real-time analysis of individual bioaerosol particles. For example, D. P. Fergenson *et al.* developed a mass spectrometry-based analytical technique, bioaerosol mass *s*pectrometry (BAMS), which has the potential to instantaneously detect species-level differences between single cells without the need for reagents, offering a high degree of detection specificity combined with both single-cell sensitivity and millisecond analysis times [7]. They characterized the mass spectral signature of individual Bacillus spore species, B. thuringiensis and B. atrophaeus, from one another very accurately and from the other biological cells.

2.2.2.2 Micromechanical oscillator sensor

Engineered micro-systems can serve as multifunctional, highly sensitive, immunospecific biological detectors. The micromechanical oscillator sensor detects single cells by measuring the oscillator resonant frequency shift due to the additional mass of the attached cells. A resonant frequency-based mass sensor comprised of low-stress silicon nitride cantilever beams for the detection of Escherichia coli (*E. coli*)-cell-antibody binding events with detection sensitivity down to a single cell has been demonstrated by B. Ilic *et al.* [2]. Figure 2.1 shows a SEM photograph of a single *E.*

coli cell bound to the antibody layer on top of the oscillator they designed and the corresponding vibration spectra of the cantilever.

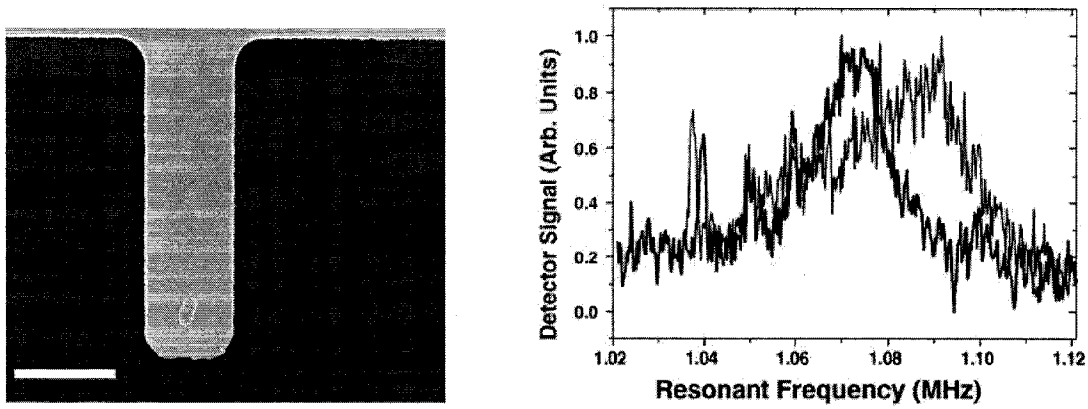

(a) (b)

Figure 2.1 (a) SEM photograph of a single *E. coli* cell bound to an immobilized antibody layer on top of the oscillator. (b) The corresponding transverse vibration spectra of the cantilever due to the thermal and ambient noise before and after antibody immobilization and single cell attachment. (Reproduced from Reference [2])

2.2.2.3 Electrochemical methods

Electrochemical biosensors have been the subject of research for a number of decades, with the vast majority of devices consisting of enzymes coupled to an electrode. The basic operating principle behind an electrochemical sensor relies on the transfer of electrons between an electrode and a chemical redox (oxidation-reduction) reaction. To detect single cells and cell populations, the size of the sensing electrode must be at most a few micrometers in size. One of the main disadvantages of electrochemical cells for single cell detection is that analyte is consumed. Two examples of cell detection with electrochemical biosensors are discussed in the following paragraphs.

Electrophoresis is one type of electrochemical method, which is a useful tool for single cell detection. As most cells have a net negative charge at neutral pH, electrical fields can be used to move individual cells in microfluidic systems. When applying an electrical field across a thin membrane containing a microspore, cells will be automatically transported towards the pore and will stick there. This enables the localization of single cells on top of the pore, where they can be analyzed using patch-clamping techniques. A good review of prior work in single cell analysis by capillary electrophoresis can be found in the paper written by J. N. Stuart and J. V. Sweedler [8].

Electrochemical detection (ED) coupled with capillary electrophoresis (CE) is also an important detection technique for single cell analysis, because it offers high sensitivity and selectivity for analyses. F. Xia *et al.* developed a novel electrochemical method using a microfluidic device [9]. In their work, cell injection, loading and lysis, and electrokinetic transportation and detection of intracellular species were integrated in a microfluidic chip with a double-T injector coupled with an end-channel amperometric detector. Figure 2.2 shows the schematic diagram of the CE-chip fabricated in soda-lime glass substrates. A single cell was loaded at the double-T injector on the microfluidic chip by using an electric field. Then, the docked cell was lysed by a direct current electric field with strength of 220 V/cm. The analyte of interest inside the cell was electro-kinetically transported to the detection end of separation channel and was electrochemically detected. External standardization was used to quantify the analyte of interest in individual cells. Ascorbic acid (AA) in single wheat callus cells was chosen as the model compound. AA could be directly detected at a carbon fiber disk bundle electrode.

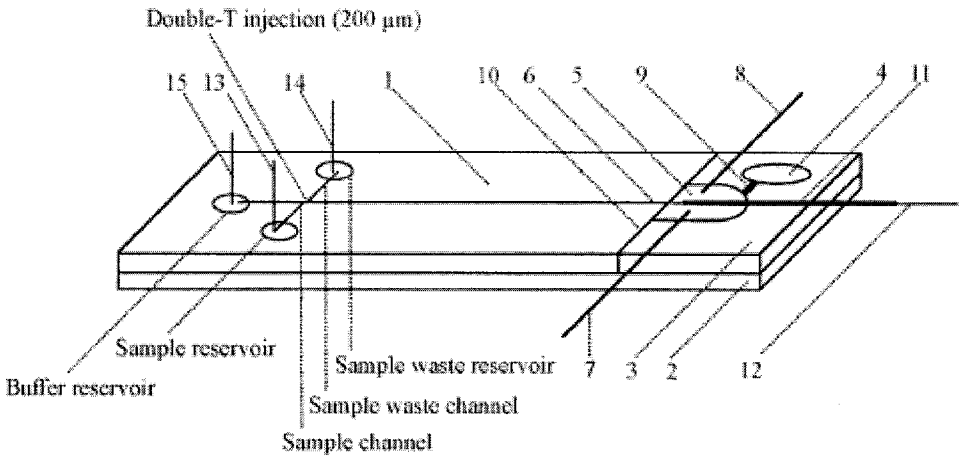

Figure 2.2 Microfluidic chip-ED system: (1) microfluidic chip; (2) microscope slide; (3) Plexiglas plate; (4) reference electrode port; (5) electrochemical cell and waste reservoir; (6) separation channel; (7) auxiliary electrode; (8) cathode of separation high voltage; (9) magnesia rod; (10) paraffin; (11) stainless steel tube; (12) working electrode; (13) anode of loading voltage; (14), cathode of loading voltage; (15), anode of separation high voltage. Channel, 30-μm depth and 80-μm width; separation channel, 45-mm length. Both sample channel and sample waste channel, 5-mm length. (Reproduced from reference [9])

2.2.2.4 Solid-state approaches

The underlying sensing principle of solid-state approaches relies on the change in the surface charge of the gate, which changes the gate voltage and modifies the operating characteristics of the field-effect transistor (FET) device. The size of FET-based biosensors is significantly larger than the size of most single cell sensors. However, FET-based biosensors have an advantage through the ease with which they can be integrated into sensor arrays to detect multiple analytes [10].

2.2.2.5 Dielectrophoresis

Dielectrophoresis (DEP) – the action of polarizable particles in non-uniform electric fields – can be used to produce stable traps for bioparticles [11] as well as provide cell separation based upon size or electrical properties [12]. The basic principle of DEP is the phenomenon whereby neutral particles, in response to a spatially nonuniform electric field, experience a net force directed toward locations with increasing or decreasing field intensity according to the physical properties, such as dielectric properties and size, of the particle and medium. The essential feature that distinguishes dielectrophoretic effects from electrophoretic ones is that AC, rather than DC, electrical fields are involved.

DEP has been successfully applied on microchip scales to manipulate and separate a variety of biological cells including bacteria, yeast, and mammalian cells. A detailed application of DEP for single cell trapping will be presented in Section 2.4 together with other trapping techniques.

2.2.2.6 Dielectrophoretic impedance measurement

This method combines the techniques of dielectrophoretic cell manipulation discussed in Section 2.2.2.5 and impedance spectroscopy [13]. Impedance spectroscopy of single cells provides information on the properties of the cell membrane, including the binding of ligands to receptors as well as the dielectric properties of the cytoplasm. DE of cells provides a means of manipulating cells, including electro-rotation of cells and is utilized to guide, trap and sort single mammalian cells. The dielectrophoretic behavior of the cells is a function of their dielectric properties. Likewise, the impedance of cells in suspension depends on both their dielectric and conductance properties. The dispersion

with frequency of these properties provides a novel method for characterizing and isolating (sorting) cells. The typical frequency range used for this application is 100 kHz ~ 1 MHz.

2.2.2.7 Light-addressable potentiometric sensor

Surface charge changes can also be detected using light. For example, in a light-addressable potentiometric sensor (LAPS), the change in surface potential is detected by measuring a photo-induced current, and the surface charge depends on the pH of the fluid containing cells [14].

2.2.3 Optical methods for single cell identification

Optical biosensors have been widely used to provide plentiful information of the biological cells while overcoming the destruction of the cells induced by most of the non-optical methods. A brief discussion of the optical properties of biological cells is necessary before going into the details of optical sensing technologies. This section talks about the structures of cells that are of particular interest to biophotonics and the corresponding optical properties followed by a review of some useful optical technologies for single cell detection.

2.2.3.1 Optical properties of biological cells

The optical properties of a biological cell, which are closely related to the structure of the cell, form the basis of optical detection of single cells. This section briefly discusses the refractive indices of cellular structures and their corresponding usefulness in optical

detection of the cell. Biological cells contain a number of different types of organelles. These include the nucleus and mitochondria. The organelles are immersed in a fluid called the cytoplasm. The cytoplasm and organelles are contained by the cell wall. Thus the cell can be thought of as a bag of fluid containing sub-cellular structures. The organelles have a higher mass density and therefore a higher refractive index than the cytoplasm. From the optical point of view, the organelles act as scattering centers. If the cell is within the path of an optical beam, it will scatter light. The angular distribution of the scattered light depends on a large number of parameters. Among these are (1) size and refractive index of the cell, (2) size and refractive index of the organelles, and (3) refractive index of the surrounding medium. The nucleus is the largest of the organelles. It has therefore been the main subject of analysis by optical scattering experiments.

An important optical property that has been widely used for single cell differentiation is the refractive index change when a cell becomes cancerous. Tumors consist of cells with structural changes produced by transformation that show aberration in the normal behavior. Cancer is a special type of tumor that exhibits much more rapid multiplication (proliferation) of cells compared to normal cells. After gaining the fundamental knowledge of the optical properties of biological cells, let us look at some optical technologies for single cell detection.

2.2.3.2 Time-of-flight optophoresis

Optophoresis is a non-invasive cell analysis technique that is based on the interaction of live whole cells with optical gradient fields, typically generated by a near-infrared

laser. The magnitude of the interaction depends upon the intrinsic physical properties of the cells, such as their refractive index, composition, size, and morphology. The interaction is similar to the mechanisms for optical tweezers, which are discussed in Appendix A. Time-of-flight (TOF) optophoresis is an implementation of this technology in a microfluidic environment. It measures cell travel times through a fixed distance with and without irradiation from the laser, and therefore the change in transit time introduced by the presence of the infrared laser provides a signature for the cell. By calculating such measurements for a population of cells (typically 200-300 cells per population), different cell types, drug treatments, or biological states can be compared quantitatively without the need for external labels or markers. H. Zhang and colleagues constructed an integrated TOF system, which is sensitive enough to distinguish between closely related cell populations, such as cancerous vs. non-cancerous and drug treated vs. untreated [15].

2.2.3.3 Cavity ring-down spectroscopy

Cavity ring-down (CRD) spectroscopy, a new direct absorption spectroscopic technique that can be performed with a pulsed light source, was first introduced by O'Keefe and Deacon in 1988 [16]. CRD technique is based upon the measurement of the rate of absorption rather than the magnitude of absorption of a light pulse confined in a closed optical cavity with a high Q-factor. CRD is typically implemented in an optical resonator formed by two highly reflective mirrors and derives its high characteristic sensitivity from the measurement of the resonator's decay rate. This rate, which is directly proportional to its internal optical losses, including those due to molecular

absorption and scattering, is insensitive to common sources of noise, such as laser intensity fluctuations and interference from external absorbers, allowing quantitative detection of trace concentrations. CRD spectroscopy offers a real-time response in a simple, compact, less expensive arrangement that requires negligible sample preparation.

P. B. Tarsa and colleagues have successfully implemented cavity ring-down spectroscopy in an optical fiber resonator for label-free detection of mammalian cancer cells [17]. Figure 2.3 (a) shows a schematic diagram of the fiber optic cavity ring-down apparatus. The cancer cells stick to the discrete tapered fiber sensing regions by chemically treating the fiber surface with poly-D-lysine, which is commonly used as a culture plate coating for anchoring cells. An image of absorbed cells on the surface of the fiber taper is shown in Figure 2.3 (b). The application of cells to the coated taper significantly affects the optical loss of the ring-down system due to the optical scattering of the evanescent field surrounding the fiber. The taper was dried with compressed air prior to data acquisition, allowing the number of adhered cells being determined by microscopic visual inspection of the coated taper using a microscope. Single-cell sensitivity has been achieved by quantitatively comparing the number of the adhered cells with the optical ring-down time at the same time.

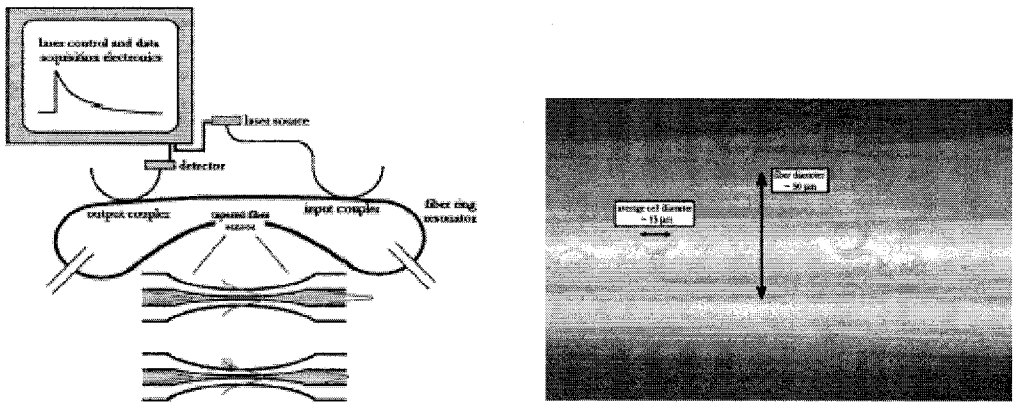

(a) (b)

Figure 2.3 (a) Schematic diagram of the fiber optic cavity ring-down apparatus, not drawn to scale. (b) Image of adsorbed cells on the surface of the fiber taper. (Reproduced from reference [17])

2.2.3.4 Confocal micro-Raman spectroscopy

Confocal micro-Raman spectroscopy is a promising tool for detection and identification of molecules contained in a tiny space based on measuring the molecular vibration frequencies from the scattered light. The position, intensities, and line widths of the Raman peaks in the spectra can yield useful information about the composition, secondary structure, and interactions of DNA-protein complexes inside the living cells. The major obstacle of using this technique for single cell studies is that the living cells being studied may move away from the confocal excitation volume within the acquisition time due to Brownian motion since a relatively long acquisition time is often required to obtain a Raman spectrum. Therefore the immobilization of the living cells without changing the chemical microenvironment of the cells plays an important role in this technique.

The use of optical trapping may relax those obstacles for single cell studies and permit high sensitivity. C. G. Xie and Y. Q. Li have studied single biological cells, including *E. coli* bacteria, yeast cells, and red blood cells, with a confocal micro-Raman spectroscopy system that uses the optical trapping technique [18]. They used a tunable laser to capture a living cell in solution, confine it in the confocal excitation volume, and then excite the Raman scattering. Figure 2.4 shows the schematic diagram of the experimental setup they designed. With this system, they obtained high-quality Raman spectra from single optically trapped biological cells. A significant difference between control and heat-treated *E. Coli* B cells was also observed due to the denaturization of biomolecules.

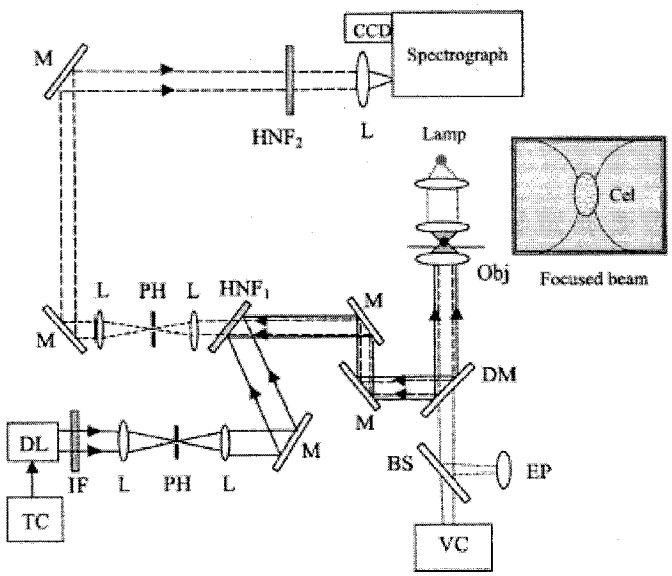

Figure 2.4 Experimental setup. A diode laser (DL) beam passes through an interference filter (IF), a pinhole (PH), and is then introduced into an inverted microscope through a dichroic mirror (DM) to form an optical trap. The Raman-scattering light of the trapped particles is collected with the same objective, passes through a holographic notch filter (HNF1) and a pinhole (PH), and is then focused onto the entrance of an imaging spectrograph equipped with a CCD detector. M-reflection mirror; L-lens; BS-beam splitter; Obj-objective lens; EP-eyepiece; VC-video

camera; TC-Temperature controller; and Lamp-Green-filtered xenon illumination light. (Reproduced from Reference [18])

2.2.3.5 Optical coherence tomographic imaging

Optical coherence tomography (OCT) is a leading imaging modality to realize non-invasive observation of cells in their natural environment. OCT is an interferometric imaging approach that provides very high sensitivity and axial resolution, making it particularly attractive for non-invasive imaging of the living retina. For example, Y. Zhang and colleagues have recently successfully utilized OCT method for the non-invasive observation of the living human retina at single cell level [19].

2.2.3.6 Fluorescence correlation spectroscopy

Fluorescence correlation spectroscopy (FCS) analyzes fluctuations in fluorescence within a small observation volume. Autocorrelation analysis of FCS fluctuation data can be used to measure concentrations, diffusion properties, and kinetic constants for individual fluorescent molecules. Photon count histogram analysis of fluorescence fluctuation data can be used to study the oligomerization of individual fluorescent molecules. If the FCS observation volume is positioned inside a living cell, these parameters can be measured *in vivo*. FCS can also provide the requisite quantitative data for analysis of molecular interaction networks underlying complex cell biological processes. More detailed information on the fundamentals of FCS can be found in the paper written by M. K. Levin [20].

Although fluorescence spectroscopy (FS) is very useful, it is necessary to inject fluorescent labeling molecules into the cells and some of the labeling materials

themselves may possibly affect the analyte distribution and biochemical pathways in cells. In such cases, it is hard to clarify whether the probing molecule has any influence on the cell. Therefore, novel techniques for in situ analysis of intact single cells are welcomed.

2.2.3.7 Auto-fluorescence spectroscopy

Auto-fluorescence (AF) spectroscopy is a novel method for studying unlabeled living mammalian cells based on their AF signal. The combination of cellular AF detection and microfluidic devices has the potential to facilitate high-throughput analysis of different cell populations. J. Emmerlkamp et al. have recently demonstrated that granulocytes were successfully differentiated from human red blood cells (RBCs) based on differences in AF [21]. Figure 2.5 shows the schematic side view of the AF detection setup they used.

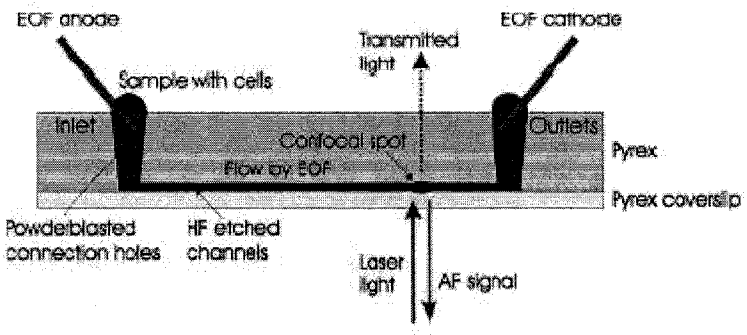

Figure 2.5 Schematic side view of the detection setup. The confocal detection spot is located just before the channel divides into the two outlets. (Reproduced from Reference [21])

The great advantage of AF spectroscopy is that no labeling with fluorescent reporter probes is required, which will result in reduced sample preparation times. In addition,

unlabeled cells avoid potential cell toxicity, proliferation and viability issues that are sometimes associated with fluorescent dyes.

2.2.3.8 Thermal lens microscopy

Thermal lens microscopy (TLM) is an effective way to overcome the drawback of the fluorescent technique since the TLM can detect absorption substances without the use of labeling materials.

E. Tamaki *et al.* developed a TLM detection system for measuring the distribution of chemical substances in a single cell [22]. TLM is based on the thermal lens effect, which is a photothermal effect and results when energy from a laser beam passing through a sample is absorbed, causing heating of the sample along the beam path [23]. Figure 2.6 shows a schematic diagram of the thermal lens formation in a sample. The lens is created through the temperature dependence of the sample refractive index. The lens usually has a negative focal length since most materials expand upon heating and the refractive index is proportional to the density. This negative lens causes beam divergence and the signal can be detected as a time dependent decrease in power at the center of the beam.

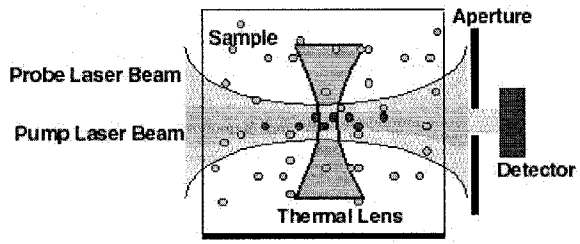

Figure 2.6 Thermal lens formation in a sample. (Reproduced from reference [23])

E. Tamaki *et al.* developed a TLM detection system for measuring the distribution of chemical substances in a single cell [22]. In their experiments, the biological cells were injected into a cell culture chip fabricated in quartz glass plates and mounted on a computer controlled 3D scanning stage with a spatial resolution of ~1 μm. A frequency-doubled YAG laser (532 nm) and a He-Ne laser (632 nm) were used as the excitation and the probe laser respectively. They successfully acquired the 2D imaging of the cytochrome *c* distribution in a living single cell by measuring the 2D intensity using a photodiode (NF Electronic Instruments, model 3627).

2.2.3.9 CMOS based optical sensors

The possibility of investigating individual cell interactions on a large scale would open up great possibilities for tasks such as drug screening, cell separation and analysis. N. Manaresi *et al.* developed a new approach to the integration on silicon of dielectrophoretic actuators and optical sensors for single cell detection [24]. The sensor was fabricated in an 8 x 8 mm^2 chip implemented in a two-poly three-metal 0.35-μm CMOS technology, featuring 102,400 actuation electrodes, arranged in an array of 320 x 320, 20 μm x 20 μm microsites each comprising addressing logic, an embedded memory for electrode programming, and an optical sensor. The chip enables software-controlled displacement of more than 10,000 individual cells in a parallel fashion. This is the first device that allows programmable manipulation of individual cells with no need for fluid flow nor micromachining, combined with embedded optical detection.

2.2.3.10 Two-beam optical trapping

A two-beam optical trap catches and holds an object in a fluidic channel using a counter-propagating optical trap. It predicts the refractive index and size of the object through the forward scattered light without referring to biological markers that may interfere with the biological function being studied. Figure 2.7 illustrates the experimental setup of a two-beam optical trapping system designed by researchers at University of California [25].

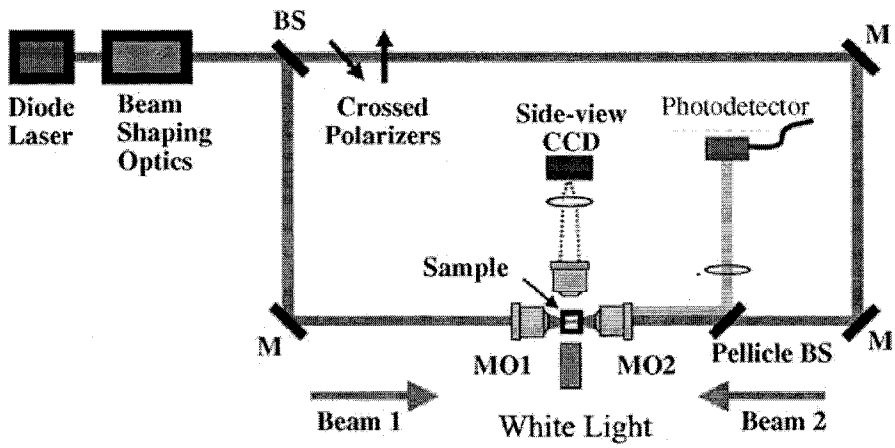

Figure 2.7 Schematic of counter-propagating optical trap measurement system. Inset at bottom gives details of the beam shaping optics. BS, beam splitter; M, mirror; MO, microscope objective; AP, anamorphic prism; CL, cylindrical lens. (Reproduced from reference [25])

2.2.3.11 Intracavity spectroscopy

Intracavity spectroscopy is based on the refractive index perturbation of an optical resonator as shown in Figure 2.8. The detection of the biological cells can be achieved by observing the transmission spectra of the optical cavity. P. L. Gourley *et al.* have utilized an optically pumped VCSEL based intracavity spectroscopic sensor for the

detection of single blood cells [26-32]. The theoretical basis of this project is intracavity spectroscopy. This technique is closely related to the research presented in this dissertation, and it will discussed in detail in Chapter 3.

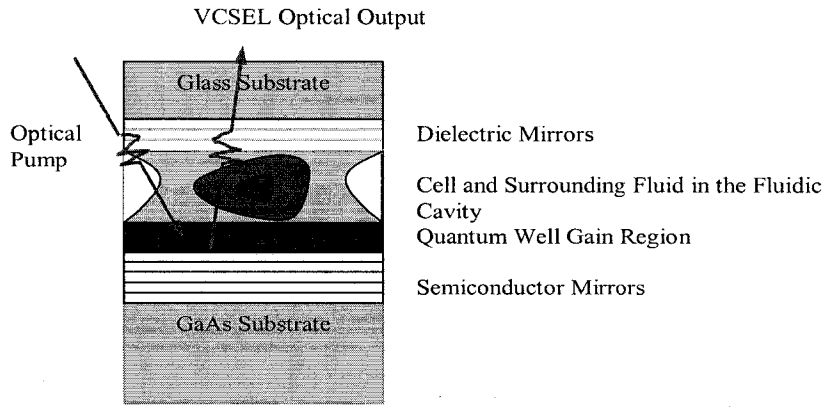

Figure 2.8 Schematic diagram of the optically pumped VCSEL based biosensor developed at Sandia National lab. (Reproduced from reference [26])

2.3 Flow cytometry

Flow cytometry is a powerful technique for analyzing chemicals, particles, and cells in clinical diagnostics, biochemistry, and biology. In flow cytometry, cells or particles flow in suspension, preferably in a single file, past a sensing point one by one. The sensing is conducted by using an optical technique where a highly focused beam from a light source interacting with an individual cell, a bioassembly, or a microbead produces scattering or fluorescence. The optical response is used to determine cellular features and organelles, providing counts and the ability to distinguish different types of cells in a heterogeneous population.

2.3.1 Basics of flow cytometry

The basic steps of flow cytometry are (i) fluorescence labeling of biological substances in cells, (ii) hydrodynamic focusing to produce a laminar flow of cells in a single file at the interrogation point in a fluid stream, (iii) laser illumination and collection of the optical response, and (iv) data acquisition and processing. Figure 2.9 shows a schematic of a five-parameter flow cytometer.

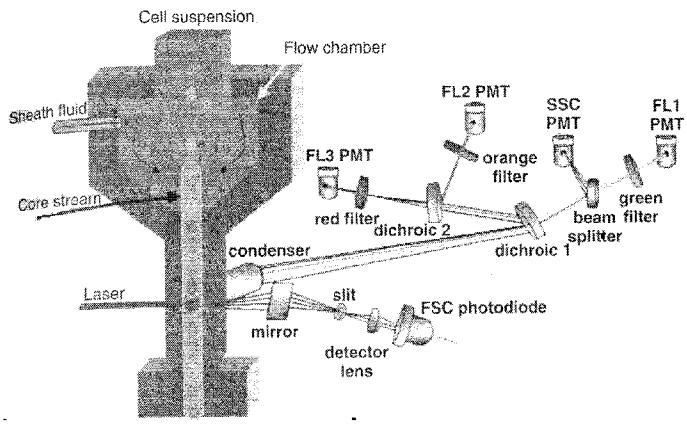

Figure 2.9 Schematic of a five-parameter flow cytometer showing details. (Reproduced from reference [1])

Flow cytometry yields measurement of various optical responses that provide a set of properties, also called parameters, such as scattered light and fluorescence that provide unique characteristics of a specific type of cells. Figure 2.10 illustrates the various optical response generated by interaction of laser light with the flowing cells.

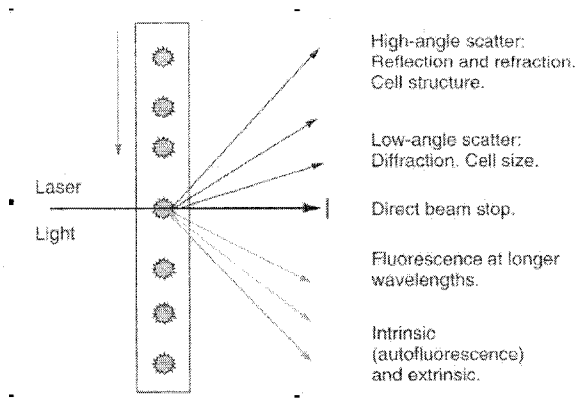

Figure 2.10 The various optical response generated by interaction of laser light with the flowing cell. (Reproduced from reference [1])

The three major optical responses generated by interaction of laser light with the flow cell are summarized here. (1) Forward scattering (FS), also called small angle scattering, provides information on the size and viability of cells or particles. FS is measured in a very narrow scattering angle range ($0.5\text{-}5.0^0$ to the incident light). (2) Large angle scattering (LS) gives information of surface roughness and internal structures of cells or particles, such as cell internal granularity. LS can be detected in a broad scattering angle range ($15\text{-}150^0$ to the incident light). (3) When a cell or particle passes through the light beam, the amount of direct light decreases due to a combination of absorbance and light scattering. This decrease is called extinction (EX). EX provides information on size, viability, and hemoglobin and protein contents.

2.3.2 Development of flow cytometry

The current market for flow cytometry is near one billion dollars worldwide, showing the wide usage of this instrument. When flow cytometer is combined with cell sorting, the so-called fluorescent activated cell sorters (μFACS) are realized. In the past two

decades, the micro fabrication technologies developed for the microelectronics industry have been utilized for miniaturizing flow cytometers and μFACS. However, the vast majority of those microsystems used bulk optics for the optical measurements. Recent advances in solid-state lasers, microfluidics, microarray technology, micro-optics, and miniaturized detectors provide challenging technological opportunities for developing small and compact flow cytometers with enhanced capabilities to simultaneously monitor many parameters than currently possible. Wang *et al.* have recently integrated several optical elements (waveguides, lens and fiber-to-waveguide couplers) with the microfluidic channels in SU-8 to form a complete microchip flow cytometer. They demonstrated that forward scattering, large angle scattering, and extinction from single polystyrene beads could be measured at the same time [33] and [34].

2.4 Micrometer-sized particle manipulation

The ability to manipulate biological cells and micrometer-sized particles plays an important role in many biological applications. One might envision several methods to immobilize cells in a microfludic channel, such as is needed for the OFIS sensors. Among the forces most suitable for positioning micron-sized particles are acoustic, optical, physical, and electrical forces. This section presents several popular particle manipulation techniques such as ultrasonic trapping, optical trapping, mechanical trapping, dielectrophoretic trapping, and optoelectronic trapping.

2.4.1 Ultrasonic trapping

Ultrasonic fields use acoustical energy to either trap particles at field nulls or to actually levitate small volumes of liquids in air with one or a few cells inside. Ultrasonic particle manipulation, however, suffers from problems of array ability and sufficient localization to trap single particles and is thus unsuitable for our application.

2.4.2 Optical trapping

Optical tweezers use optical gradient forces to trap particles at the focal point of strongly focused laser beams. Optical tweezers can be used to manipulate single particles in three-dimensions and allow concurrent imaging. Optical tweezers offer high resolution for single cells trapping, but have limited manipulation area owing to tight focusing requirement. Recent work tried to overcome this limitation by either utilizing individually addressable VCSELs [25] or light intensity patterns to manipulate cells [35]. But their applications in microfluidics for cell-based assay are still limited due to the complicated optical setup, complex operation, and expensive instrumentation. Detailed information about the physics principle of optical tweezers is presented in Appendix A together with demonstration of the experimental setup designed in our lab.

2.4.3 Physical trapping

Another particle-manipulation technology is simply to use physical forces to contain particles. This can take the form of arrays of micro-fabricated wells into which particles can be deposited and shielded from destabilizing fluid flows, thus effecting trapping. These methods may affect the optical confinement in the transverse direction, however,

as their structures directly touching the cells. In addition, all physical trapping techniques may cause contact-induced cellular responses that may interfere with assay result. Therefore, physical trapping has limited applications in microfluidics for cell-based assays.

2.4.4 Dielectrophoretic trapping

Dielectrophoretic (DEP) trapping is the electronic analog of optical tweezers. DEP forces, arising from a cell's polarizability, can be used to create microsystems that separate cell mixtures into its component or act as electrical "handles" to transport cells or place them in specific locations [36].

DEP-based particle traps have many advantages over the aforementioned forces for manipulating micron-sized particles. First, they are amenable to micro-fabrication. Second, they can trap particles of various sizes depending on the trap geometry. In addition, since they are active traps, they can be turned off, releasing particles and effecting sorting. Finally, the electrodes can be designed in such a way that doesn't affect the optical confinement of cells. By exploiting the dielectric difference between different particles and cells, DEP techniques have been able to discriminate and sort biological cells that have differences in membrane properties (permeability, capacitance and conductivity), internal conductivity, and size [37]. Because of these advantages and the compatibility with the fabrication of the optofluidic cavities, I have chosen to use DEP based particle traps in this dissertation. Detailed information on trap design will be presented in Section 4.4.8.

2.4.5 Optoelectronic tweezers

Recently, an optoelectronic tweezer (OET) that is capable of trapping and transporting multiple biological cells has been developed by researcher at University of California, Berkeley [35]. OET is based on a new mechanism called light induced dielectrophoresis. OET allows a focused optical beam to create a virtual electrode on a photoconductive surface, producing a highly non-uniform electric field. This enables optical addressing of dielectrophoresis forces with a spatial resolution of 1 μm. The optical intensity required is three orders of magnitudes lower than that of conventional optical tweezers. Figure 2.11 illustrates the OET device structure. The liquid containing the cells or particles of interest is sandwiched between a upper transparent, conductive ITO-coated glass, and a lower photoconductive surface, which consists of multiple featureless layers of ITO-coated glass, an n+ hydrogenerated amorphous silicon (a-Si:H) layer, an undoped a-Si:H layer, and a silicon nitride layer. These two surfaces are biased with an a.c. signal, 10V peak-to-peak. When projected light illuminates the photoconductive layer, it turns on the virtual electrodes, creating non-uniform electric fields and enabling particle manipulation via DEP forces. Under direct imaging, sophisticated virtual electrodes can be easily patterned and reconfigured to create dynamic electric field distributions for continuous particle manipulation without the assistance of fluidic flow.

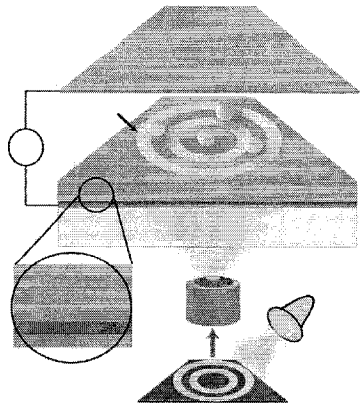

Figure 2.11 Device structure used in optoelectronic tweezers. (Reproduced from reference [35])

2.5 Microfluidic flow control

Microfluidic flow control plays an important role in biosensor designs since cells or microparticles need to flow through the detection region in a controllable way. This is usually done with the integration of cell traps discussed above so that cells can be trapped and released freely. This section briefly reviews some of the popular microfluidic flow control techniques. Pressure driven flow is the easiest way for delivering fluid into microfluidic devices. Syringe pumps are usually used when flow speed control is required. For cell analysis, sheath fluid is widely used to help the cell flow in a single file format, for example, in flow cytometers.

2.6 Microfluidic device sealing

Bonding technology is one of the most important technologies in making a micro-chip, which should not reduce the chemical inertness, uniformity, or integrity of the etched channels. This section reviews the general background of microfluidic device sealing techniques.

2.6.1 Polymeric material based device sealing

Polymer-based micro-devices have gained increased interest due to the low fabrication costs, the well-known micromachining techniques and the wide variety of available materials, such as PDMS, PMMA, or SU-8. This section will briefly review some device sealing techniques for the popular polymer based microfluidic devices such as polydimethylsiloxane (PDMS), SU-8, PMMA, and polyimide.

2.6.1.1 Soft lithography

Polymer based microfluidic devices are usually fabricated using soft lithography. The basic procedures of soft lithography are: 1) microfluidic channels are replicated by casting pre-polymer against a master mold, which is typically created by a variation of contact lithography that uses inexpensive and rapidly prepared high-resolution transparency masks in place of chrome masks. 2) The master mold has positive relief structures that hollow out negative relief structures in the cured (hardened) polymer cast against it. 3) The polymer structures with open channel features are then sealed against flat surfaces. Soft lithography has some unique advantages over other forms of lithography, such as photolithography and electron beam lithography. They include the following:

- Lower cost than traditional photolithography
- Well-suited for applications in biotechnology and plastic electronics
- well-suited for applications involving large or nonplanar (nonflat) surfaces
- Does not need a photo-reactive surface to create a nanostructure

2.6.1.2 PDMS based device sealing

PDMS, the most popular elastomer, enjoys several advantages as a material for fabricating microfluidic systems [38]. The material is soft compared to silicon or glass, but is moderately still polymer (Yong's modulus ~1MPa). The elastomer stiffness can be adjusted by the degree of cross linkage, which is controlled by the amount of curing agent added to the base chain monomers (typically in a 1:10 weight ratio). PDMS is optically clear making integration of on-chip or external optical devices convenient. Finally, this material, which is intrinsically hydrophobic, can be chemically treated to become hydrophilic. PDMS based microfluidic devices can be easily fabricated by pouring the elastomer into the molds made from SU-8. After curing the elastomer, the channel patterns will be transferred from the molds to the PDMS layer. PDMS can be directly peeled off from the molds. Treating the cured PDMS in the oxygen plasma usually does the sealing between PDMS and glass. PDMS based technique was not used in this dissertation due to the difficulty in controlling the parallelism between the superstrate and the substrate and dielectric film deposition on PDMS.

2.6.1.3 SU-8 based device sealing

SU-8 is a kind of negative photoresist that can be photo patterned as the conventional photoresist and is often used as the molding for PDMS based microfluidic devices or to fabricate optical waveguide type of microfluidic devices. Sealing between two SU-8 layers could be achieved by properly controlling the crosslinking rate of the polymer. Papers [39-44] talking about SU-8 to SU-8 wafer bonding are listed in the reference at the end of the chapter.

2.6.1.4 Polyimide base device sealing

Polyimide is another type of polymer that has excellent chemical and thermal stability, low water uptake, and good biocompatibility [45-46]. This paragraph summarizes several techniques that have been developed to fabricate polyimide based microfluidic devices: 1) Polyimide solvent bonding technique, where microfluidic devices are fabricated between two wafers. Open channels are patterned on a first wafer, a second wafer is spin coated with polyimide precursor and the two wafers are put in contact and bonded together in a vacuum oven. This method can suffer from inhibited solvent evaporation during final cure. As the fabricated channels are located between two wafers, high internal pressures can develop which might create debonding forces. 2) Layer transfer technique, where a fully cured Kapton™ foil is bonded to the open channel structures by using a thin layer of polyimide precursor as adhesive. With this method the top layer is not easily structured and only Kapton™ foils with a certain thickness can be used. 3) Layer transfer and lamination technique is used to fabricate flexible microfluidic channels in various shapes and with a wide range of dimensions.

2.6.2 Glass based device bonding

A wide range of bonding processes have been used to seal glass based microfluidic devices. This section briefly reviews some of the popular techniques used for bonding glass substrates. Good references for various wafer bonding techniques can be found on LTD's and SUSS's websites [Applied Microengineering Ltd's website].

2.6.2.1 Wafer direct bonding

The most straightforward glass-to-glass sealing technique is wafer direct bonding, also called fusion bonding, by means of joining of two atomically smooth and clean surfaces at room temperature and pulling the two bodies together into intimate contact by attractive forces so that bonds can form across the interface. After joining the two wafer surfaces, the bonded pairs are annealed at a high temperature to ensure the formation of strong bonding. With proper procedure the bonded interface can achieve bulk strength. However, wafer direct bonding requires a high-temperature annealing step after the room temperature joining, to ensure the formation of strong and uniform bonding, i.e., to enable interface surface diffusion and covalent or ionic crystal bonds. For example, fusion bonding was used to fabricate micro-chips consisted of quartz and Pyrex to measure chemical reactions in a small volume at more than 1000^0C and it took about one or two days to bond the two quartz wafers together. This high-temperature annealing is incompatible with many otherwise potential applications and it may cause material degradation, especially when bonding thermally mismatched materials. Therefore, glass wafer direct bonding is seldom used in modern MEMS applications.

2.6.2.2 Thermocompressive bonding

Thermocompressive bonding is simply the joining of two surfaces via the welding of a layer of soft metals on each surface. The most common metal for MEMS applications is gold, with a suitable adhesion layer. Moderate temperature (~300°C) and pressure (10^6MPa) are needed. This technique offers very low outgassing and therefore is attractive for sealing of evacuated cavities. Due these advantages, thermocompressive

bonding was used to seal the optofluidic cavities in this thesis. Details on thermocompressive bonding of patterned glass substrates will be presented in Section 4.2.3. The stringent requirements for this bonding technique are tight requirements for wafer topography, the method is sensitive to particles, and alignment and bonding have to be on separate equipment.

2.6.2.3 Solder bonding

Solder bonding process works by reflowing low melting point metals to form a seal. Typical metals are Au-Sn, Cu-Sn and Pb-Sn. The metals can be applied by various thin film deposition techniques. The reflow process means that the method is not well suited where accurate alignment is needed and, as is the case with thermocompressive bonding, the metallic nature of the bond makes it incompatible with the inclusion of metal tracks for interfacing with sealed devices. This technique differs from thermocompressive bonding in that the metallic intermediate layer needs to be melted for solder bonding. The solder technique is tolerant to particles and is most widely used for electrical contacts (e.g. flip chip bonding).

2.6.2.4 Anodic bonding

Anodic bonding technique is an established technology in packaging and encapsulation of micromechanical sensors and actuators [xx]. Anodic bonding is restrained to bonding of sodium containing glass with similar thermal expansion as the semiconductor substrate. Anodic bonding system is expensive and needs high voltage (500–1000 V) and temperature (around 400^0C). Nearly all the applied field appears

over a short depleted transition region in the glass close to the interface. Under the applied field mobile sodium ions in the glass migrate toward the cathode and oxygen ions migrate to the Si anode, with they react with the Si wafer forming a strong bond between the wafers. Anodic bonding is less sensitive to surface roughness as compared to wafer direct bonding, and has very high strength. However, anodic bonding requires high voltage and high bonding temperature that are incompatible with CMOS. It can induce stress due to material difference (glass vs. silicon). Also the alignment and bonding has to be operated on separate equipment.

2.6.2.5 Chemical assisted bonding

Chemical assisted bonding is one other solution for glass wafer bonding at a low temperature. For example, diluted hydrogen acid could bond two quartz wafers at room temperature [47]. Various adhesives (epoxies, silicones, photoresists, polyimides, UV sensitive glues etc.) can also be used for wafer bonds. In-situ alignment can be used with this technique but like other processes that rely on some flow in the intermediate layer, alignment accuracy is compromised. The adhesive can be applied by spinning, spraying etc., and the process normally requires some heat (typically between room temperature and 400^0C depending on the adhesive being used) and pressure. The technique is tolerant to particles and is useful when the wafers have a severe temperature limitation. Adhesive bonding is flexible with regards to wafer materials and can achieve high alignment accuracy if in-situ curing (e.g. UV) is used. However, this bonding technique is not typically hermetic (depends on material used) unless covered with

metallic films. Alignment can be difficult for adhesive bonding if cured in separate bonding system and some adhesives will generate out-gassing.

2.6.2.6 Sacrificial layer assisted bonding

The sacrificial layer method uses a dissolvable material to form the channel geometry. This sacrificial structure is embedded in other materials to form the micro-channels and is subsequently removed by solvent dissolution, anodically assisted wet etching, which is faster than conventional wet etching, or heating. Silicon oxide, metals and photoresist have been proposed as sacrificial materials and the technique has been used to manufacture channels in silicon, silicon oxide, metals and several polymers. However, the fabrication method can be quite time consuming, especially for small channel sizes, as the dissolution process is usually diffusion limited. This leads to a prolonged exposure of the substrate to the etchant that can result in device destruction due to the harsh chemicals.

2.7 Summary

This chapter has provided background information on certain topics that are relevant to the subject matter discussed in this report. Hopefully, it has helped the reader to develop an intuition about the subject discussed in the report, by providing a tutorial on the topic of biosensors and a literature review of single biological cell detection and associated fabrication.

References

[1] P. N. Prasad, "Introduction to biophotonics", *John Wiley and Sons*, 2003.

[2] B. Ilic, D. Czaplewski, M. Zalalutdinov, and H. G. Craighead, "Single cell detection with micromechanical oscillators", *J. Vac. Sci. Technol. B*, vol. 19, no. 6, pp. 2825-2827, 2001.

[3] A. Neef, R. Schafer, C. Beimfohr, and P. Kampfer, "Fluorescence based rRNA sensor systems for detection of whole cells of Saccharomonospora spp. and Thermoactinomyces spp.", *Biosens. Bioelectron*, vol. 18, pp.565, 2003.

[4] R. A. Yotter and D. M. Wilson, "Sensor technologies for monitoring metabolic activity in single cells-Part II: Nonoptical methods and applications", *IEEE Sensors J.*, vol.4, no.4, pp. 412-429, 2004.

[5] R. A. Yotter, L. Lee, and D. Wilson, "Sensor technologies for monitoring metabolic activity in single cells-part I: optical methods", *IEEE Sensors J.*, vol. 4, no. 4, pp. 395-411, 2004.

[6] B. F. Brehm-Stechen and E. A. Johnson, "Single-cell microbiology: tools, technologies, and applications", *Microbiology and Molecular Biology Reviews*, vol. 68, no. 3, pp. 538-559, 2004.

[7] D. P. Fergenson, M. E. Pitesky, and Herbert J. Tobias, et al "Reagentless detection and classification of individual bioaerosol particles in seconds", *Anal. Chem.*, vol. 76, pp.373-378, 2004.

[8] J. N. Stuart and J. V. Sweedler, "Single-cell analysis by capillary electrophoresis", *Anal. Bioanal. Chem.*, vol. 375, pp. 28-29, 2003.

[9] M. Lehmann and W. Baumann *et al.*, "Simultaneous measurement of cellular respiration and acidification with a single CMOS ISFET", *Biosensors & Bioelectronics*, vol. 16, no. 3, pp. 195-203, 2001.

[10] T. Muller, G. Gradl, S. Howitz, S. Shirley, T. Schnelle, and G. Fuhr, "A 3-D microelectrode system for handling and caging single cells and particles," *Biosens. Bioelec.*, vol. 14, no. 3, pp. 247, 1999.

[11] H. Morgan, M. P. Hughes, and N. G. Green, "Separation of submicron bioparticles by dielectrophoresis," *Biophys. J.*, vol. 77, no. 1, pp. 516, 1999.

[12] J. Suehiro, R. Hamada, D. Noutomi, M. Shutou, and M. Hara, "Selective detection of viable bacteria using dielectrophoretic impedance measurement method", *J. of Electrostatics*, vol. 57, no. 2, pp. 157-168, 2003.

[13] G. X. Xu, X. S. Ye, L. F. Qin, Y. Xu, Y. Li, and P. Wang, "Cell-based biosensors based on light-addressable potentiometric sensors for single cell monitoring", *Biosensors & Bioelectronics*, vol. 20, no. 9, pp. 1757-1763, 2005.

[14] H. C. Zhang, E. Tu, and P. J. Marchand *et al.,* "Time-of-flight optophoresis analysis of live whole cells in microfluidic channels", *Biomedical Microdevices*, vol.6, no.1, pp. 11-21, 2004.

[15] A. O'Keefe and D. A. G. Deacon, "Cavity ring-down optical spectrometer for absorption measurements using pulsed laser sources", Review of Scientific Instruments, vol. 59, no. 12, pp. 2544-2551, 1998.

[16] P. B. Tarsa, A. D. Wist, P. Rabinowitz, and K. K. Lehmann, "Single-cell detection by cavity ring-down spectroscopy", *Appl. Phys. Lett.*, vol. 85, no.19, pp. 4253-4255, 2004.

[17] C. G. Xie and Y. Q. Li, "Confocal micro-Raman spectroscopy of single biological cells using optical trapping and shifted excitation difference techniques", *J. of Appl. Phys.*, 93 (5), pp. 2982, 2003.

[18] Y. Zhang, J. Rha, R. S. Jonnal, and D. T. Miller, "Adaptive optics parallel spectral domain optical coherence tomography for imaging the living retina", Optics Express, vol. 13, no. 12, pp.4792-4811, 2005.

[19] M. K. Levin and J. H. Carson, "Fluorescence correlation spectroscopy and quantitative cell biology", *Differentiation*, vol.72, no.1, pp.1-10, 2004.

[20] J. Emmelkamp *et al.*, "The potential of autofluorescence for the detection of single living cells for label-free cell sorting in microfluidic systems", *Electrophoresis*, vol. 25, pp. 3740-3745, 2004.

[21] E. Tamaki *et al.*, "Single-cell analysis by a scanning thermal-lens microscope with a microchip: direct monitoring of cytochrome c distribution during apoptosis process", *Anal. Chem.*, vol. 74, pp. 1560-1564, 2002.

[22] www.photonics.cusat.edu/Research_Thermal lens.html

[23] N. Manaresi, A. Romani, G. Medoro, L. Altomare, A. Leonardi, M. Tartagni, and R. Guerrieri, "A CMOS chip for individual cell manipulation and detection", *IEEE J. of Solid-State Circuits*, vol. 38, no.12, pp.2297-2304, 2004.

[24] R. A. Flynn, B. Shao, M. Chachisvilis, M. Ozkan, S. C. Esener, "Counter-propagating optical trapping system for size and refractive index measurement of microparticles", Biosensors & Bioelectronics, vol. 21, no.7, pp. 1029-1036, 2006.

[25] P. L. Gourley, A. E. McDonald, and M. F. Gourley, "Vertical cavity surface-emitting laser scanning cytometer for high speed analysis of cells", *SPIE*, vol. 2679, pp. 131-141, 1996.

[26] P. L. Gourley, T. French, A. E. McDonald, E.A. Shields, and M. F. Gourley, "Ultrasensitive detection of red blood cell lysing in a microfabricated semiconductor laser cavity", *Proc. SPIE* 2978, pp.195-206, 1997.

[27] P. L. Gourley and M. F. Gourley, "Biocavity lasers for biomedicine", *Trends Biotech.*, vol. 18, pp. 443-448, 2000.

[28] P. L. Gourley, J. D. Cox, J. K. Hendricks, A. E McDonald, G. C. Copeland, D. Y. Sasaki, M. Curry and S. L. Skirboll, "Semiconductor microcavity laser spectroscopy of intracellular protein in human cancer cells", *SPIE*, vol. 4265, pp. 113-124, 2001.

[29] P. L. Gourley, "Biocavity laser for high-speed cell and tumour biology", *J. Phys. D: Appl. Phys.*, vol. 36, R228–R239, 2003.

[30] P. L. Gourley, J. K. Hendricks, A. E., McDonald, R. G. Copeland, K. E. Barrett, C. R. Gourley, and R.K. Naviaux, "Ultrafast nanolaser flow device for detecting cancer in single cells", *Biomedical Microdevices*, 7:4, 331–339, 2005.

[31] P. L. Gourley and R. K. Naviaux, "Optical phenotyping of human mitochondria in a biocavity laser", *IEEE J. of Selected Topics in Quantum Electronics*, vol. 11, no. 4, 2005.

[32] Z. Wang, J. El-Ali, M. Engelund, and A. Wolff, "Measurements of scattered light on a microchip flow cytometer with integrated polymer based optical elements", *Lab Chip*, vol. 4, pp. 372-377, 2004.

[33] C. H. Chen, F. Tsai, V. Lien, N. Justis, Y. H. Lo, "Scattering-based cytometric detection using integrated arrayed waveguides with microfluidics", *IEEE Photon. Tech. Lett.*, vol. 19, no.5-8, pp. 441-443, 2007.

[34] P. Y. Chiou, A. T. Ohta, and M. C. Wu, "Massively parallel manipulation of single cells and microparticles using optical images", Nature, vol. 436, no.7049, pp. 370-372, 2005.

[35] J. Voldman, "Electrical forces for microscale cell manipulation", *Annu. Rev. Biomed. Eng.*, vol. 8, pp. 425-454, 2006.

[36] P. Domachuck, I. C. M. Littler, M. Cronin-Golomb, and B. J. Eggleton, "Compact resonant integrated microfluidic refractometer", *Appl. Phys. Lett.*, no. 88, 093512, 2006.

[37] S. L. Peterson, A. McDonald, P. L. Gourley, D. Y. Sasaki, "Poly (dimethylsiloxane) thin films as biocompatible coatings for microfluidic devices: Cell culture and flow studies with glial cells", J. of Biomedical Materials, vol. 72, pp.10-18, 2004.

[38] C-T Pan, H. Yang, S-C Shen, M-C Chou, and H-P Chou, "A low-temperature wafter bonding technique using patternable materials", *J. Micromech. Microeng.*, vol. 12, pp. 611–615, 2002.

[39] F. J. Blanco, M. Agirregabiria, J. Garcia, J. Berganzo, M. Tijero, M. T. Arroyo, J. M. Ruano, I. Aramburu, and K. Mayora "Novel three-dimensional embedded SU-8 microchannels fabricated using a low temperature full wafer adhesive bonding", *J. Micromech. Microeng.*, vol. 14, pp.1047–1056, 2004.

[40] B. Bilenberg, T. Nielsen, B. Clausen, and A. Kristensen, "PMMA to SU-8 bonding for polymer based lab-on-a-chip systems with integrated optics", *J. Micromech. Microeng.*, vol. 14, pp. 814–818, 2004.

[41] B. Bohl, R. Steger, R. Zengerle, and P. Koltay, "Multi-layer SU-8 lift-off technology for microfluidic devices", *J. Micromech. Microeng.*, vol. 15, pp. 1125-1130, 2005.

[42] S. Tuomikoski, S. Franssila, "Free-standing SU-8 microfluidic chips by adhesivebonding and release etching", *Sensors and Actuators A*, vol.120, pp. 408–415, 2005.

[43] A. Mata, A. J. Fleischman, and S. Roy, "Fabrication of multi-layer SU-8 microstructures", *J. Micromech. Microeng.*, vol. 16, pp. 276–284, 2006.

[44] S. Metz, R. Holzer, and P. Renaud, "Polyimide-based microfluidic devices", *Lab on a Chip*, vol. 1, pp. 29–34, 2001.

[45] S. Metz, C. Trautmann, A. Bertsch, and P. Renaud, "Polyimide microfluidic devices with integrated nanoporous filtration areas manufactured by micromachining and ion track technology", *J. Micromech. Microeng.*, vol. 14, pp. 324–331, 2004.

[46] H. Nakanishi, T. Nishimoto, R. Nakamura, A. Yostumoto, S. Shoji, "Studies on SiO_2-SiO_2 bonding with hydrofluoric acid-room temperature and low stress bonding technique for MEMS", MEMS'98, pp. 609-614.

Chapter 3

Intracavity Spectroscopy for Single Cell Identification

In the previous chapter, the general background information on biosensor was presented. Intracavity spectroscopy is a novel biosensing technique that has been used to detect single biological cells for about a decade. This chapter will talk about the physics and the research work related to this important technique. Fabry-Pérot (FP) optical cavity is the test-bed for single cell intracavity spectroscopy. Therefore, the first part of this chapter will be directed toward the physical fundamentals of Fabry-Pérot interferometers with an emphasis on factors affecting the cavity finesse and the optical resolution. Section 3.2 briefly discusses the physics of intracavity spectroscopy and Section 3.3 gives a literature review of research in the area of intracavity spectroscopy including optically pumped and electrically injected vertical cavity surface emitting laser (VCSEL) based biosensors, a coupled cavity on-chip biosensor [1], and a passive on-chip fiber based FP cavity. Section 3.4 goes on to present the concept of the passive cavity interferometer based biosensors developed in this project. The goal of my research is to develop a passive optofluidic intracavity spectroscopic (OFIS) biosensor. The novelty and drawbacks of each cited research work in terms of usefulness to our application will be discussed.

3.1 General background of Fabry-Pérot interferometer

The Fabry-Pérot interferometer, initially designed in 1899 by C. Fabry and A. Pérot, is commonly used as a narrow-bandpass filter or as an instrument to measure spectral line

widths. It is also an instrument of extraordinary sensitivity, and its operation depends on the relative phase of the light beams that have undergone different numbers of reflections between the mirrors. Typical Fabry-Pérot design contains plane surfaces that are all partially reflecting so that multiple rays of light are responsible for creation of the observed interference patterns. In the next few paragraphs, the basic structure, operation and optical properties of Fabry-Pérot interferometers, and the applications to sensors will be discussed.

3.1.1 Physics: Fabry-Pérot interferometer

The Fabry-Pérot interferometer is a simple device, which relies on the interference of multiple reflected beams between two parallel mirrors. Figure 3.1 shows a schematic of a plane-plane Fabry-Perot cavity. The two partially transmissive mirrors (etalons) are at a distance *d* from each other and have a reflectivity R. The wave falls under the angle θ in the Fabry-Perot.

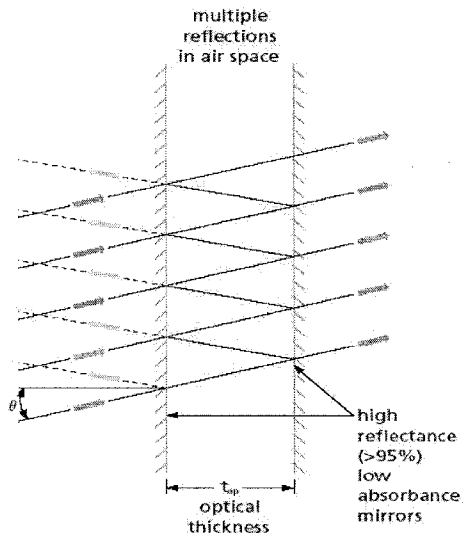

Figure 3.1 Schematic of a Fabry-Pérot interferometer copied from reference. (Reproduced from [2])

The basic physics governing the operation of a FP interferometer is the general theory behind interferometry. However, multiple reflections reinforce the areas where constructive and destructive effects occur making the resulting fringes much more clearly defined. Figure 3.2 shows a simplified model of a FP interferometer. Incident light undergoes multiple reflections between coated surfaces which define the cavity. Each transmitted wavefront has undergone an even number of reflections (0, 2, 4 ...). Whenever there is no phase difference between emerging wavefronts, interference between these wavefronts produces a transmission maximum.

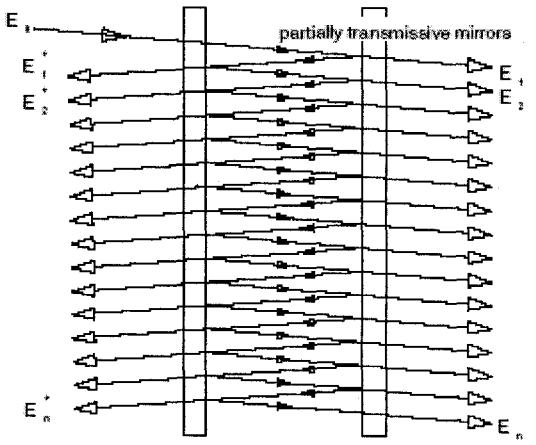

Figure 3.2 Ray tracing diagram of multibeam interferometry copied from reference. (Reproduced from reference [3])

The transmission of an ideal etalon, an Airy Function, is $T = \frac{(1-R)^2}{(1-R)^2 + 4R\sin^2(\frac{2\pi}{\lambda}\phi)}$, where

T is the transmission, R is the reflectivity of the mirrors, and Φ is the roundtrip phase change of the light ray.

If any phase change at the mirror surfaces is ignored then $\phi = \frac{2\pi}{\lambda} 2nd \cos\theta$, where

λ= the wavelength of the light

n = the index of refraction of the material between the mirrors

d = the distance between the mirrors

θ = the angle of the incoming light beam

3.1.2 Applications

There are three major areas of applications for Fabry-Pérot interferometers:

- As length measuring equipment for a known wavelength of the light source. The Michelson interferometer offers better possibilities for this.
- As a High-resolution spectrometer for measuring line intervals and line widths (optical spectrum analyzer).
- As a high quality optical resonator for the construction of lasers.

3.1.3 Finesse of Fabry-Pérot interferometer

Finesse of a Fabry-Pérot interferometer is an important parameter, which can be used to measure the ability of the interferometer to resolve fine spectral features. Cavity finesse is defined as the ratio of the frequency spacing between the adjacent transmission peaks or free spectral range (*FSR*) to the transmission peak full width at half-maximum (FWHM). The FSR is determined by the cavity length, L, and the refractive index of the media, n, between the mirrors and is expressed as $FSR = c/2nL$. The minimum resolvable bandwidth of the interferometer is given by the FWHM as shown in Figure

3.3. Thus, for a high-resolution spectrum, the FWHM should be small and the finesse should be high.

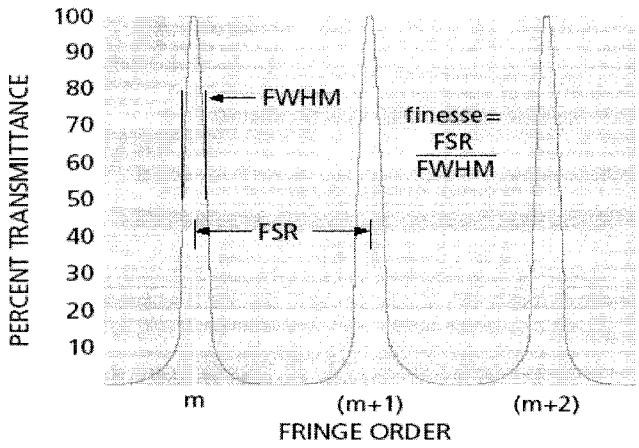

Figure 3.3 Transmission spectrum of a plane-plane Fabry-Pérot interferometer. (Reproduced from [3])

In reality, the Fabry-Pérot interferometers are usually constructed from solid materials such as glass or fused silica. Imperfections in the etalon such as imperfect flatness and parallelism will degrade the finesse. The value of the overall finesse is determined by the reflectance of the mirrors (the reflectance finesse, F_R) and the quality of the interferometer's construction (the defect finesse, F_d) according to $F_{total}^{-1}=F_R^{-1}+F_d^{-1}$.

3.1.3.1 Finesse vs. mirror reflectivity

The sharpness of individual peaks (the resolution of the spectral analyzer) is limited by the finesse of the Fabry-Pérot interferometer. For an ideal etalon, only the mirror reflectivity determines the cavity finesse $F_{total} = F_R = \pi\sqrt{R}/(1-R)$. Transmission peaks can be made very sharp by increasing the reflectivity of the mirror surfaces. Figure 3.4

shows the transmission curves of a Fabry-Pérot interferometer for different degrees of mirror reflection R. As finesse increases, the peaks of the transmission spectrum become narrower. Overall transmission, however, may drop as the result of increased absorption. The minimum resolvable bandwidth of the interferometer is given by the FWHM. Thus, for a high-resolution spectrum, the FSR should be small and the finesse should be high.

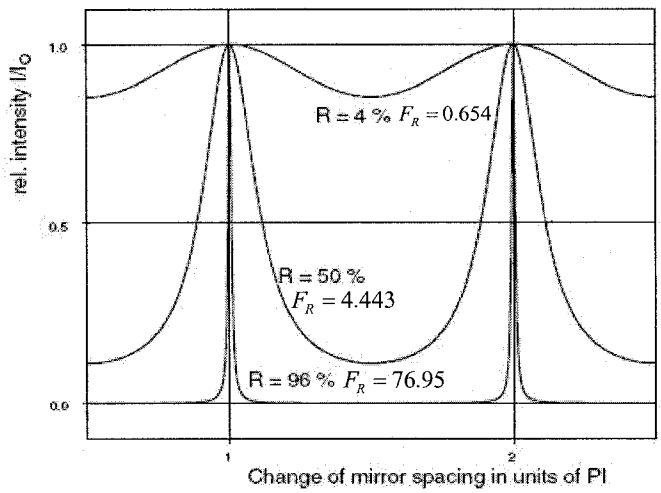

Figure 3.4 Transmission curves of a Fabry-Pérot interferometer for different degrees of mirror reflection R. (Reproduced from reference [3])

3.1.3.2 Finesse vs. roughness or scatter

Mirror surface roughness affects the optical reflectivity of the mirror coatings, which imposes an upper limit on finesse. The detrimental optical effects of various types of mirror defects have been extensively studied [4-6]. The allowed maximum finesse was calculated using the closed form formula in [5], $F_{total} = (F_{ideal}^{-2} + F_d^{-2})^{-1/2}$, where F_d is the

surface roughness limit on finesse defined as $F_d = \lambda/\left(2\sqrt{3}\sigma\right)$ with σ designating the RMS surface roughness and λ is the optical wavelength.

3.1.3.3 Finesse vs. non-parallelism

Mirror tilt is another factor that affects the finesse of the Fabry-Perot cavity. Mirror tilt induced cavity finesse can be calculated using a closed form formula derived by Sloggett, $F_{tilt} = \sqrt{3}/(\pi\sigma_{tilt}) = \sqrt{3}/\pi(\phi_{\max}/2)$, where $2\phi_{max}$ is the round-trip peak-to-peak phase variation across a circular aperture due to the nonparallelism of the flat interferometer plates. It can be calculated as $\phi_{\max} = (2\pi/\lambda)n(D/2)\tan(\Gamma_{tilt})$, where D is the effective aperture size, n is the refractive index of media inside the Fabry-Perot cavity, and Γ_{tilt} is the mirror tilt angle. Therefore, the measurement of Γ_{tilt} allows us to calculate the maximum cavity finesse limited by the non-parallelism. The allowed maximum finesse, F_{max}, of a tilted mirror FP cavity depends on F_{tilt} and the ideal finesse, F_{ideal}, according to $F_{total} = (F_{ideal}^{-2} + F_{tilt}^{-2})^{-1/2}$. A detailed calculation will be presented in the device characterization Section 4.3.4.

3.1.3.4 Finesse vs. beam collimation

Cavity finesse is also dependent on the collimation of the excitation beam. Figure 3.5 shows the transmission spectra of a FP microfluidic cavity excited by a broadband microscope light source and a well collimated LED. It is believed that a highly collimated laser beam can further improve the cavity finesse.

3.2 Physics: intracavity spectroscopy

The basic idea behind the intracavity spectroscopic biosensor is the refractive index perturbation effects due to the biological cells inside the fluidic cavity. Bioanalyte with relatively high refractive index introduced into the optical resonator will perturb the optical path length and the light confinement of the resonant modes, and consequently the spectrum of the resonator. In particular, a plane-plane FP cavity ideally only supports a single transverse mode with infinite plane wave behavior. However, the micro structure can modify the resonant beam propagation to allow multiple transverse modes at various frequencies. A simplified example is a single thin lens inside a plane-plane cavity with the resulting transverse mode spectra depending on the cavity length and lens focal length and position according to fundamental optical resonator theory very similar to that discussed by optics or lasers texts for curved mirror resonators [7]. The focal length in turn is a function of the refractive index of the lens and cavity medium and radii of curvature of the lens surfaces. Accordingly, the refractive index profile and size of cells alter the transverse mode spectra of a resonator, providing a sensitive probe of the cell's optical structure. Thus the specific modal structure is useful in classifying microstructures inside the cavity including differentiating cell types, sizes, and shapes [8, 9]. Figure 3.5 illustrates the spectral changes of a plane-plane Fabry-Pérot cavity induced by a biological cell.

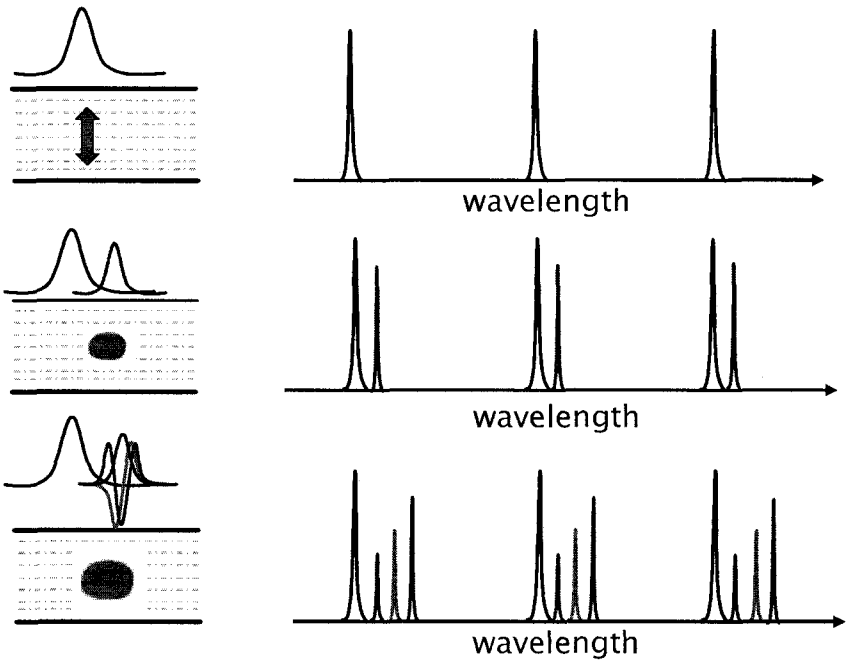

Figure 3.5 Schematic diagrams of spectral changes of a microfluidic FP cavity containing a biological cell with black peaks representing the bare fluidic cavity modes, blue, cyan, and green peaks representing the transverse modes.

Three spectral features related to the cell composition, size and shape can be concluded according to Figure 3.5. (i) The longitudinal modes shift from the bare fluid mode, as shown in Figure 3.5 (a), represents the refractive index difference between the cell and the bare fluid (principally blood plasma). This difference increases with hemoglobin, concentration of the cell. Hemoglobin is the major component of a normal hydrated cell with a concentration in the range of 32 to 36 g/dL, while the level decreases in the body of an anemic patient. (ii) The transverse modes spacing is related to the size of the cells with large mode spacing corresponding to a small cell diameter. As discussed in reference [10], a biological cell inside the microcavity has the same waveguiding effect as an optical fiber due to the slight difference in the dielectric constant between various cell components and the surrounding fluids. (iii) The envelope

of modal intensities is representative of the cell shape. As said in reference [11-14], cells within high biconcavity have spectra with significant intensity in the first and higher overtones, while spherical cells have spectra with a dominant fundamental modal intensity. Therefore introducing bioanalyte into a laser cavity will affect the lasing prosperities of the laser. These types of optical and electrical effects in turn provide sensitive probes for the detection and differentiation of the biological samples inside the cavity.

3.2 Prior work in intracavity spectroscopy

It is known that optical properties of biological cells can provide substantial information about cell parameters including size, shape, and refractive index variation. Optical processes such as light scattering, absorption, and diffraction can be used for the detection of single cells. For example, Katz et al. used light scattering effects to measure the size, shape, and refractive index variations of bacteria [8]. Laser based microfluidic devices, especially ones in which a microfluidic channel is an integral part of the laser cavity, are very attractive for biomedical diagnostics applications. This section talks about the prior work on an optically pumped and an electrically injected VCSEL based biosensors.

3.2.1 Optically pumped laser based biosensor

In 1997, P. L. Gourley *et al* integrated a half VCSEL chip to an external mirror with etched microfluidic channels and characterized the resulting mode spectra for different normal and abnormal blood cells introduced in the external fluidic cavity. Their biosensor

has a simple structure as illustrated in Figure 3.6. This biosensor is comprised of a half VCSEL chip containing only a bottom semiconductor mirror and a multiple-quantum-well (MQW) active region grown on a GaAs substrate, a fluidic cavity with a dimension about the size of the biological cell, usually a few microns, and a highly reflective dielectric mirror deposited on the top glass substrate. Transmission spectrum was externally excited by optically pumping the fluidic cavity through solid-state laser. Information of the bioanalyte inside the fluidic cavity was then extracted from the lasing spectra.

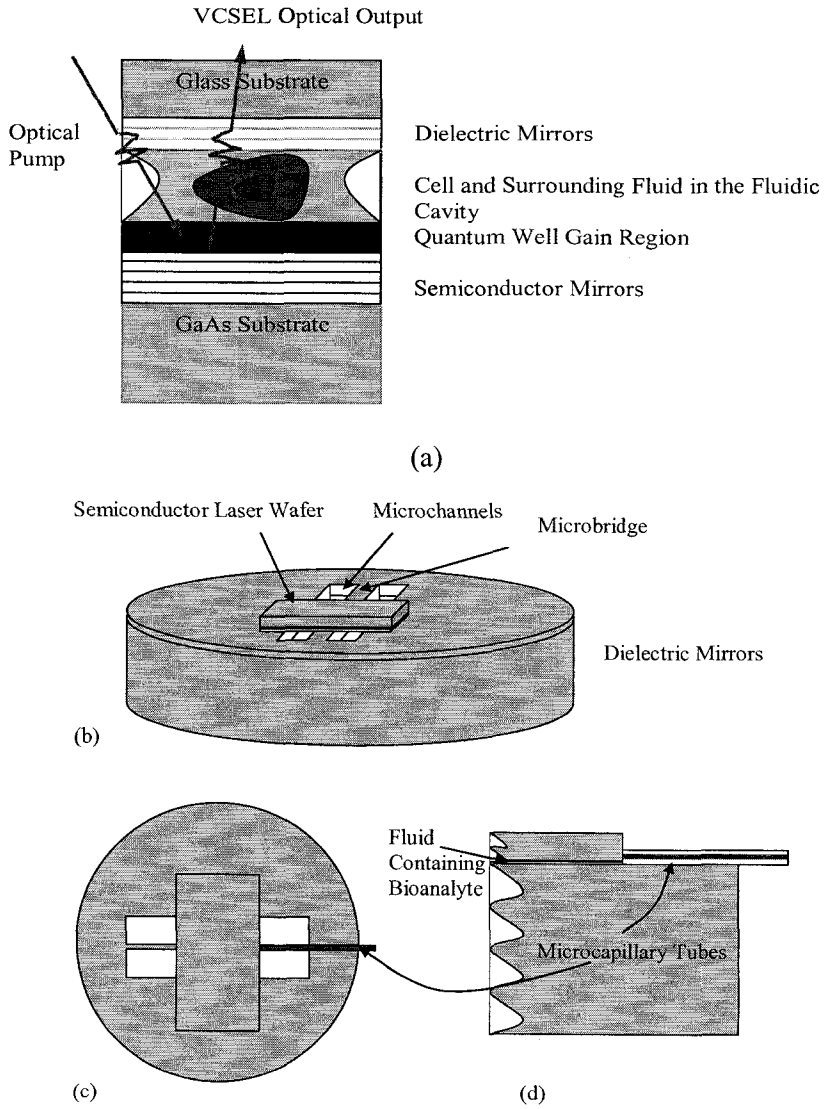

Figure 3.6 Schematic diagram of the optically pumped VCSEL based biosensor developed at Sandia National lab. (a) crossing-section view, (b) perspective view, (c) top view and (d) side view. (Reproduced from reference [11])

The basic idea of this design is that the cell, as a component of a laser resonant cavity, aids the light-generation process. The dielectric properties of various cell components and their surrounding fluids will modify the effective optical path length and consequently change the output wavelength, power and even transverse modes of the VCSEL. They demonstrated that different cell types resulted in multimode laser spectra with mode offset, spacing, and intensity being characteristic of the cell type. A typical spectrum from different types of human blood cells is shown in Figure 3.7.

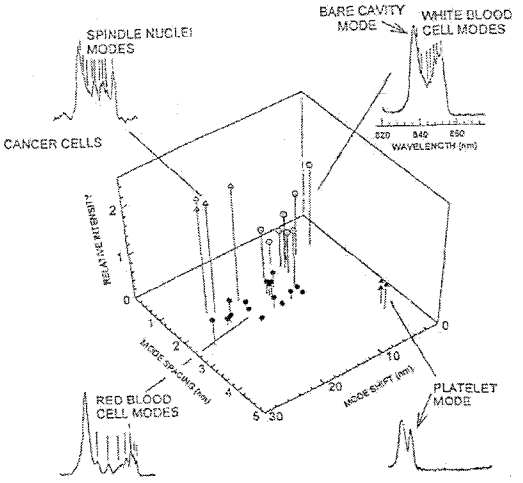

Figure 3.7 Representative spectra for 4 different cell types and cluster plot for identifying cell types. (Reproduced from reference [11])

The spacing and intensity distributions of the spectral peaks of the VCSEL output yield a unique spectral signature for each type of the cell that cannot be confused with other cells. Therefore, the presence of a cell can be detected. The need for an external

solid-state or other laser to optically pump the VCSEL is suitable for proof-of-concept experiments, but increases the size and cost of such sensor. In the next section, a simplified, lab-on-a-chip type fluidic sensing system, employing an electrically pumped VCSEL will be presented.

3.2.2 Electrically injected laser based biosensor

Following the development of the optically pumped laser based biosensor designed in Sandia National Laboratories, our group subsequently developed a fluidic intracavity laser diode (FILD) sensor based on intracavity spectroscopy using an electrically injected, microfluidic, vertical external cavity surface emitting laser (VECSEL) [1]. Figure 3.8 shows a cross-sectional schematic diagram and a top-view photograph of the VCSEL based FILD sensor.

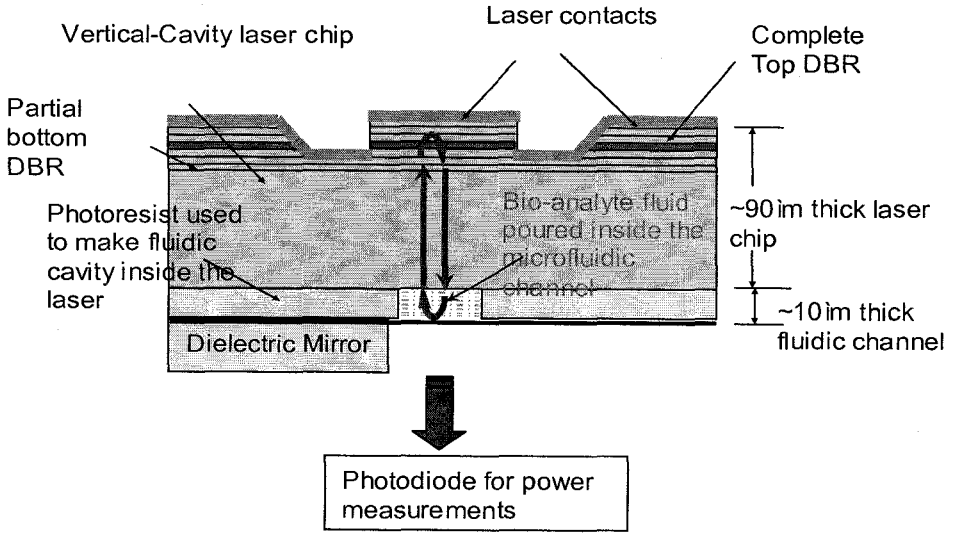

(a)

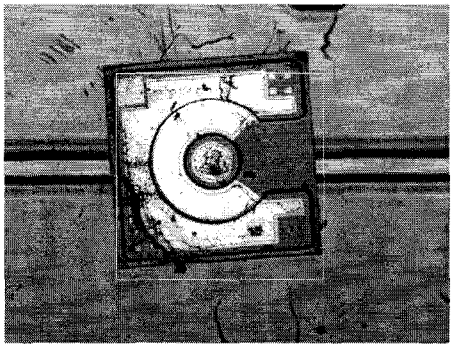

(b)

Figure 3.8 (a) Schematic cross-section of the completed VCSEL based FILD sensor, (b) photographic top-view of the FILD sensor with half VCSEL integrated on top of a microfluidic channel. (Reproduced from Reference [1])

The FILD sensor was constructed from a VCSEL chip and external mirror using an intervening patterned photoresist layer (AZ 5540) to define the fluidic channel. The VCSEL chip, provided by Novalux, Inc., was originally designed for external cavity surface emitting laser diodes called NECSELs [15]. It consisted of a thinned GaAs substrate, a bottom, partial, n-type distributed Bragg reflector (DBR), multiple InGaAs quantum well active region designed for operation at 980 nm, and a top, complete, p-type DBR. The bottom, n-type DBR has a relatively low reflectivity (~80%) compared to conventional VCSEL DBRs (~99%). Thus a ~99% reflectivity, external dielectric mirror on a BK7 substrate is attached to the bottom of the VCSEL chip substrate to complete the coupled cavity laser diode. The use of a partially reflecting n-type DBR between the external cavity and the quantum wells is a compromise to reduce the effect of external cavity losses while still allowing higher circulating power in the external cavity. The external mirror's high reflectivity is compatible with the minimal output power requirements of the sensor function.

A particularly straightforward photoresist gasket process [16] was used to define the microfluidic channels. The 1 mm x 1 mm VCSEL chip was aligned to a 100 μm wide channel and attached to the photoresist by heating the assembly for 20 seconds at 125°C on a hotplate. A sealed fluidic cavity, through which liquid analyte including biological samples will flow, was thus formed between the dielectric mirror and laser diode. Fluids with different refractive indices have been introduced into the FILD sensor. Significant modulation of laser power vs. current characteristics with changes in fluid refractive index has been measured with the results shown in Figure 3.9. Larger fluidic index inside the cavity is observed to decrease the laser threshold with an increase in slope efficiency. However effective spectral changes due to transverse confinement in biological cells are still under investigation.

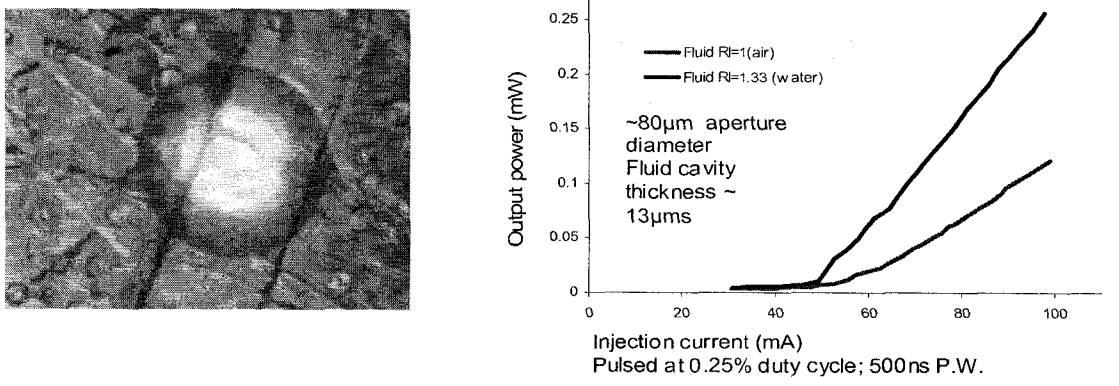

(a) (b)

Figure 3.9 (a) Picture showing modulation of laser intensity due to flow of water inside the laser cavity, (b) Output power vs. injection current characteristics of the laser diode for two different refractive indices of the fluidic cavity. (Reproduced from reference [1])

Both the optically pumped and electrically injected VCSEL based intracavity fluidic biosensors discussed above are classified as active devices because they can form a laser resonant cavity and convert electrical energy into light. The active laser based intracavity

spectroscopic biosensors investigated thus far require relatively high gain to overcome the losses associated with the introduction of the fluidic cavity leading to the requirement for optical pumping or relatively complicated fabrication.

3.2.3 Micro-fluidic photonic crystal laser

In the above work the flow structures are all fabricated outside the VCSEL and the direction of flow is restricted to the horizontal direction. Researchers at UIUC recently demonstrated the first monolithic micro-fluidic photonic crystal VCSEL [17], wherein the micro-fluidic channel lies within the VCSEL as shown in Figure 3.10 (a). The photonic crystal pattern serves a dual purpose of acting as the vertical micro-channels, and also helps in achieving single mode operation. The vertical channels are connected to the underlying horizontal channel, which is created by selectively etching a buried oxide layer. Continuous-wave measurements were performed by introducing acetone in the VCSEL. Figure 3.10 (b) shows the optical spectra during and before the introduction of acetone operating at three times threshold. The sensing mechanism of the micro-fluidic VCSEL and further applications in biosensing are still under investigation according to the UIUC group.

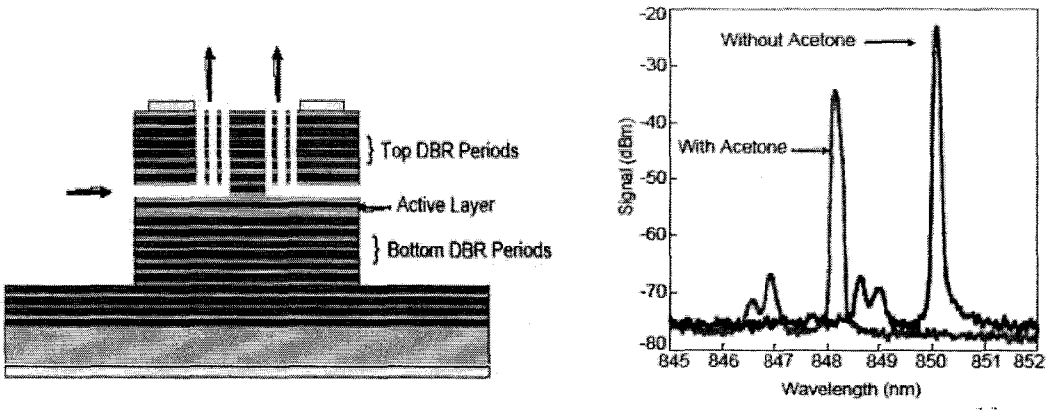

Figure 3.10 (a) Cross-section of micro-fluidic photonic crystal VCSEL Photonic crystal hole pattern creates vertical micro-channel; etched oxide layer creates horizontal channel; (b) Optical spectrum with and without flow of acetone in micro-channels. (Reproduced from reference [17])

3.2.4 External cavity laser based biosensor

Another work on intracavity spectroscopic biosensor was done by a research group at Nanyang Technological University of Singapore in 2005. They integrated a laser diode, a micro-lens, and a microfluidic channel onto a chip monolithically [18], which was able to determine the refractive index of living cell in real time without any cell labeling and chemical treatment. Figure 3.11 shows the schematic side view of the integrated biochip and the refractive indices measurement results of some cancerous cells. This design suffers from the drawback of low wavelength shifts induced by the cells from the bare cavity mode, which inevitably increase the system cost due to the need for a high resolution spectrometer in order to resolve the minor shift. This biosensor utilized a coupled cavity concept, but the extended cavity length decreased the perturbation effect of the cell on the cavity spectrum.

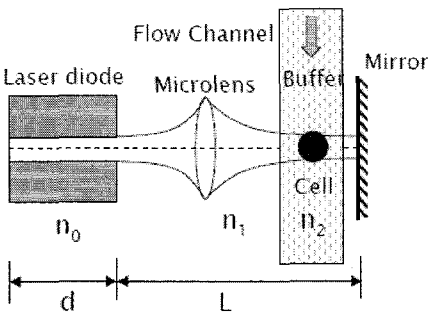

Beads & Cells	l (μm)	Δl	$\Delta\lambda$ (nm)	RI
Culture Medium	-	-	-	1.350
HeLa	17.66	1	0.08	1.392
PC12	11.11	0	0.03	1.395
MDA-MB-231	18.72	1	0.03	1.399
MCF-7	17.48	1	0.02	1.401
Jurkat	12.82	0	0.07	1.390

(a) (b)

Figure 3.11 (a) schematic side view of the integrated biochip, (b) refractive indices measurement results of cancerous cells. (Reproduced from reference [18])

3.2.5 Microfluidic fiber optic biosensor

To eliminate uncertain factors and ensure high accuracy of refractive index measurement of real cells, the Singapore group followed up with a new design based on a passive on-chip Fabry-Pérot cavity in late 2006. Figure 3.12 shows the schematics of their chip design.

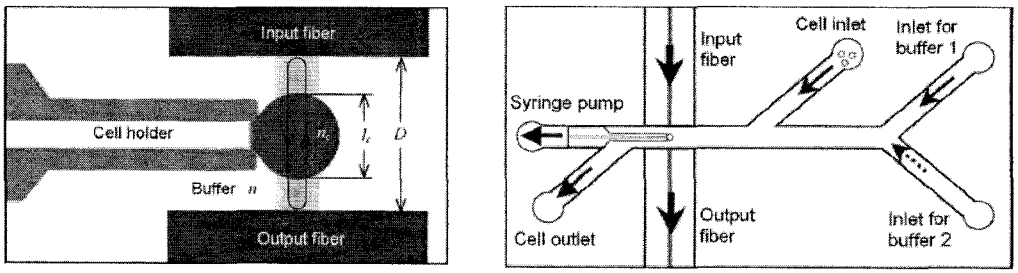

(a) (b)

Figure 3.12 (a) Working principle of a microfluidic Fabry-Perot cavity for cell detection, and (b) Device structure. (Reproduced from reference [19])

The value of refractive index and the size of single cell were determined using a differential method, which measured the spectral shift in response to the buffer change

and the cell presence/absence. Typical cell spectra are shown in Figure 3.13. However, their analysis neglected multimode operation induced by the cell.

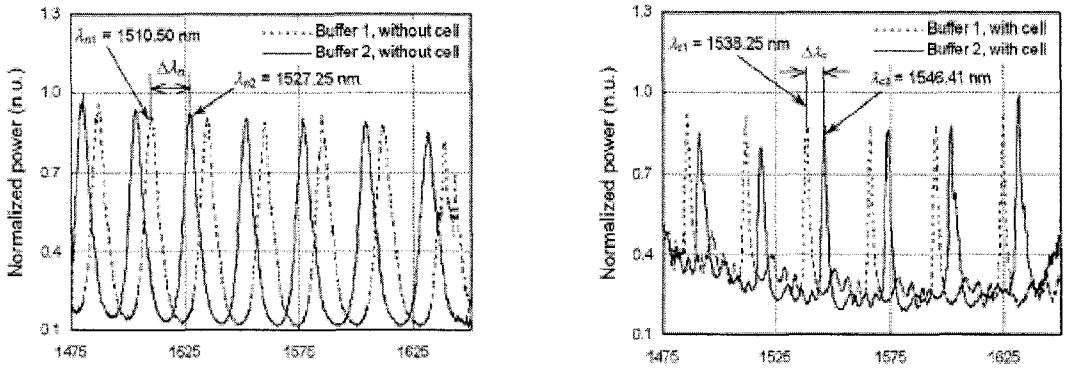

(a) (b)

Figure 3.13 Measured optical spectra in response to the change of buffer and the presence/absence of the cell. (a) The transmitted spectra in the absence of the cell for two buffers. (b) The transmitted spectrum in the presence of the cell for two buffers. n.u. stands for normalized unit. (Reproduced from reference [19])

3.3 New sensing concept

This project utilizes optical refraction and diffraction effects to produce characteristic intracavity transmission spectra of single biological cells in an optical resonator. It is motivated in part by the benefits of a passive cavity interferometric system that retains mode spectrum dependence on cells in a resonator but does not require laser gain media inside the cavity. An OFIS biosensor was designed and fabricated in etched microfluidic channels in glass substrates as a test bed for intracavity spectroscopy of single polystyrene beads and single biological cells. Instead of using laser as the excitation source, transmission spectra are obtained by illuminating the passive cavity system with an external continuum light source such as an LED or bright incandescent source easing

the requirements on cavity finesse and loss. The passive cavity based intracavity spectroscopic biosensor is also expected to simplify the analysis of cell induced transverse mode spectral changes by eliminating the complexities associated with an active laser cavity such as mode confinement factors, material gain, and various losses.

3.4 Summary

This chapter reviewed prior work in single cell detection using active VCSEL based biosensors. The concept of the passive interferometer based biosensor motivated by the active laser based sensors was presented to give the reader an understanding of the state of single cell intracavity spectroscopy.

References

[1] D. Kumar, H. Shao, and K. L. Lear, "Microfluidic cavity surface emitting laser based biosensor", *IEEE LEOS Conference*, vol. 1, pp. 118, 2004.

[2] http://www.mellesgriot.com

[3] http://www.meos.com

[4] R. A. Briones, L. O. Heflinger, and R. F. Wuerker, "Holographic microscopy", *Appl. Opt.*, vol. 17, pp.944, 1978.

[5] G. J. Sloggett, "Fringe broadening in Fabry-Perot interferometers", *Appl. Opt.*, 23(14), 2427-2431, 1984.

[6] C. S. Vikram and M. L. Billet, "Aberration limited resolution in Frauhofer holography with collimated beams", *Opt. Laser Technol.*, vol. 21, pp.185, 1989.

[7] A. E. Siegman, *Lasers*. Mill Valley, CA: University Science, 1986, Chapter 21.

[8] A. Katz, A. Alimova, M. Xu, E. Rudolph, M. K. Shah, H. E. Savage, R. B. Rosen, S. A. McCormick, and R. R. Alfano, "Bacteria size determination by elastic light scattering", *IEEE J. of Selected Topics in Quantum Mechanics*, vol. 9, no. 2, pp. 277-287, 2003.

[9] P. L. Gourley and M. F. Gourley, "Biocavity lasers for biomedicine", *Trend Biotech.*, vol. 18, pp.443-448, 2000.

[10] K. E. Meissner, P. L. Gourley, T. M. Brennan, B.E Hammons, and A. E. McDonald, "Intracavity spectroscopy in vertical cavity surface-emitting lasers for micro-optical-mechanical systems", *Appl. Phys. Lett.*, vol. 69, no. 11, pp.1517-1519, 1996.

[11] P. L. Gourley and A. E. McDonald, "Vertical cavity surface-emitting laser scanning cytometer for high speed analysis of cells", *Proc. SPIE,* vol. 2679, pp. 132-141, 1996.

[12] P. L. Gourley and A. E. McDonald, "Semiconductor microlasers with intracavity microfluidics for biomedical application", *Proc. SPIE,* vol. 2978, pg. 186-196, 1997.

[13] P. L. Gourley, T. French, A. E. McDonald, E.A. Shields, and M. F. Gourley, "Ultrasensitive detection of red blood cell lysing in a microfabricated semiconductor laser cavity", *Proc. SPIE,* vol. 2978, pp.195-206, 1998.

[14] P. L. Gourley, J. D. Cox, J. K. Hendricks, A. E. McDonald, G. C. Copeland, and D. Y. Sasaki, "Semiconductor microcavity laser spectroscopy of intracellular protein in human cancer cells", *Proc. of SPIE*, vol. 4265, pp. 113-124, 2001.

[15] http://www.novalux.com/

[16] T. Yu, T. Ao, K. Hartinger, H. Shao, C. W. Wilmsen, K. L. Lear, K. M. Geib, and S. A. Feld, "Electrically pumped fluidic cavity (EPFC) VCSEL for the detection of biologic agents", *Proc. SPIE*, vol. 4994, pp. 206-215, 2003.

[17] K. Samakkulam, J. Sulkin, A. Giannopoulos, and K. D. Choquette, "Micro-fluidic photonic crystal vertical cavity surface emitting laser", *Electron. Lett.*, vol. 42, no.14, 2006.

[18] X. J. Liang, A. Q. Liu, X. M. Zhang, P. H. Yap, T. C. Ayi, and H. S. Yoon, "Determination of refractive index for single living-cell using integrated biochip", *the 13th Intemational Conference on Solid-State Sensors*, Actuators and Microsystems, Scoul, Korea, 2005.

[19] W. Z. Song, X. M. Zhang, A. Q. Liu, C. S. Lim, P. H. Yap, and H. M. M. Hosseini, "Refractive index measurement of single living cells using on-chip Fabry-Pérot cavity", *Appl. Phys. Lett.*, Vol. 89, 203901, 2006.

Chapter 4

Biosensor Design and Fabrication

In order to achieve the desired sensor performance, the device structure has to be carefully designed and fabricated. This chapter talks about the fabrication process for the prototype microfluidic Fabry-Pérot (FP) cavity in Pyrex glass. Section 4.1 discusses the material selection of microfluic FP cavity followed by a detailed description of the fabrication processes in Section 4.2. Section 4.3 describes the microscopic and spectroscopic characterization of the optofluidic biosensors.

4.1 Material selection and design

Various microelectromechanical system (MEMS) based lab-on-a-chip analytical systems have been recently developed for the analysis of biological samples such as proteins, cells, and DNA. Microfluidic FP cavities are being developed for a wide range of applications, including microsphere spectroscopy [1], biocavity lasers [2], microcavity fluidic dye lasers [3], and optical FP filters [4]. For all these applications, the system performance is highly dependent on device fabrication techniques. Considerable attention is now directed towards simplifying and improving the reliability of the manufacturing steps.

Glass-based microfluidic devices, especially those coated with reflective thin films inside the etched channels, are very attractive for microcavity spectroscopic applications. Detection of microstructures within the cavity is based on the optical resonant frequencies of the fluidic cavity, which are determined by the cavity geometry.

Therefore, cavity stability is a major factor in the system performance. Compared to polydimethlysiloxane (PDMS) and other soft polymers, glass offers better rigidity and easier control of surface properties, which make it desirable for applications that require robust and stable surface characteristics and a wide optical transmission range. Table 4.1 lists the major properties of various types of glasses, among which Pyrex 7740 is the most popular glass type for microfluidic applications. Therefore, Pyrex 7740 (1"x1.5"x0.7mm) was used to form the microfluidic channels in this thesis work.

Table 4.1 Properties of glasses. [http://www.valleydesign.com]

Glass type	Refractive index (l=582.1nm)	Thermal coefficient expansion	Hydrolytic resistance	Acid resistance
BK7 Schott glass	1.509	7.0×10^{-6}/°C	class 2	class 1
Pyrex 7740	1.473	32.5×10^{-7}/°C	class 1	class 1
Soda-lime glass	1.513	8.6×10^{-6}/°C	class 3	n/a
Fused quartz/silica	n/a	n/a	n/a	n/a
Borofloat glass	1.47	3.25×10^{-6} K^{-1}	class 1	class 1

4.2 Fabrication

In this thesis work, microchannels were wet etched into glass substrates using a standard photolithographic process. Two patterned glass wafers were then sealed using a thermo compressive gold-to-gold diffusion bonding technique. This method has several advantages over present microfluidic FP cavity fabrication methods in manufacturing complexity, surface smoothness, cavity rigidity, and bonding temperature. First of all, it makes use of the etching mask as intermediate bonding layers, which greatly simplifies the fabrication process by eliminating complicated and strict wafer cleaning processes. Secondly, using gold as a bonding layer is compatible with

dielectric or other metallic mirror coatings to be incorporated in the channels to make high finesse FP cavities as long as the coatings are limited to the channel bottoms. For example, while gold provides high reflectivity in the near-infrared, silver or aluminum would be more suitable in the visible range, and dielectric coatings could provide low loss reflectors across the spectrum. Furthermore, the bonding temperature of 350°C for the present work is much lower than for glass-to-glass direct wafer bonding, which requires a bonding temperature of 580°C for soda-lime glass [5], or 500°C to 650°C [6-8] for borosilicate glass. Finally, the surface property of the etched channel is much easier to control than with PDMS. The gold coating and sealing layer can be further patterned to facilitate the integration of metallic electrodes, which will make it suitable for dielectrophoresis experiments. The following few sections will discuss the detailed process flow for fabricating sealed, microfluidic FP cavities in a Pyrex glass substrate.

4.2.1 Photomask design

The photomask was designed using a commercial software package Freehand 10 and then printed on transparencies using high resolution printers. Two mask printing services were used in this work based on the resolution of the mask designs. Photomasks with a minimum feature size above 50 μm were printed with a high resolution printer (2400 dpi) at the Fort Collins High School's printing center. Masks with minimum feature size below 50 μm were printed at the Photoplot Store in Colorado Springs. Detailed information about photomask design and data conversion was discussed in Appendix F.

4.2.2 Channel definition and mirror formation

The first generation of microfluidic FP cavities was coated with thin gold films due to the unavailability of dielectric coating machines. The 2nd generation of chips was coated with broadband HfO_2/SiO_2 dielectric mirrors with a reflectivity of 96% at a water interface. The following paragraphs talk about the fabrication of the 1st generation chips, followed by a revised process for the 2nd generation chips.

Fabrication of thermo compressively bonded, microfluidic FP cavities began by wet-etching channels into glass substrates using a Cr/Au/photoresist mask as illustrated with cross-sectional diagrams in Figure 4.1 (a-g). The Pyrex glass substrates were first cleaned with acetone, methanol, and de-ionized (DI) water prior to the deposition of etch masking layers. A thin, 35nm, Cr layer followed by a 120 nm gold layer were e-beam evaporated on the glass substrate. The Cr layer was included to increase the adhesion between the gold film and the glass substrate. Shipley PR1818 photoresist was spun on the Cr/Au coated glass substrate at 4000 rpm and UV exposed with an energy density of 15 mJ/cm^2 for 11 seconds. The mask used for the photoresist exposure was a high resolution (1500 dpi) laser printed transparency containing patterns for channel widths of 50 to 280 μm. The exposed, positive tone photoresist over the channels was removed with AZ400K developer for 45 seconds. The underlying gold was then etched in commercial etchant consisting of potassium iodide and a mixture of cerium nitrate. Subsequently, the Cr over the channel was etched with nitric acid. Leaving the patterned photoresist as a protective layer for the gold mask, the whole wafer was dipped into 49% HF at room temperature for 2 minutes. A channel depth of 15 μm was obtained, as measured by a surface profilometer. The observed channel edges are curved due to

the undercut of the metal mask during the wet etching step. Consequently, the actual channel width is larger than the designed value by 30 μm as a result of the isotropic etching of glass by the hydrofluoric (HF) solution [9]. Narrow channels with large aspect ratios could be fabricated without undercut by using dry etching followed by an optional, brief wet etch f necessary to improve the roughness of the etched channel. For completely dry etching, the minimum channel width would be determined by lithographic constraints and the anisotropy of the etch.

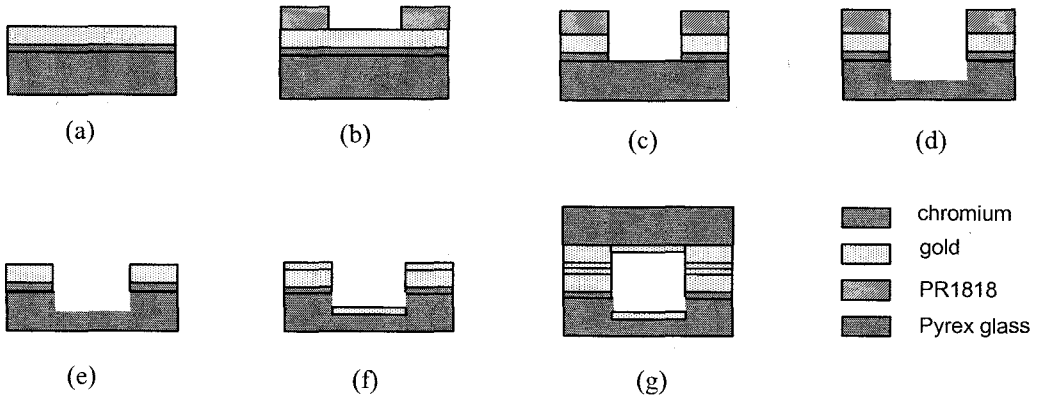

Figure 4.1 Schematic diagram of the device fabrication process. (a) Cr/Au evaporation (b) photolithography c) Cr/Au wet etching (d) glass wet etching (e) photoresist removal (f) mirror coating (g) wafer bonding

The other, unetched, Pyrex glass sample was prepared for the superstrate at the same time as the substrate containing the etched channel. The superstrate was fabricated in a nearly identical process as that used for the substrate including etching of the metal layers in the channel region, but without etching the glass layer. The thin gold mirror layer was evaporated on the superstrate at the same time as the substrate in order to keep the substrate and superstrate mirror layer thicknesses and thus optical reflectivities matched as this provides a higher finesse FP cavity.

4.2.3 Thermo compressive gold-to-gold diffusion bonding

Controlling the cavity length and the parallelism between the superstrate and substrate requires strong bonding. However, most of the currently developed FP microfluidic cavities use either a micro bridge without wafer bonding [1], [2] or are sealed with photoresist [3], [4] or photo definable epoxy [10], which might cause clogging of the channels as discussed in section 2.6.2. Considering the complexity and quality of various wafer bonding techniques, the patterned reflectors were bonded together using a thermo compressive gold-to-gold diffusion bonding technique [11] in this work. This section talks about the details of the bonding of microfluidic FP cavities in glass.

The schematic diagram in Figure 4.2 (a) shows the bonding of the glass substrate and superstrate including Au mirror coatings in the channel. Strong bonding was obtained by applying pressure to the glass samples by clamping them between aluminum plates shown in Figure 4.2 (b). Four bolts at the corners of the plates were tightened using an Allen wrench to apply a torque of approximately 130 lbs. in. Prior to the final clamping, the superstrate and substrate were aligned under a microscope system with the help of alignment marks visible through open holes in the plates.

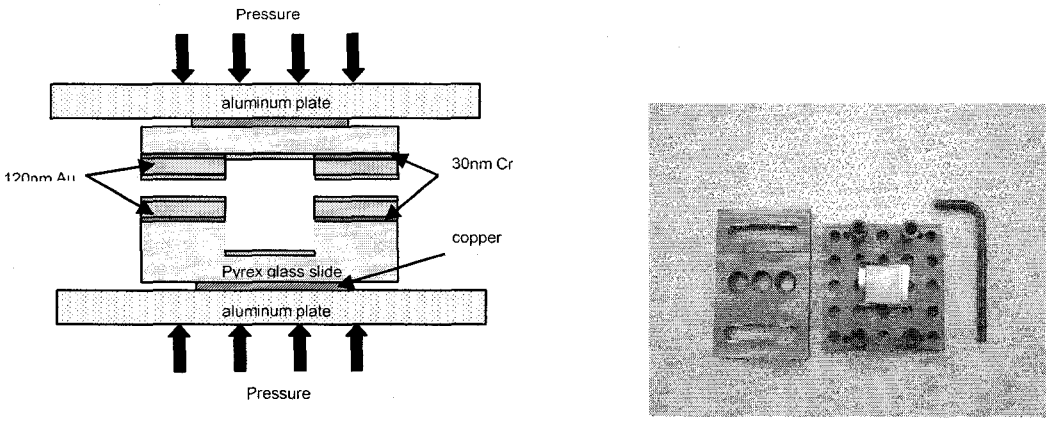

(a) (b)

Figure 4.2 (a) Schematic diagram of thermal compressive gold-gold diffusion bonding, (b) Optical plates that were used to apply pressure to the glass substrates.

Shearing test and subsequent failure analysis showed that bonding occurred primarily on the outer edges of the sample using the apparatus discussed above. This is attributed to the bolt placement at the corners of the plate causing minute bowing in the plates and thus greater pressure near the edges of the sample. In order to deliver force more uniformly to the central part of the glass substrates, two small (1.85 cm x 1.85 cm x 0.142 cm) polished copper sheets were inserted between both glass and aluminum interfaces. Other researchers have suggested the use of temporary flat metal plates in the initial bonding process for thermo compressive glass wafer bonding [12]. The high thermal conductance of copper, 4 times higher than that of the aluminum, promotes more uniform heat distribution across the glass samples as well. An initial bonding process without inserting the copper plates needs to be performed if the patterns on the glass substrate and superstrate need to be aligned by seeing through the clamps. The clamped assembly of the glass samples, copper sheets, and aluminum plates was then put into an oven evacuated to a pressure of about 10^{-3} torr. The sample temperature was gradually

increased over 4 hours to a final temperature of 310-350^{0}C, which was held for 20 minutes before cooling the samples for 2 hours. Strong and homogenous bonding was achieved using this method. The impact of the bonding temperature on the strength of the bonded interface is discussed in Section 4.3.1.

4.2.4 Microfluidic nanoport assemblies integration

Through holes of 1 mm diameter were drilled at the end of the channel by diamond coated bit using a Dremel drill press before bonding the glass superstrate and substrate in order to incorporate nanoports onto the sensor chip to overcome the capillary force induced fluid flow by pressure balancing using syringes at the end ports of the channel. Peek tubing (Upchurch Scientific Inc. N-124H) with an inner diameter of 125μm was used to deliver fluid into the microfluidic channels. Figure 4.3 shows the picture of the syringes and micromanipulator used for fluid flow control.

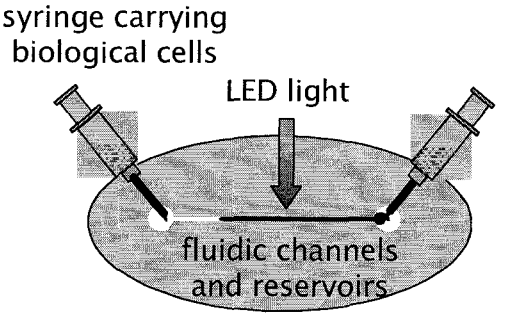

Figure 4.3 Schematic diagram for integrating nanoport assemblies to the optofluidic chip.

4.3 Device characterization

This section presents the detailed characterization of the fabricated biosensor chips by examining critical fabrication steps that affect the optofluidic cavity's performance with

scanning electron microscopy, atomic force microscopy, and optical spectroscopy. Theoretical modeling of cavity finesse reduction due to mirror roughness and tilt will be studied and compared with the measured value.

4.3.1 Bonding strength measurement

Accurate control of the FP cavity length and thus transmission spectrum requires uniform bonding of the substrate and superstrate without an intervening gap that can vary in size. In this work, bonding strength has been used to quantify the quality and completeness of bonding. In order to test the bonding strength, shear tests were performed on three (2 cm x 3 cm) samples bonded at 310^{0}C, 330°C, and 350^{0}C. Table 4.2 lists the shear force per bonded area required to separate the substrate and superstrate as well as the observed failure modes. The observed failure location of the samples indicates that the bonding happens mostly on the outer edges of the wafer at temperatures lower than 350^{0}C. Strong bonding across the entire sample occurs around 350°C, which significantly increases the shear force.

Table 4.2 Shear test of thermal compressive bonding strength

Wafer bonding temperature	Shear force (Newton/cm^2)	Observed failure mode
310^{0}C	3.833	Chromium separates from the glass
330^{0}C	5.767	Gold layers separate
350^{0}C	13.557	Glass fractures

4.3.2 Surface roughness and cavity finesse

Surface roughness of the etched channel was studied by atomic force microscopy (AFM) since roughness affects the optical reflectivity of the mirror coatings, which imposes an upper limit on finesse. Figure 4.4 shows the AFM images taken from the bottom of the etched channel. The measurements indicated a RMS roughness of 1.309 nm and 1.765 nm before and after the gold coating respectively. This surface roughness meets the requirements for optical mirrors, which can be utilized in the intracavity spectroscopy experiments. The detrimental optical effects of various types of mirror defects have been extensively studied [13-15]. In this work, the allowed maximum finesse was calculated using the closed form formula in [14], $F_{total} = \left(F_{ideal}^{-2} + F_d^{-2}\right)^{-1/2}$, where F_d is the surface roughness limit on finesse defined as $F_d = \lambda/\left(2\sqrt{3}\square\right)$ with $\square$ designating the RMS surface roughness and $\square$ is the optical wavelength. From this expression, the RMS surface roughness of 1.765 nm allows a maximum cavity finesse of 145.56. The ideal finesse of the cavity is 43.3 based on the 93% reflectivity of the 35 nm gold mirrors at 890 nm. The resultant total finesse including surface roughness is F_{total} = 41.48. The increased RMS roughness after coating may be caused by small clusters or other defects in the gold layer resulting from the relatively high 0.3-0.4 nm/s deposition rate. Further improvement of the surface roughness can be expected by decreasing the concentration of the HF solution in the wet etching process [16]. A multilayer Cr/Au mask should be used for channel depths larger than 50 μm in order to prevent pinholes in the masked area [17].

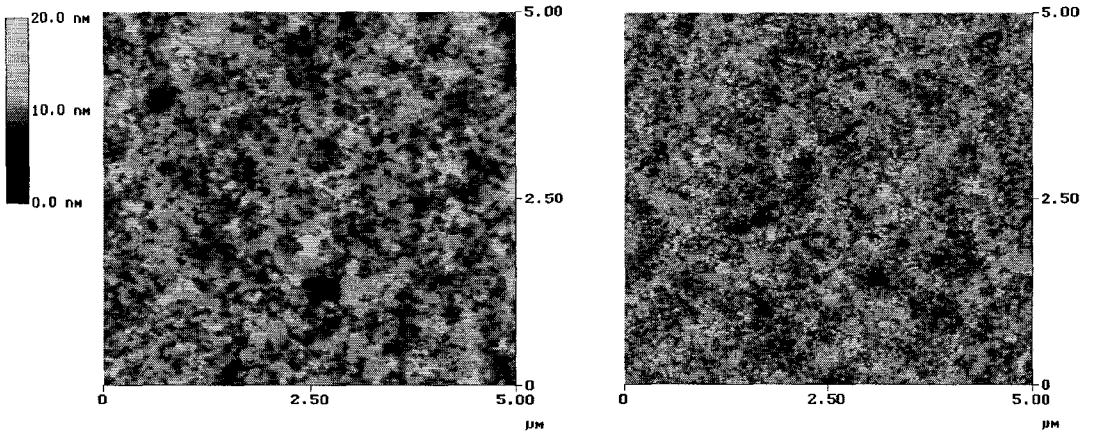

(a) (b)

Figure 4.4 (a) AFM image of a 15 μm deep etched Pyrex glass channel surface before gold coating. The RMS roughness is 1.309 nm. (b) AFM image of an etched channel surface, with a RMS roughness of 1.765 nm, after evaporating a layer of 35 nm gold at a 0.4 nm/sec evaporation rate.

4.3.3 Cross section and cavity length measurement

A scanning electron microscope image of the sealed channel resulting from the 350^0C thermocompressive bonding process is shown in Figure 4.5. The image shows there are no gaps between the metal films in the regions outside the channel. Undercut metal layers are apparent at the edges of the channel. Typical of gold thermocompressive bonding [18] is that the combination of heating and clamping pressure in the vacuum causes atoms to diffuse and mix between the gold layers on the two glass slides, forming a single gold layer that bonds the two parts together. The diffusion process requires clean surfaces to allow intimate contact between the gold layers. The channel layout can also impact the quality of the bonding. Large unetched areas should be provided between channel regions to ensure successful bonding. Designs with channels extending to the sample edge allow trapped air to readily escape from the bonded cavity.

The gold bonded glass technique presented here does allow greater flexibility in channel layout than some other methods. For example, cavities sealed with photosensitive epoxy require a critical bonding temperature to prevent a clog within the channel while still maintaining a strong bonding strength [10].

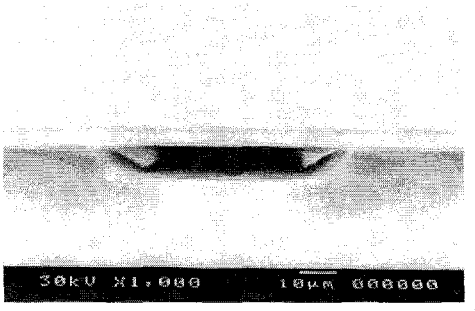

Figure 4.5 SEM picture of a cavity cross-section after thermo compressive bonding. Ordinary glass cover slips were used for making this cavity to simplify cutting the bonded sample in cross-section.

Optical measurements of the microfluidic cavity are useful for verifying the quality of the bonding without resorting to destructive tests required for cross-sectioning. The cavity depth after bonding can be extracted from the transmission spectra based on the wavelength position and spacing of the optical micro cavity modes. Figure 4.6 shows the optical transmission spectra of the FP microfluidic cavity when flood exposed by a broadband microscope white light from the superstrate side while a 62.5 μm core diameter multimode optical fiber was used to collect the transmitted light on the opposite side. The figure shows spectra for both an air filled and water filled channel. The shift in the spectrum corresponds to an increased optical thickness due to the refractive index of water. The broadband microscope white light excites several longitudinal modes in

the transmission spectra, which makes the cavity depth measurement more accurate by fitting a large number of modes with the theoretical simulations. TFCalc, a thin film design software package, was used to simulate the cavity transmission spectrum for the air filled cavity with the results presented in Figure 4.6. A cavity length of 14.828 μm predicted by fitting the etches depth and the measured depth of the bonded cavity indicates the accurate simulation result to the experimental spectra corresponds very well with the etching depth of 15 μm measured by the surface profiler. The good correspondence between the measured cavity length control that is available using the method presented in this paper. Other methods may have greater variation between the designed and measured cavity lengths. For example, an uncertainty of 1 μm in the thickness of the bonding layer of a 15 μm deep microfluidic dye laser cavity, formed and bonded using the SU-8 photoresist, was previously reported [3].

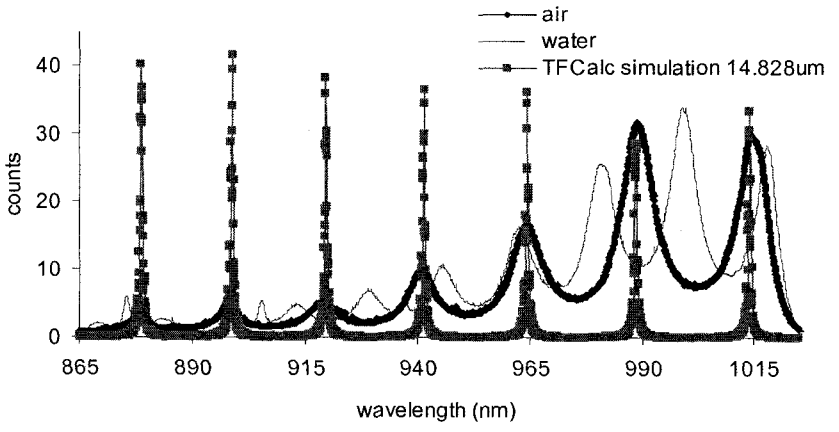

Figure 4.6 Transmission spectra of a bonded microfluidic cavity filled with water and air respectively flood exposed by a broadband microscope white light. Also shown is a TFCalc simulation of the transmission spectra of the microfluidic Fabry-Pérot cavity after the thermocompressive bonding.

4.3.4 Mirror parallelism and cavity finesse

Uniform clamping forces and a smooth bonding interface are required to assure the parallelism between the superstrate and the substrate. . In this work, the parallelism between the top and bottom cavity mirrors after the bonding process was determined from the variation in the absolute cavity length as a function of position along the microfluidic channel. Figure 4.7 shows the transmission spectra taken at 7 different positions in a 200 μm wide, ~25 μm deep microfluidic cavity filled with water. The transmitted light is collected from a circular spot of approximately 10 μm in diameter by adjusting the focus of a customized microscope system shown in Figure 4.10. The absolute cavity length at each position can be calculated using $L_{cav} = c/(2n\Delta\nu)$, where $\Delta\nu$ is the frequency difference of two neighboring longitudinal modes of the FP cavity, c is the speed of light in air, and n = 1.33 is the refractive index of the water inside the microfluidic cavity. The deeper microfluidic cavity and larger refractive index used in this experiment allows many longitudinal modes in the transmission spectra, which increases the accuracy of the cavity length measurement and thus the mirror tilt angle calculation. The RMS value of $\Delta\nu$ for each spectrum is extracted from the curve and listed in Table 4.3 along with the corresponding cavity length. The cavity mirror-tilting angle is calculated from $\theta_{tilt} = arctan\ (\Delta L_{cav}/\Delta x)$. Here ΔL_{cav} is the cavity length change from one position to the other position, and Δx is the distance between the two positions. The maximum tilt angles calculated from Table 4.3 are 0.095^0 and 0.053^0 in the direction transverse to and along the channel layout respectively.

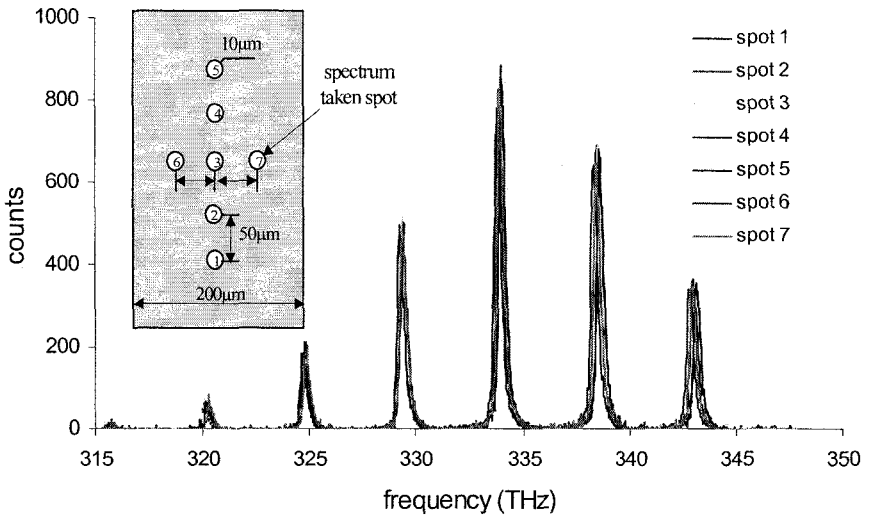

Figure 4.7 Transmission spectra taken at 7 different spots in a 200 μm wide, ~25 μm deep microfluidic cavity filled with water after the thermo compressive wafer bonding. The inserted plot shows the spectra taken positions.

Table 4.3 Fabry-Pérot cavity mirror parallelism measurement

Detection position	Peak 1 (THz)	Peak 2 (THz)	Peak 3 (THz)	Peak 4 (THz)	Peak 5 (THz)	Peak 6 (THz)	RMS □ν (THz)	L_{cavity} (μm)
1	320.119	324.815	329.334	333.875	338.598	342.959	4.570	24.679
2	320.085	324.633	329.243	333.875	338.432	342.959	4.575	24.652
3	320.113	324.721	329.337	333.905	338.501	343.065	4.590	24.569
4	320.198	324.753	329.37	333.97	338.535	343.175	4.596	24.542
5	320.113	324.78	329.337	333.972	338.535	343.100	4.598	24.531
6	320.113	324.721	329.337	333.875	338.467	343.065	4.590	24.569
7	320.113	324.753	329.234	333.875	338.261	343.012	4.582	24.616

Departures of flat mirrors from perfect parallelism have been studied as a form of surface defect in FP cavities [14]. Mirror tilt induced cavity finesse can be calculated using a closed form formula derived by Sloggett, $F_{tilt} = \sqrt{3}/(\pi\sigma_{tilt}) = \sqrt{3}/\pi(\phi_{\max}/2)$, where $2\phi_{max}$ is the round-trip peak-to-peak phase variation across a circular aperture due

to the non-parallelism of the flat interferometer plates. It can be calculated as $\phi_{max} = (2\pi/\lambda) n (D/2) \tan(\theta_{tilt})$, where D is the effective aperture size, n=1.33 is the refractive index of water inside the microfluidic cavity, and θ_{tilt} is the mirror tilt angle. The allowed maximum finesse, F_{max}, of a tilted mirror FP cavity depends on F_{tilt} and the ideal finesse, F_{ideal}, according to $F_{max} = (F_{ideal}^{-2} + F_{tilt}^{-2})^{-1/2}$. The measured tilt angles of 0.095° and 0.053° correspond to cavity finesses of 31.71 and 38.42 respectively, for an aperture size of 10 μm in diameter and an ideal finesse of 43.28. For intracavity spectroscopy applications, exciting the microfluidic FP cavity using a smaller beam size is an effective way of reducing the mirror titling effects [19]. Consideration of the combined effects of the measured surface roughness and mirror tilt provides a maximum calculated finesse of 30.99, which is in good agreement with the observed finesse of 30.

4.3.5 Cavity finesse improvement

As discussed in Section 3.1.3, FP cavity finesse is affected by the following factors (a) end mirror reflectivity, (b) uniformity of the bonding process, and (c) incident beam collimation. Therefore, care needs to be taken during the design and fabrication of the microfluidic FP cavities in order to improve the cavity finesse.

4.3.5.1 Mirror coating materials and stability

High quality mirror coatings are critical to the proper function of the microfluidic FP cavity. In order to remove the particles left inside the etched channels in the photoresist developing process, a 30 seconds reactive ion etch was performed before the mirror coating. Wet rather than dry etching was primarily used in these experiments to

enhance the smoothness of the etched channel. In this simple, unmasked process, a thin 35 nm gold mirror layer was electron beam evaporated on the entire sample after stripping the photoresist. However, it is found that gold coatings do not have good water resistibility. For example, gold coated microfluidic cavity can only be used 3-4 times by flowing biological analyte and cleaning with DI water immediately after the spectroscopic experiments. Therefore, finding robust mirror materials that are compatible with water and also stable at 350^0C - 400^0C is critical in order to reduce both the fabrication cost and the labor involved. Alternative processes for coatings other than gold are discussed below.

4.3.5.2 Dielectric coated FP cavity fabrication

Mirror coating materials have to be chosen carefully in order to endure the thermo compressive bonding temperature. Dielectric or a variety of metallic mirror coatings, such as aluminum or silver, can also be deposited in the channel without interfering with the gold surfaces for bonding, by slightly modifying the fabrication steps. In this case, the steps through channel etching would be carried out as described above, but the etch masking photoresist would be left in place while the mirror coating is deposited in the exposed channel. The photoresist can then be used to lift off the mirror coating material outside the channel, leaving the underlying gold exposed for subsequent bonding. The mirror deposition temperature must be kept below the photoresist reflow temperature to allow optimum lift off. In the process developed in this work, only the etched channel portions are optically transparent or selectively coated with thin film mirrors so that light will be blocked outside the channel region.

More robust HfO_2/SiO_2 dielectric mirrors with 13 quarter-wave layers, designed for 96% reflectivity in water at the LED peak wavelength of 890 nm and coated at Dominar Inc. were used for the 2nd generation devices. The fabrication processes were adjusted accordingly as shown in Figure 4.8.

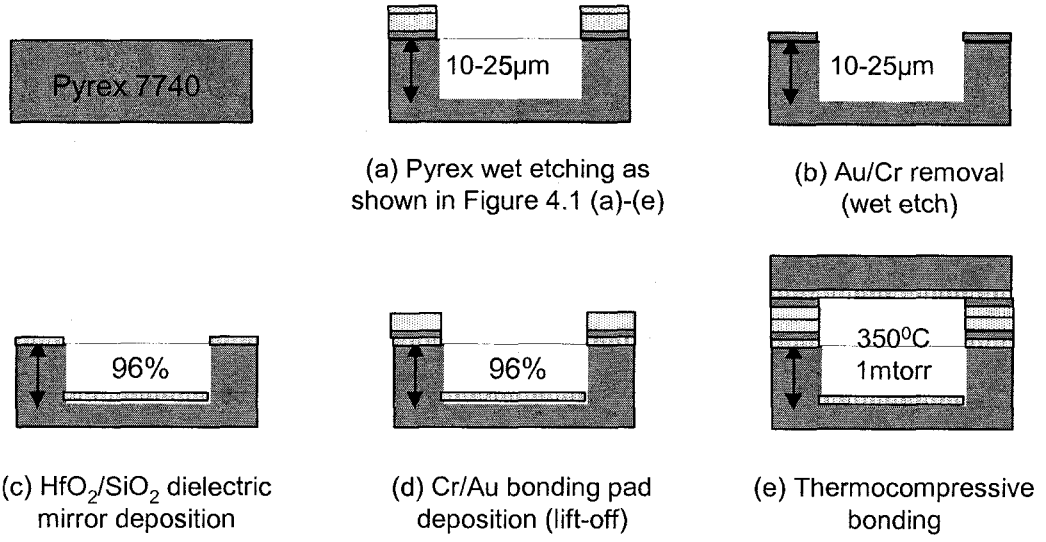

Figure 4.8 Schematic diagram of the 2nd generation chip fabrication process.

In order to understand the amount of improvement on cavity reflectivity due to the change of mirror coating materials, modeling of mirror reflectivity was performed using a commercial thin film modeling software package, TFCalc. Figure 4.9 shows the calculated reflective spectra of a 8.5 pairs of HfO_2 (117.72 nm thick)/SiO_2 (153.44 nm thick) dielectric coating with a reference wavelength of 890nm and a 35nm thick gold mirror. It is clearly shown that the reflectivity of the mirrors was increased from 93% to 97% at an air interface corresponding to the replacement of gold by HfO_2/SiO_2. Therefore, ideal cavity finesse increases from 43 to 103. Experimentally, an optical finesse of above 40 was obtained for cavities coated with dielectric mirrors.

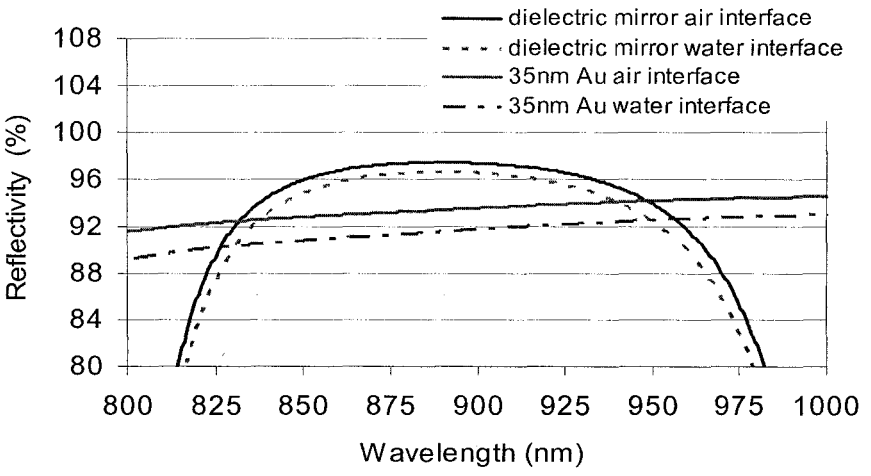

Figure 4.9 TFCalc simulations of the reflective spectra of HfO_2/SiO_2 dielectric mirrors and 35 nm thick gold mirrors on a glass substrate at air and water interfaces.

4.3.5.3 Incident beam collimation

The measured finesse using a broadband microscope light is much lower than corresponding simulations in Figure 4.6 due to the imperfect collimation of the extended source. A customized microscope system, shown in Figure 4.10, was used to analyze the transmission spectra of the microfluidic cavity illuminated by LEDs from the bottom side. The fiber coupled Ocean Optic Spectrometer (HR2000), with a 0.3 nm resolution and a spectral response range of 865 nm~1020 nm, collects the transmitted light. An improved finesse over a narrow band obtained by using a well-collimated high power LED (Hamamatsu L2690-02) as shown in Figure 4.11. Although the LED has a narrower wavelength range than the microscope light, leading to fewer excited longitudinal modes of the cavity, it results in higher finesse. A biconvex lens (f =30mm) collimated the LED light from the bottom side of the microfluidic cavity. The transmission peak at 908.76 nm has a FWHM of ~1.0 nm, corresponding to a cavity

finesse of 30. Further improvement of the measured cavity finesse is expected by exciting the cavity modes with a highly collimated tunable laser source.

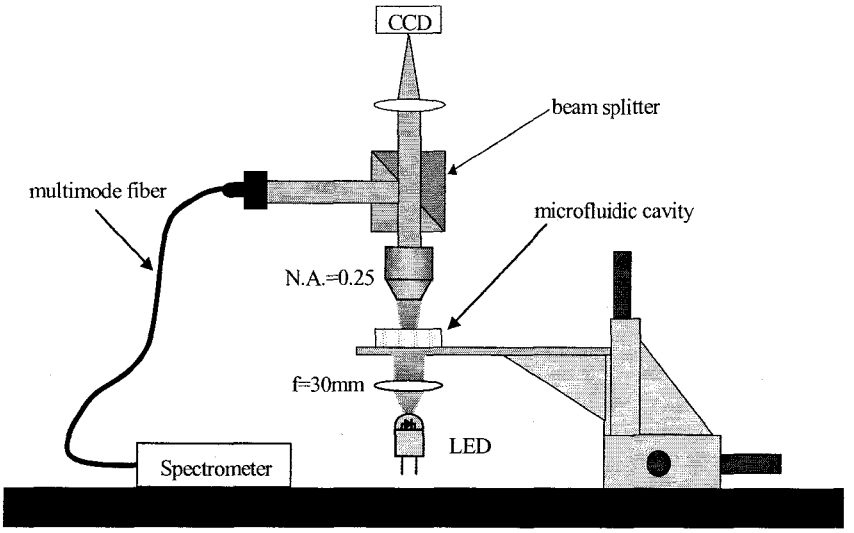

Figure 4.10 Customized microscope system used to measure the optical spectra of the microfluidic Fabry-Pérot cavity.

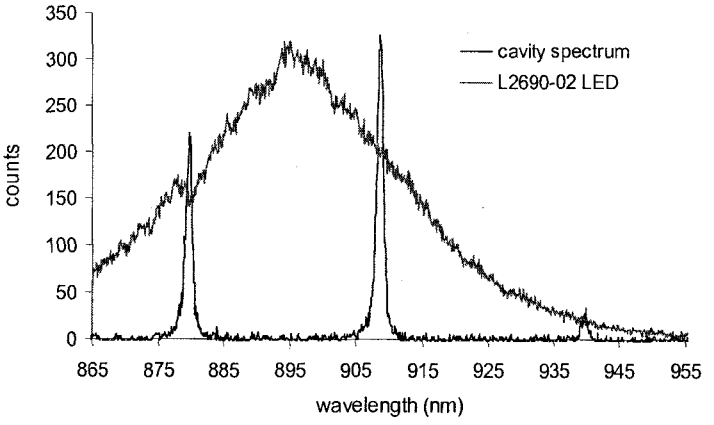

Figure 4.11 Microfluidic FP cavity transmission spectrum illuminated with a well-collimated LED biased with a 100 mA current source. The spectrometer integration time was reduced by a factor of 30 for the LED spectrum in order to match with the intensity level of the microfluidic cavity spectrum.

4.3.6 Integration of DEP traps

To help stabilize cells within the microfluidic cavity, single cell dielectrophoretic (DEP) traps were fabricated within the cavity by patterning ~10 μm wide Cr/Au electrodes as shown in Figure 4.12 [20]. This section presents the corresponding processes for the fabrication of DEP chips.

Robust, uniformly bonded, and > 15 μm deep cavities are highly desirable for the DEP spectroscopic experiments pursued in this thesis work. One plain glass slide and one pre-etched slide with at least 15 μm deep channels are required to allow the cancer cells flow through the cavity after the wafer bonding. Due to the lacking of >15 μm deep dielectric coated channels, new cavities were fabricated by bonding two glass pieces that have ~10 μm deep etched channels. While the undeveloped photoresist along the channel edges caused an electrical short between the DEP electrodes fabricated on the etched slide as shown in Figure 4.12. To further solve the cavity depth problem, a ~6 μm thick AZ4400 photoresist layer was spin-coated on an unetched dielectric coated slide and acted as the interfacial bonding layer to fabricate > 15 μm deep cavities using the available etched slides with shallow channels.

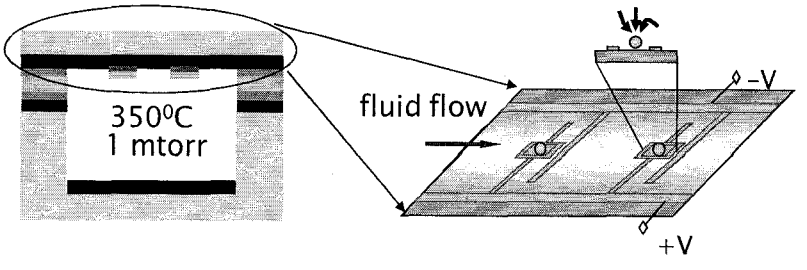

Figure 4.12 Schematics of the proposed DEP trap design.

The following section describes the fabrication processes for DEP integrated optofluidic cavities.

1) Two pieces of dielectric coated glass slides, one with 8 μm~12 μm pre-etched channels and the other unetched piece but with 35 nm/100 nm Cr/Au coatings, were thoroughly cleaned with Piranha solution (98% H_2SO_4 : H_2O_2 = 3:1) and DI water, and finally by N_2 blow drying.
2) The cleaned slides were then dehydrated on a 120^0C hot plate for 5 minutes to remove the remaining solvents.
3) The unetched piece with metallic coatings was first spin coated with Shipley 1818 @ 4000 rpm for 30 seconds. Soft baked on a 95^0C hot plate for 2 minutes followed by an edge bead removal.
4) UV exposure at 150 mJ/cm^2 using a plastic DEP photomask laid on a 4 inch diameter Pyrex glass plate (ordered from University Wafers) using scotch tapes on the edges. The plate was attached to the big mask holder of the aligner by vacuum and then flipped to let the ink side face the sample in order to decrease the interference effects during UV exposure. 10 μm wide lines could be resolved properly by controlling contact between the photomask and the sample.
5) Developing in AZ400K: DI H_2O=1:4 for 20 seconds. Decreasing the exposure power helps decrease the developing time to give better control of the developing process.
6) Etching the Au/Cr layer in the corresponding etching solutions to remove the metallic films uncovered by the photoresist.

7) Finally, the patterned chip was dipped into acetone to remove the photoresist left on top of the DEP electrodes.

8) The other etched piece was spin coated with AZ4400 photoresist at 3000 rpm for 30sec to give a layer thickness of about 7 μm. EV exposed @ 300 mJ and then developed in AZ400K: DI H_2O = 1:4 solution for 2 minutes.

9) The two glass pieces were then aligned under a microscope and clamped using a customized C-clamp as shown in Figure 4.13 to apply pressure uniformly over 1cm x 1cm square at the glass pair center immediately after the alignment.

10) Thermal bonding was done in an annealing furnace flowed with dried N_2 gas at a flow rate of 5 sccm. The temperature ramped from room temperature to 150^{0}C within 15 minutes, holding for 3 minutes at 150^{0}C and then slowly cooled down to room temperature.

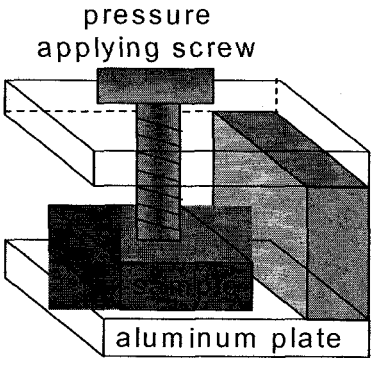

Figure 4.13 Schematics of the customized C-clamp used for applying pressure over the DEP chip.

A HP 8116A function generator was used to generate 14 MHz, 0~16 V peak-peak sinusoidal voltage to trap microspheres and biological cells. The DEP trapping strength is closely related to the refractive indices of the micro particles and the surrounding media, and also the applied voltages. Detailed theories governing the DEP effects will

be presented in Appendix. In this work, microspheres with refractive index of 1.45, 1.49, and 1.59, canine lymphoma cells, and canine peripheral blood mononuclear cells (PBMCs) have been successfully trapped with a moderate AC voltage (~ 10 V). Figure 4.14 shows the schematics of the DEP testing setup and images of the two 15 μm diameter polystyrene spheres trapped with two DEP traps. Initial spectroscopic measurements of the photoresist bonded DEP microfluidic cavities will be presented in details in Chapter 5.

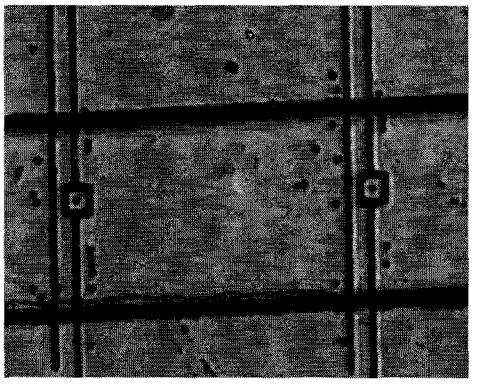

Figure 4.14 DEP traps fabricated on a dielectric coated glass slide after thermo compressive bonding with a photo resist layer. 10 μm diameter polystyrene spheres were trapped by a 10 Vpp AC voltage at 16 MHz.

4.4 Summary

This chapter reports a simple microfluidic channel fabrication process, which can be easily performed using simple fabrication equipment. The microfluidic channels were etched in HF solution on a glass substrate using a Cr/Au/photoresist etching mask resulting in a channel bottom roughness of 1.309 nm. An effective thermo compressive gold-gold bonding technique was used to bond the photolithographically etched glass

substrates inside a 350°C oven in a 10^{-3} torr vacuum. Pressure was applied to the glass pieces by using two aluminum blocks with intermediate copper sheets. This method takes advantage of using Cr/Au layers both as a wet etching mask and as intermediate bonding layers, requiring only one lithography step for the entire process. A parallelism of 0.095^0 was measured, and a finesse as high as 30 was obtained for the 1st generation devices coated with 35nm thick gold using an LED.

The fabrication method is also compatible with the incorporation of dielectric mirror coatings in the channels to form a high finesse Fabry-Pérot cavity. Robust HfO_2/SiO_2 dielectric mirrors were used in the 2nd generation optofluidic Fabry-Perot cavities. The dielectric mirrors are compatible with water and also stable during the thermo compressive bonding process. A cavity finesse of above 40 was obtained using an LED. The low reflectivity of the HfO_2/SiO_2 mirrors allows visual observation and white light imaging, which greatly improves the accuracy of the alignment between DEP traps and the etched microfluidic channels.

The microfluidic cavity developed here can be used in electrophoresis and intracavity spectroscopy experiments. It allows the fabrication of microfluidic FP cavities without using additional spin-on glass layers or other types of UV sensitive glue to bond the glass substrates. It relies only on the metal films already deposited as an etch mask without further material deposition. Good reproducibility has been obtained using cleanroom procedures. Since the method does not require sophisticated polishing and cleaning steps, it should enable a wider range of researchers to fabricate customized microfluidic chips. Furthermore, it can be combined with highly reflective dielectric or metal thin

film optical coatings in the etched channels to perform intracavity microscopy experiments in different wavelength ranges.

Single cell DEP traps integrated into the dielectric mirrors coated optofluidic cavities enable better control of the flowing and the stabilization of cells or microspheres within the cavity. The process developed in this work allows patterning 10 μm wide Cr/Au microelectrodes directly on the unetched glass using low cost transparency photomasks.

In general, the flexibility offered by this fabrication method should extend the applications of the conventional microfluidic FP cavities into chemical and biological spectroscopy experiments.

References

[1] K. E. Meissner, P. L. Gourley, T. M. Brennan, and B. E. Hammons, "Intracavity spectroscopy in vertical cavity surface-emitting lasers for micro-optical-mechanical systems", *Appl. Phys. Lett.*, vol. 69, no.11, pp.1517-1519, 1996.

[2] P. L. Gourley, "Biocavity laser for high-speed cell and tumor biology", *J. Phys. D: Appl. Phys.*, vol.36, pp. R228-R239, 2003.

[3] B. Helbo, A. Kristensen, and A. Menon, "A micro-cavity fluidic dye laser", *J. Micromech. Microeng.*, vol.13, pp.307-311, 2003.

[4] G. Minas, J. S. Martins, and J. H. Correia, "Highly selective optical detection in a lab-on-a-chip for biological fluids analysis", *Sensors and Materials*, vol. 14, no. 2, pp.7-89, 2002.

[5] C. H. Lin, G. B. Lee, Y. H. Lin, and G. L. Chang, "A fast prototyping process for fabrication of microfluidic systems on soda-lime glass", *J. Micromech. Microeng.*, vol.11, pp.726-732, 2001.

[6] I. Rodriguez, P. Spicar-Mihalic, C. L. Kuyper, G. S. Fiorini, and D. T. Chiu, "Rapid prototyping of glass microchannels", *Analytica Chemical Acta*, vol.496, pp.205-215, 2003.

[7] S. C. Jacobson, R. Hergenroder, L. B. Koutny, R. J. Warmack, and J. M. Ramsey, "Effects of injection schemes and column geometry on the performance of microchip electrophoresis devices", *Anal. Chem.*, vol. 66, no.7, pp.1107-1113, 1994.

[8] D. J. Harrison, A. Manz, Z. H. Fan, H. Lusi, and H. M. Widmer, "Capillary electrophoresis and sample injection systems integrated on a planar glass chip", *Anal. Chem.*, vol.64, no.17, pp.1926-1932, 1992.

[9] Z. H. Fan and D. J. Harrison, "Micromachining of capillary electrophoresis injectors and separators on glass chips and evaluation of flow at capillary intersections", *Anal. Chem.*, vol.66, pp.177-184, 1994.

[10] R. J. Jackman, T. M. Floyd, R. Ghodssi, M. A. Schmidt, and K. F. Jensen, "Microfluidic systems with on-line UV detection fabricated in photodefinable epoxy", *J. Micromech. Microengr.*, vol. 11, pp.263-269, 2001.

[11] http://www.nasatech.com/Briefs/Oct02/NPO20076.html

[12] K. T. Turner, M. D. Thouless, and S. M. Spearing, "Mechanics of wafer bonding: effect of clamping", *J. of Appl. Phys.*, vol. 95, no. 1, pp.349-355, 2004.

[13] R. A. Briones, L. O. Heflinger, and R. F. Wuerker, "Holographic microscopy", *Appl. Opt.*, vol. 17, pp.944, 1978.

[14] G. J. Sloggett, "Fringe broadening in Fabry-Perot interferometers", *Appl. Opt.*, vol. 23, no.14,.pp. 2427-2431, 1984.

[15] C. S. Vikram and M. L. Billet, "Aberration limited resolution in Frauhofer holography with collimated beams", *Opt. Laser Technology*, vol. 21, pp.185, 1989.

[16] R. Yokokawa, S. Takeuchi and H. Fujita, "Ultra-smooth glass substrate for bioassay with motor proteins", *Analyst*, vol. 129, pp.850-854, 2004.

[17] M. Bu and T. Melvin, *et al.*, "A new masking technology for deep glass etching and its microfluidic application", *Sensors and Actuators*, pp.1-7, 2004.

[18] http://www.nasatech.com/Briefs/Oct02/NPO20076.html

[19] P. L. Penna, A. D. Virgilio, etc., "Transmittivity profile of high finesse plane parallel Fabry-Perot cavities illuminated by Gaussian beams", *Optics Communications,* vol.162, pp.262-279, 1999.

[20] J. Voldman, M. Toner, M. L. Gray, M. A. Schmidt, "A microfabrication-based dynamic array cytometer", *Anal. Chem.*, vol. 74, pp.3984–3990, 2002.

Chapter 5

Experimental Results

This chapter describes experimental results of single cell detection using the optofluidic intracavity spectroscopic biosensors discussed in Chapter 4. Section 5.1 presents the experimental setup. Section 5.2 presents the experimental microsphere and cell transmission spectra obtained using the OFIS biosensor. Section 5.3 discusses a method for quantitative calculation of the spectral correlation to evaluate the capability of single cell identification using OFIS biosensors. The experimental results indicate that this label-free technique is suitable for differentiating human blood cells and cancerous cells from non-cancerous ones.

5.1 Experimental setup

The OFIS biosensor was fabricated in Pyrex glass substrate using the processes discussed in Chapter 4. Figure 5.1 shows a photographic top view of the sensor and a 200 μm wide channel flowed with 10 μm diameter polystyrene spheres. Microspheres and biological cells were injected into 10~30 μm deep and 200 μm wide fluidic channels through the nanoport assemblies integrated onto the sensor chip and were stabilized within the fluidic cavity by pressure balancing using syringes at the end ports of the channel.

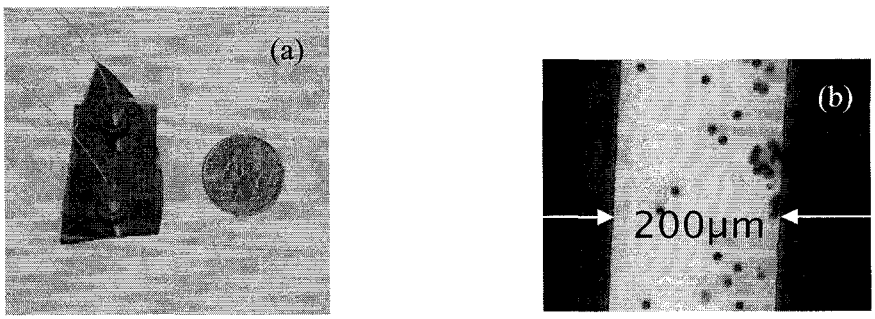

Figure 5.1 (a) Photographic top view of the OFIS sensor beside a quarter, and (b) 200 μm wide microfluidic channels filled with 10μm diameter polystyrene spheres.

Detection and differentiation of cells are based on the transmission mode spectra of cells in fluid-filled Fabry-Pérot cavities. The microsphere/cell loaded fluidic cavity was placed on a xyz stage that can be adjusted and illuminated by a near infrared LED (Hamamatsu L2690-02) with a full width at half maximum (FWHM) of ~30 nm from the bottom side. Imaging of the microfluidic channel onto a multimode fiber served to spatially filter the transmitted light through a customized microscope and select spectra either of individual cells or of the bare cavity for reference as illustrated Figure 5.2. The focal length of the optical system was adjusted to make the light collection spot size, i.e. the image size of the fiber core, approximately 5 to 10 μm in diameter in order to probe single cells inside the fluidic cavity. The transmission spectrum of the fluidic cavity was then analyzed with a 0.3 nm resolution Ocean Optic spectrometer (HR2000).

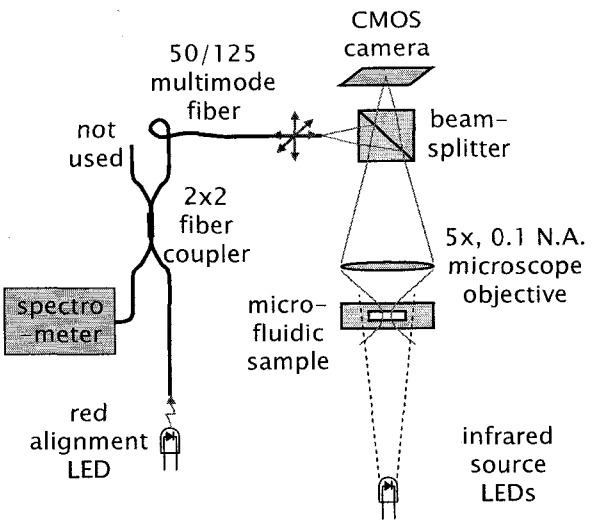

Figure 5.2 The customized microscope system used to measure the transmission spectra of optofluidic cavities.

5.2 Experimental results

As mentioned in Chapter 3, transverse mode spectra of a cell-loaded microfluidic cavity are determined by the refractive index structure of the cell including its type, size, and shape. This section presents the experimental single microsphere and cell spectra.

5.2.1 Spectra of standard microspheres

Initial transmission spectra were obtained from the microfluidic cavity filled with a water suspension of polystyrene microspheres (purchased from Bangs Laboratories, Inc.) as they resembled cells but with well controlled size, shape, and index of refraction. Typical transmission spectra for polystyrene microspheres are presented in Figure 5.3. The spectra clearly show additional narrow transmission resonances, corresponding to the transverse cavity modes, compared to the bare cavity modes (bottom curve). The transverse mode groups are repeated twice, corresponding to two longitudinal modes,

within the wavelength range of the LED. The number of the transverse modes and the spectral differences of neighboring modes provide useful information about the sphere inside the microfluidic cavity.

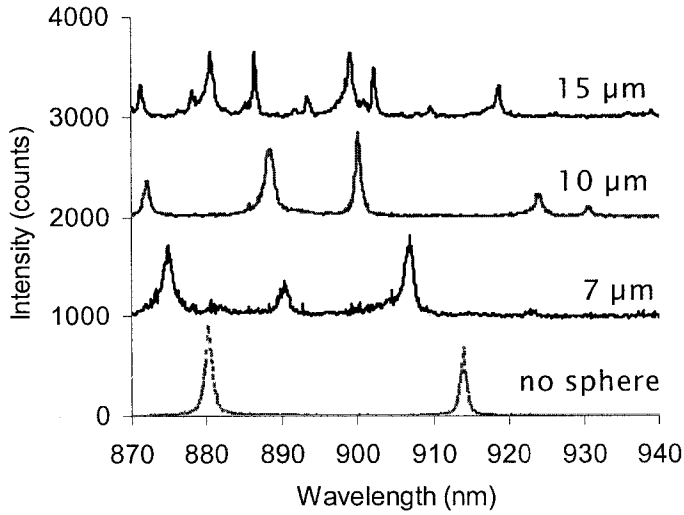

Figure 5.3 Transmission spectra of polystyrene spheres of different diameters within an optofluidic cavity.

Microspheres made from materials other than polystyrene were also investigated by the optofludic intracavity spectroscopy. Table 5.1 summarizes the physical parameters of the microspheres used in this dissertation.

Table 5.1 Standard microspheres used in the spectroscopic experiments.

Sphere type	Refractive index	Diameter (μm)	Standard deviation (μm)	Phase format	Vendor
polystyrene	1.59	2.00	± 0.1		Bangs Laboratories, Inc.
		5 or 5.1			
		7.00			
		9.77	± 0.2	0.5g, 9.7%	
		15 or 15.3	± 0.3		
		15.00	fluorescent labeled		Triton Inc.
PMMA	1.489	6.50		10g, 100%	Bangs Laboratories, Inc.
silica (SiO2)	1.37	5.00		0.5g, 100%	
		5.06	0.42	0.5g, 100%	
soda-lime glass	1.45	11.58	± 0.19		Whitehouse Scientific Ltd.
		22.81	± 0.78		
		25.60	± 0.72		
		28.41	± 0.94		
		31.33	± 0.82		

5.2.1.1 Fluorescent imaging of labeled microspheres

The goal of this experiment was to compare the spectra of different types of spheres that are similar in size. 15 μm diameter fluorescent labeled polystyrene spheres (Part No. 130-0485, Triton Technology Inc.) together with unlabeled PMMA spheres were submerged in an injectable phosphate buffered saline (PBS) solution in a microfuidic cavity. Fluorescent labeling was used to differentiate the spheres as an aid in effectively comparing their optical images. The recommended excitation and emission bands for this type of microspheres were 450 nm and 485 nm respectively. A blue LED with a center wavelength of 440 nm was used to excite the fluorescence. The experimental setup for fluorescent imaging was similar to that shown in Figure 5.2 except a 450 nm low pass filter (FES0450, Thorlabs Inc.) and a 475 nm long pass filter (475FG03-25, Andover Corporation) were inserted in front of the LED and the CMOS camera respectively to improve the image contrast by filtering out the LED excitation light collected by the camera. Figure 5.4 shows the fluorescent image taken by a Lucam CCD

camera that has integration time adjusting function. With the help of fluorescent imaging, different types of microspheres can be successfully differentiated from their optical images. Detailed information about fluorescent imaging techniques could be found from www.cyto.purdue.edu. Similar experimental setup could be used to differentiate monocytes from lymphocytes in canine peripheral blood mononuclear cells (PBMCs) that will be used in this dissertation by labeling one type of cells with suitable fluorescent dye.

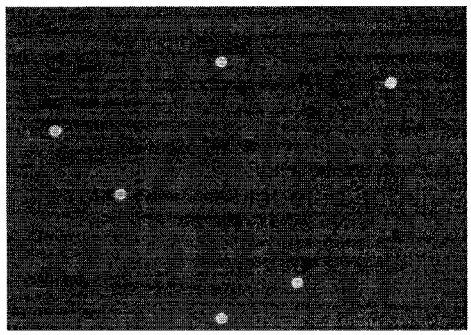

Figure 5.4 Optical image of 15 μm diameter polystyrene microspheres, where the highlighted spheres are fluorescent labeled and the dark spheres are unlabeled.

5.2.1.2 Titled excitation and mode matching

In order to differentiate between high order and fundamental modes, the transmission spectra excited at various excitation angles were taken and compared. Figure 5.5 shows that experimental setup and spectra taken from a 5μm diameter polystyrene sphere with a tilted excitation together with the theoretical fitting to the mode shifts as function of LED tilt angle.

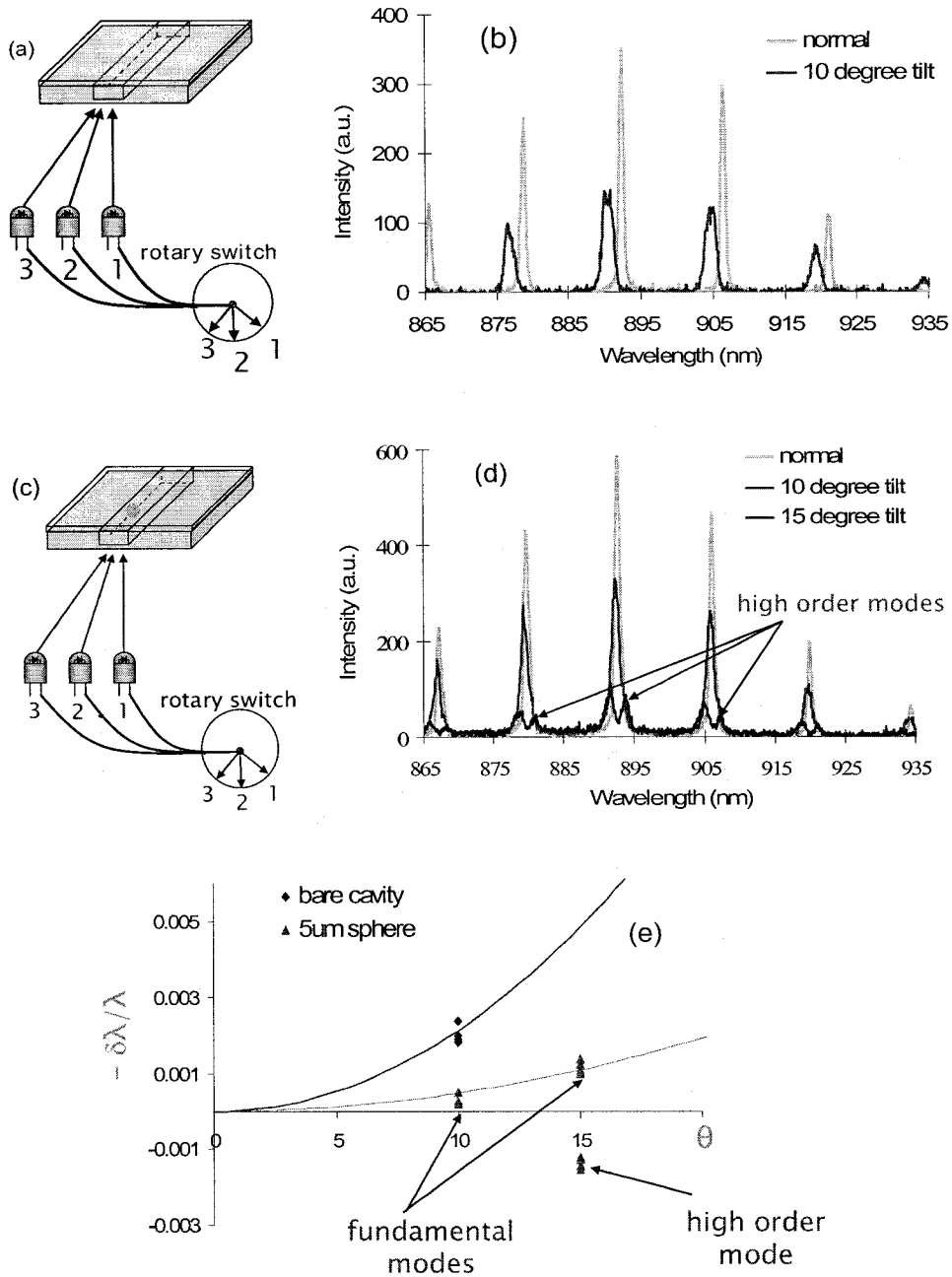

Figure 5.5 (a) schematic diagram of the LED illumination scheme, (b) bare fluidic cavity transmissions spectra under normal and tilted excitations, (c) illumination scheme and cavity configuration, (c) transmission spectra of a 5 μm diameter polystyrene sphere loaded cavity under normal and tilted illuminations, and (e) theoretical modeling of mode shift vs. excitation tilt angle.

Figure 5.5 (d) indicated that high order transverse modes of the sphere loaded cavity were at the long wavelength side and were effectively excited by the titled illumination due to their relatively larger diffraction angles than the fundamental modes. This result agrees with the normal mode assignment conventions of optical waveguides. However, the transverse mode order can not be obtained from the above spectra. It was found that transverse modes corresponding to a specific longitudinal mode were hopped to the longer wavelength side by more than one free spectral range (FSR) due to the large refractive index contrast between the sphere and the surrounding fluid. Detailed information on mode hopping vs. sphere size and refractive index will be presented in Section 6.3.6.

Results shown in Figure 5.5 may provide general insight into the effects of tilted illumination on the cavity transmission spectra since the current optical apparatus were only able to measure the illumination angles roughly. Future work should be done in terms of designing optical system capable of measuring the illumination angle with certain accuracy. In the case of real biological cells, situation is more complicated because of the unknown refractive index, absorption, and nonuniformity of cell geometry. Transmission spectra of real cells are presented in the following sections.

5.2.2 Spectra of yeast cells and human blood cells

The first biological cell type investigated was yeast cells because of their ready availability and size (8 to 15 μm diameter) compatibility with the optofluidic cavity. Transmission spectra for three separate single yeast cells prepared in water together with the mode excitation conditions are shown in Figure 5.6 and appear relatively similar.

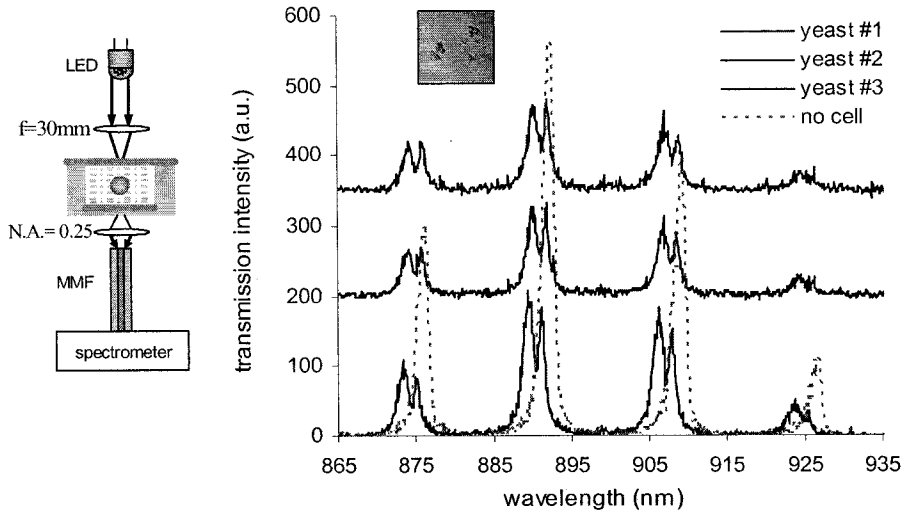

Figure 5.6 Transmission spectra of three separate single yeast cells. The bare cavity mode spectrum is also shown with the dashed line. The inserted image of the yeast cells was taken by a dark field microscope.

Bare cavity spectrum observed in regions away from the yeast cells is also shown with a dashed line. A shift in wavelength is anticipated between the bare cavity mode and even the fundamental optical mode in the presence of a cell both because of a variation in the transverse optical confinement as well as the integrated optical path length changing due to the cell's higher index of refraction compared to the water. Bare cavity regions or specific cells can be interrogated by simply horizontally translating the optical fiber to accept the image of that region. The relative fiber position can be determined by backward illuminating the fiber and observing the light spot relative to the cell positions in the microscope.

Microfluidic FP cavity transmission spectra for several blood cells were also obtained. The cells were obtained from a single human and introduced into the microfluidic cavity without any dilution of the original blood serum. Two distinct types of spectra were obtained corresponding to red blood cells seen in Figure 5.7 (a) and what

are believed to be various types of white blood cells seen in Figure 5.7 (b).

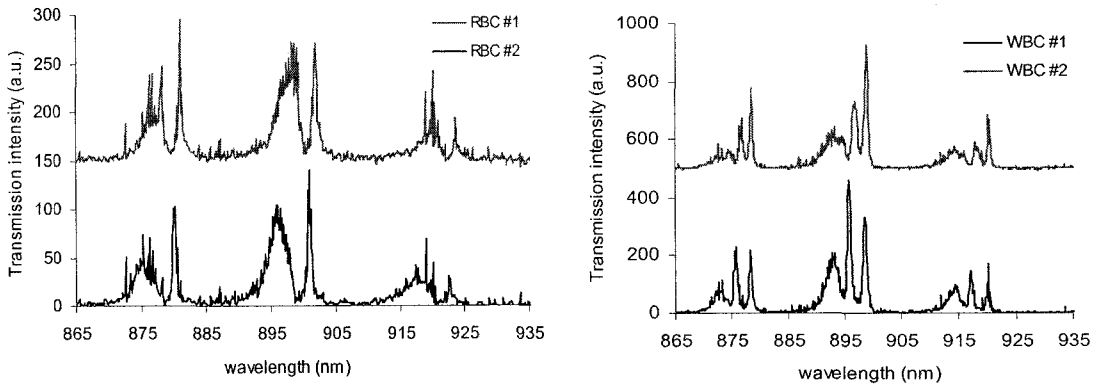

(a) (b)

Figure 5.8 Transmission spectra of (a) red and (b) white human blood cells. The mode excitation condition is the same as shown in Figure 5.6.

The spectral signatures of the different cell types are considered to be sufficiently qualitatively unique to differentiate them. The yeast cells showed a single, relatively broad transmission peak at slightly longer wavelength than what is assumed to be the fundamental mode. The blood cells showed strong, narrow transmission peaks, one for red blood cells and two for white blood cells, at larger wavelength offsets. The amount of offset varies somewhat from cell to cell and may be associated with cell size.

The experimental spectra of single biological cells presented above qualitatively appear to have characteristics such as the number of modes and mode spacing that can be used to differentiate cells. To further evaluate the utility of this sensor, a method for quantitative calculation of the spectral correlation was developed and evaluated as discussed in the next section.

In order to prove the repeatability and reliability of the biosensor to differentiate single biological cells, transmission spectra of multiple cells of each type used in this work have been taken repeatedly. While the spectra corresponding to a particular cell type are qualitatively considered to be repeatable, it is useful to quantitatively assess the similarities of the spectra. Correlation analysis is a widely used technique in biochemical experiments to recognize specific chemical components [1, 2] and will be applied here to cell differentiation.

The spectral data were prepared for correlation computations using the following steps. (1) A portion of each spectrum corresponding to a single free spectral range of the cavity was selected. Typically this was the central, highest intensity portion of the spectra. (2) The bare cavity mode peak, taken to be the broad, lowest wavelength peak, was assigned a relative wavelength offset of 0 nm. (3) The wavelength offset range was normalized to place the dominate peak of each spectra at the same point. (4) A Lorentzian lineshape curve was fit to the bare cavity mode and subtracted from the spectrum thus removing the bare cavity mode which was taken to contain no cell specific information. (5) Lastly, the root-mean-square amplitude of the net spectrum containing the transverse mode transmission peaks was normalized to unity. The resulting spectra for one red blood cell and one white blood cell are shown in Figure 5.9 as examples.

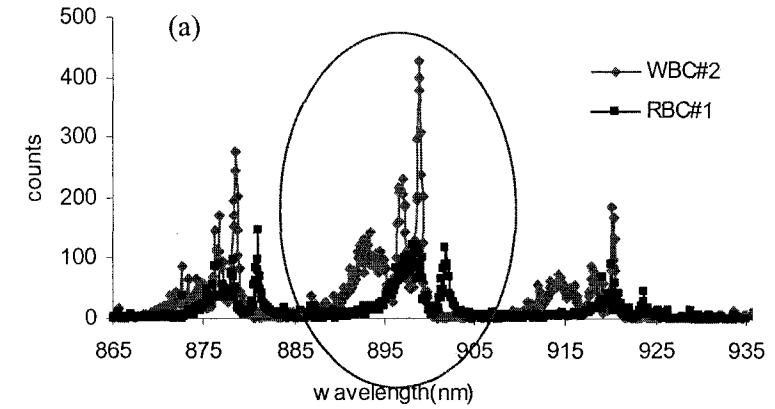

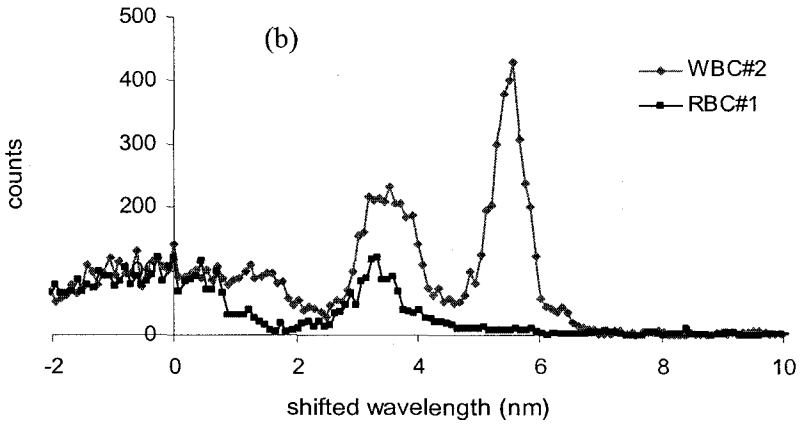

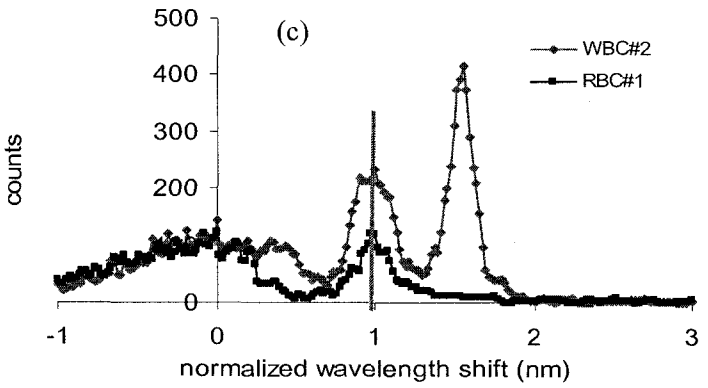

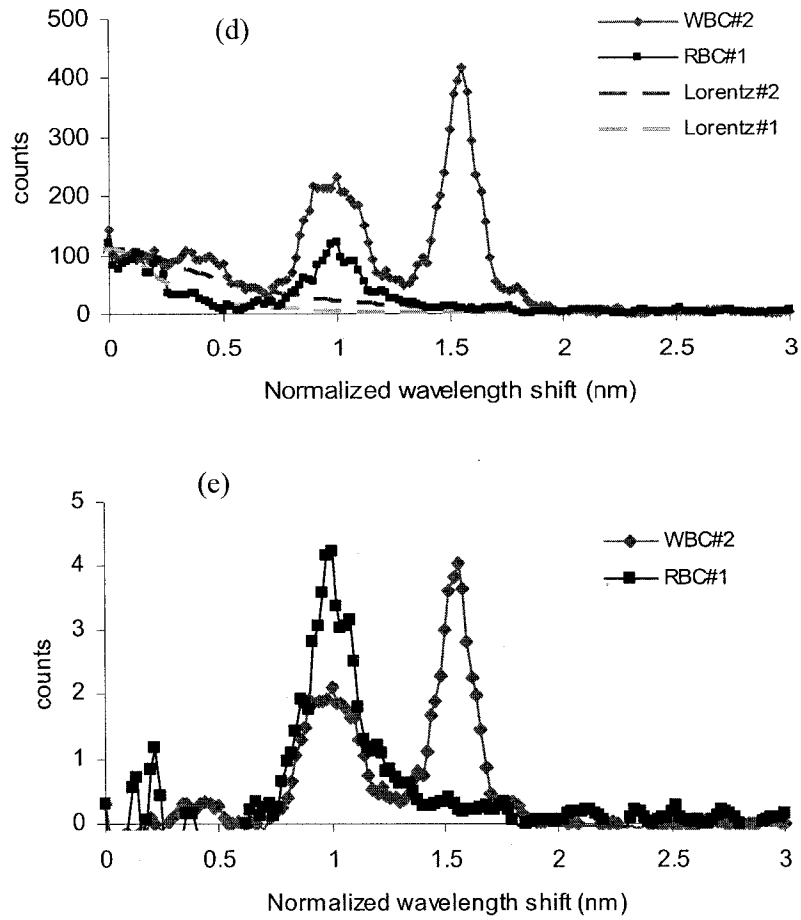

Figure 5.9 Spectra of a red blood cell and a white blood cell processed according to the steps discussed in the text and ready for a correlation integral.

The correlation coefficients between the transmission spectra of four red blood cells, two white blood cells, and three yeast cells were then computed and recorded in Table 5.2. The correlation data shows that the red blood cells can be differentiated from the other blood cells based on a correlation coefficient threshold of 0.8, but that the method is not sufficient to differentiate red blood cells from yeast cells. It is also noteworthy that the two white blood cell spectra had a relatively low correlation and may have come from different cell types e.g. neurophils and lymphocytes. The results presented here were

initial correlation studies and better results are expected from more complete studies including the creation of correlation templates or masks that account for the variability of spectra for the same type of cells.

Table 5.2 Correlation coefficient of spectra for red blood (RBC), white blood (WBC), and yeast (Y) cells.

	RBC1	RBC2	RBC3	RBC4	WBC1	WBC2	Y1	Y2	Y3
RBC1	1	0.8400	0.8400	0.8721	0.7016	0.6716	0.8430	0.862	0.7993
RBC2	0.84	1	0.9011	0.847	0.757	0.7442	0.820	0.8115	0.8666
RBC3	0.8721	0.9011	1	0.8784	0.7026	0.7241	0.6810	0.7660	0.7314
RBC4	0.9252	0.8470	0.8784	1	0.7591	0.7223	0.9068	0.9230	0.8907
WBC1	0.7016	0.7570	0.7026	0.7591	1	0.6507	0.6910	0.7690	0.7533
WBC2	0.6716	0.7442	0.7241	0.7223	0.6507	1	0.571	0.6385	0.7465
Y1	0.843	0.820	0.6810	0.9068	0.6910	0.571	1	0.9699	0.8707
Y2	0.862	0.8115	0.7660	0.9230	0.7690	0.6385	0.9699	1	0.9247
Y3	0.7993	0.8666	0.7314	0.8907	0.7533	0.7465	0.8707	0.9247	1

5.2.3 Differentiation of cancerous and normal cells

The RI of the phosphate buffered saline (PBS) solution is critical for accurate modeling wavelength shift induced by the cells. In order to measure the RI of the PBS solution (phosphate 50mM, NaCl 0.9%), transmission spectra of an optofluidic cavity filled with DI water and PBS solution were taken at the same cavity location respectively. An HfO_2/SiO_2 dielectric coated cavity bonded with AZ4400 photoresist and sealed with silicone caulk was used in this experiment. First, DI water was delivered into the channel by a syringe through the nanoport assembly. Transmission spectrum was taken by the HR2000 spectrometer immediately after the channel was fully filled with water and the position of the light collection spot was recorded by a CCD camera. Then the other syringe containing PBS solution was utilized to inject PBS solution into the microfluidic channel and push DI water out of the channel. The transmission spectrum

was then taken at the same position within the microfluidic cavity as shown in Figure 5.10. The RI of the PBS can be calculated from $n_0 = n_1 (\lambda_0 / \lambda_1)$ by measuring the m_{th} longitudinal mode shift of a FP cavity filled with DI water and the PBS, which is 1.333 and 1.366 without and with mode hop respectively. Therefore, a cavity length of ~15.8μm was measured after thermal bonding using $L_{cav} = \lambda^2/(2n_0\Delta\lambda)$, where n_0 was taken to be 1.333 to be consistent with other reports [4, 5].

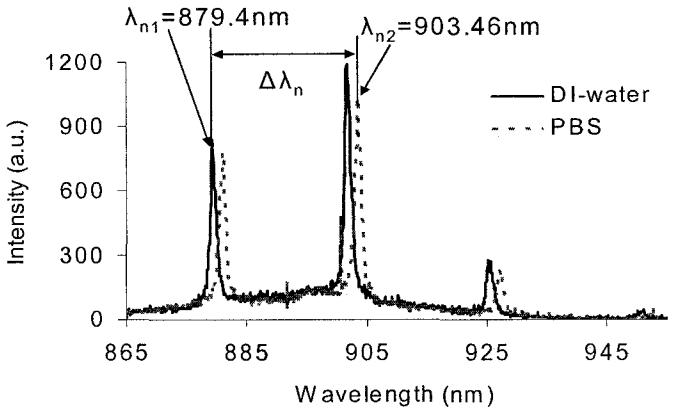

Figure 5.10 Transmission spectra of a DI water-filled and PBS-filled optofluidic cavity.

Transmission spectra of single cells from two canine lymphoma cell lines as well as baseline non-cancerous lymphocytes centrifuged from peripheral blood mononuclear cells (PBMCs) were collected. An example spectrum of lymphoma is shown in Figure 5.11 (a) together with bare cavity spectra taken at four different positions adjacent to the cell. Alignment of the four bare cavity spectra demonstrates the good cavity uniformity in the neighborhood of each cell although the bare cavity resonant wavelength does vary along the length of the channel. Transverse mode groups are repeated for each longitudinal mode and are spaced by the cavity's free spectral range (FSR) of ~20 nm.

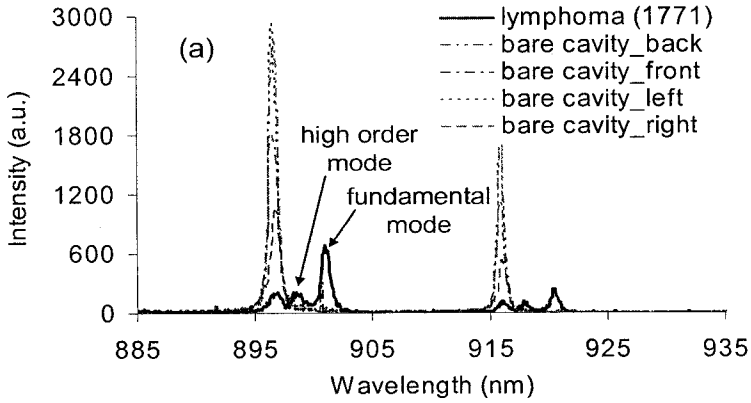

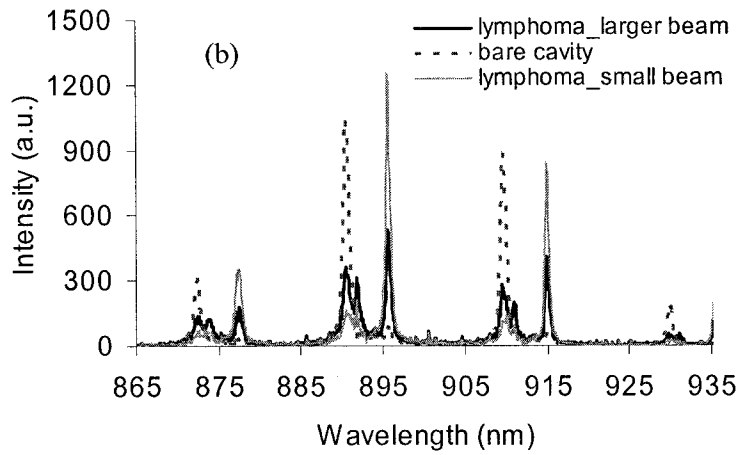

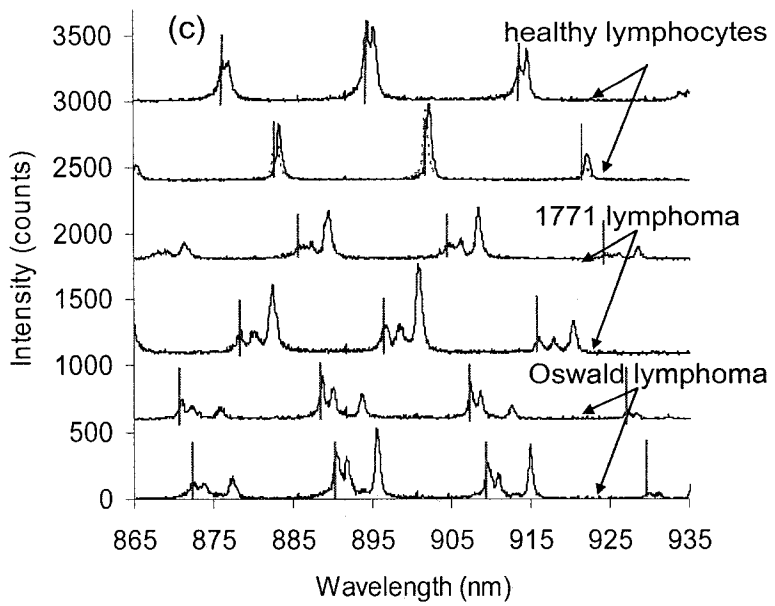

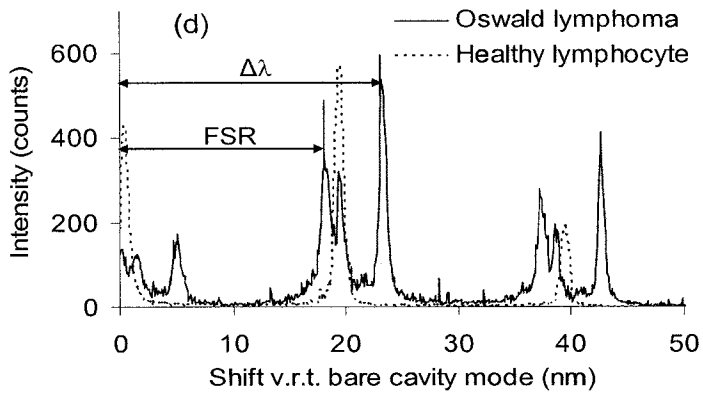

Figure 5.10 Transmission spectra of (a) 1771 canine lymphoma together with bare cavity spectra taken near the cell, (b) spectra of Oswald lymphoma collected over different areas, (c) healthy canine lymphocytes and cancerous lymphoma cells from two different cell lines, Oswald and 1771, where vertical lines denote the bare cavity modes adjacent to each cell, and (d) transverse mode shift for an individual lymphocyte from canine PBMCs and lymphoma.

Figure 5.10 (a) clearly shows that the peaks near 896 and 916 nm in the lymphoma spectrum correspond to residual transmission through the bare cavity around the cell. The other two modes in each transverse mode group, for example at 899 and 901 nm, are due to a combination of longitudinal mode shift and lateral confinement by the cell and will be discussed in detail in Chapter 6.

The longer and shorter peaks associated with the cell are respectively dominated by the nucleus and cytoplasm. Varying the light collection spot size changes the intensity of the longer wavelength nuclear mode relative to the fundamental mode as shown in Figure 5.10 (b). A small collecting beam increases the intensity of the nuclear mode supporting its assignment to the nucleus. The spectroscopic experiments were repeated on different types of single cells. Figure 5.10 (c) and (d) shows the spectra of individual lymphoma from two cell lines, labeled as "Oswald" and "1771" as well as a non-cancerous

lymphocyte for reference. The number of modes and spectral mode spacing for both the lymphocytes and the lymphoma cell lines were very repeatable for the same type of cell except that the absolute wavelength of each mode shifts due to slight variations in the cavity length at different locations.

In order to determine effective RIs for each cell mode relative to the bare cavity, an ambiguity in the absolute mode shift needs to be resolved. For example, lymphocytes exhibited only a single mode red shifted from the bare cavity by $\Delta\lambda = j\text{FSR} + 0.49 \pm 0.30$ nm where FSR=19.69 nm. The corresponding refractive index is $n_{lymphocyte}$=1.3345, 1.3733, and 1.4105 for values of j = 0, 1, and 2, respectively. Previously published results indicate that the correct value for lymphocytes is 1.3550 [5] to 1.4126 [4] so that j = 1 in this case. Thus, while the spectrum in Figure 5.10 (d) may appear to indicate only a very small $\Delta\lambda$=0.49 nm, reasonable lymphocyte refractive index values require that lymphocytes shift the resonant wavelength from that of the bare cavity by $\Delta\lambda$=20.18 nm or slightly more than one FSR.

The Oswald lymphoma cell line displayed a whole cell mode shift of 20.36 ± 0.40 nm corresponding to an effective index of 1.3737 ± 0.0008, and a nuclear mode shift of 24.59 ± 0.13 nm corresponding to an effective index of 1.3817 ± 0.0002. Modeling of the cells allows the measured mode effective indices to be used to extract material effective indices for the cell cytoplasm and nucleus.

5.3 Summary

This chapter presented the transmission spectra for optofluidic Fabry-Pérot cavities containing polystyrene spheres, yeast cells, and human blood cells, and canine lymphoma

and PBMCs. The transmission spectra for the cell types were qualitatively different in terms of the number, relative position, and relative wavelength offset of transverse modes. Preliminary quantitative correlation analysis of the spectra demonstrated the capability of the biosensor to differentiate certain pairs of single biological cells. Thus the approach utilized in this project may provide a useful label-free optical technique for recognizing cells in a microfluidic environment.

References

[1] E. Gratton, S. Breusegem, N. Barry, Q. Ruan, and J. Eid, "Fluctuation correlation spectroscopy in cells: Determination of molecular aggregation", *Biophotonics-Optical Science and Engineering for the 21st Century*, Norwell, MA: Kluwer, 2004.

[2] P. Schwille, F. J. MeyerAlmes, and R. Rigler, "Dual-color fluorescence cross-correlation spectroscopy for multicomponent diffusional analysis in solution," *Biophys J.*, vol. 72, no. 4, pp. 1878–1886, Apr. 1997.

[3] T. Akimoto, S. Sasaki, K. Lkebukuro, and 1. Karube, "Refractive-index and thickness sensitivity in surface plasmon resonance spectroscopy", *Applied Optics*, vol. 38, no. 19, 1999.

[4] A. N. Shvalov, I. V. Surovtsev, A. V. Chernyshev, J. T. Soini, and V. P. Maltsev, "Particle classification from light scattering with the scanning flow cytometer", *Cytometry*, vol.37, no. 3, 1999.

[5] K. W. Keohane and W. K. Metcalf, "The cytoplasmic refractive index of lymphocytes, its significance and its changes during active immunization", *Q J. Exp Physiol Cogn Med Sci.*, vol. 44, pp. 343, 1959.

Chapter 6

Optical Modeling

For cells in a microcavity, the small-angle forward scattered light is reflected back through the cell, while the large angle scattered light is lost sideways from the longitudinal cavity. The reflected light cycles through the cell and fluidic cavity until a stable mode pattern is formed. The experimental results presented in Chapter 5 have shown that intracavity spectra of different types of cells exhibit variations in mode intensity, mode spacing, and number of high order transverse modes, which provide specific spectral signatures for different types of cells. All of these spectral differences are attributed to the optical confinement induced by the cells since cells inside a passive microcavity serve as optical waveguides to confine light injected from the external LED. The waveguiding effect is induced by the slight difference in the dielectric constants between various cell components and the surrounding fluids. Theoretical interpretation of intracavity spectra provides insight into specific modal structures for classifying individual cells. This chapter focuses on modeling the transmission spectra of sphere-loaded and cell-loaded plane-plane Fabry-Pérot (FP) cavities and compares the modeling results with the experimental data presented in the previous chapter. Extensive numerical modeling has been done and is presented in the following sections in the sequence of increasing accuracy and increasing computation time. Section 6.1 presents the simulation results using the paraxial Gaussian beam propagation method (BPM). Section 6.2 discusses the effective refractive index method and its application in modeling optofluidic FP cavities. A comparison between the modeling and the measured spectra of

sphere-load cavities will be presented afterwards. The effective index model will also be used to derive the cellular refractive indices of canine lymphocytes and lymphoma cells from the measured cell spectra. Section 6.3 discusses the full numerical simulation results using the 3-dimensional finite-difference time-domain (FDTD) method. Section 6.4 compares the modeling results and the experimental ones. Finally, the accuracy and applicability of each model's results will be discussed and compared in Section 6.5.

6.1 Analytical solutions by Gourley

Analytical solutions for optical modes of a sphere loaded passive microcavity were reported by Gourley et al [1]. They studied optical modes of three cavity configurations, (a) no cell, (b) flat cell, and (c) fully three-dimensional objects in the cavity as shown in Figure 6.1. The following sub-sections briefly review their results for reference.

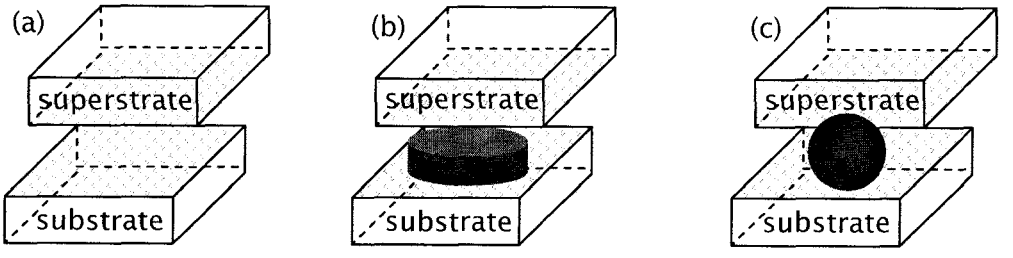

Figure 6.1 Cavity configurations for (a) 1-D, (b) 2-D, and (c) 3-D cases.

6.1.1 One-dimensional case

When no cell is present, the cavity length L_{cav} and the dielectric constant of the fluid in the cavity will establish the cavity resonance frequencies. The q_{th} order longitudinal mode wavelength is $\lambda_q = \frac{2\sum_i d_i n_i}{q - \phi/2\pi}$, where $2\sum_i d_i n_i$ is the round trip optical path length

in the cavity comprising a sum of lengths d_i of index n_i and ϕ is the sum of mirror phases.

6.1.2 Two-dimensional case

The second case is for flat cells like red blood cells that resemble two-dimensional objects. To first order, a cell in the cavity can be modeled by a disc of index n_{cell} surrounded by a fluid of index n_{cav} as shown in Figure 6.1 (b). This problem is similar to the solution of optical modes in a dielectric waveguide. In this case, the cell will perturb each bare-fluid mode given by the 1-D analytical solution by adding a series of modes at longer wavelengths λ_{qmv}, where q, m, v index the longitudinal, radial, and angular solutions to the wave equation for light confined by the cell in the cavity. The fundamental transverse mode has the longest wavelength separation from the bare cavity mode λ_l of the cavity and is given to good approximation by $\Delta\lambda_{qmv} = \Delta\lambda_q \frac{-\lambda_q^3 \chi_{00}^2}{2\pi^2 n_{cell}^2 (2R)^2}$, where R is the cell radius, χ_{00} is the 00^{th} zero of the 0^{th} order Hankel function, and the first factor arises from the dielectric shift $\Delta\lambda_q = \Delta\xi/(q - \phi/2\pi)$, where $\xi = 2\sum_i d_i \Delta n_i$ due to the change in index from the fluid (e.g. cytoplasm) to that of the cell, and the second factor, $\frac{-\lambda_q^3 \chi_{00}^2}{2\pi^2 n_{cell}^2 (2R)^2}$, arises from the lateral confinement of light by the cell. The solutions for the fundamental and higher order transverse modes are solutions to the wave equation and are given by the characteristic equations $\frac{XJ_{m\pm1}(X)}{J_m(X)} = \frac{\pm YK_{m\pm1}(Y)}{K_m(Y)}$ and $X^2 + Y^2 = V^2$, where J and K are Bessel and modified Bessel functions, respectively, and $X = ka$ and $Y = \gamma a$ are wave vector parameters of the cell and surrounding regions,

respectively. The normalized frequency V is defined as $V = (2\pi R / \lambda_1)\left(n_{cell}^2 - n_{cav}^2\right)^{1/2}$, where R is the cell radius and the latter factor is the numerical aperture of the cell. The resonant mode wavelength is $\lambda_{qmv} = \frac{2\pi n_{cav}}{\left[(X_{mv}/R)^2 + (q\pi / L^*_{cav})^2\right]^{1/2}}$, where X_{mv} is the v^{th} root of the characteristic equation and L^*_{cav} is an effective cavity length. The set of roots includes the fundamental mode and shorter wavelength modes.

6.1.3 Three-dimensional case

The three-dimensional case shown in Figure 6.1 (c) was approximated by a spherical cell between two reflecting planes, which was complicated due to the dissimilar geometries of the cell and the longitudinal cavity. The problem was simplified by making the adiabatic approximation that the longitudinal field variation was rapid compared to the lateral field variation. For spherical objects placed within the FP cavity, the authors expected the optical modes to be solutions to the Helmholtz equation and contain symmetries of both the longitudinal cavity and the sphere. An approximate solution is $\psi = f(z)g(r,\theta,\varphi)$, where f is the one-dimensional solution for the rapid varying field along the cavity length and g is the slowly varying solution for spherical waves. The functions f and g are solutions to $(\nabla^2 + K^2)f(z) = 0$ and $(\nabla^2 + k^2)g(r,\theta,\phi) = 0$ respectively. The traveling wave solutions are of the form $f = ae^{\pm iKz}$ and $g = h_l^{(1,2)}(kr)Y_l^m(\theta,\phi)$. The $h_l^{(1,2)}(kr)$ are spherical Hankel functions and $Y_l^m(\theta,\phi)$ are spherical harmonics. These solutions represent waves traveling in the $\pm z$ and $\pm r$ directions, respectively. The wave equation for the product solution is $g\delta^2 f + f\delta^2 g + 2\delta f \cong \delta g + \frac{\omega^2 n^2}{c^2 fg} = 0$. This equation can

be approximated by $K^2 + k^2 + 2Kk\xi = \frac{\omega^2 n^2}{c^2}$, where ξ is a geometrical factor averaged over the spherical volume. Since $K >> k$, the wavelength can be approximated as $\lambda_{l_n} = \frac{2n_s L_{cav}}{q} - \frac{4\xi n_s x_{ln} L_{cav}^2}{\pi q^2 (2R)}$, where n_s is the index of the sphere, L_{cav} is the effective cavity length, q is the longitudinal mode index, x_{ln} is the n_{th} zero of the l_{th} Hankel function, and d is the sphere diameter. The analytical solution is valid when the index difference between the sphere and the surrounding fluid is sufficiently large. However, as mentioned in page R234 of [1] the cell or nucleus refractive index is only slightly larger than its surrounding media, which makes the above numerical solutions not suitable for real cells. Also an unknown parameter, ξ, in the analytical solution needs to be determined by fitting the experimental data in order to model microspheres with large refractive indices as discussed in the other paper [2] coauthored by P. L. Gourley. Therefore, further exploration of practical optical models for sphere or biological cell loaded FP cavity transmission spectra is desirable in order to interpret the intracavity spectra.

6.2 Paraxial Gaussian beam propagation method

Classical paraxial Gaussian beam resonator analysis expressed in *ABCD* matrices allows setting bounds on parameters for resonator stability and provides guidance on the cavity design. In order to couple the maximum amount of the transmitted light from an optofluidic cavity, it should be designed to function within the stable range to minimize diffraction loss. Under the stable operation condition, beam profile matching between the excitation LED and the stable cavity modes allows efficient excitation of transverse

modes. Section 6.2.1 presents resonator stability analysis using ABCD matrices. The paraxial approximation is known to be accurate if the beam waist is much bigger than the wavelength [3]. Transverse mode profiles calculated using the ABCD matrices will be presented in Section 6.2.2. And Section 6.2.3 will show the transverse mode spacing calculated from the Guoy phase shift.

Since exact mathematical models for biological cells are unavailable, initial simulations are performed on a plane-plane FP cavity containing a single microsphere with uniform refractive index submerged in water as shown in Figure 6.2.

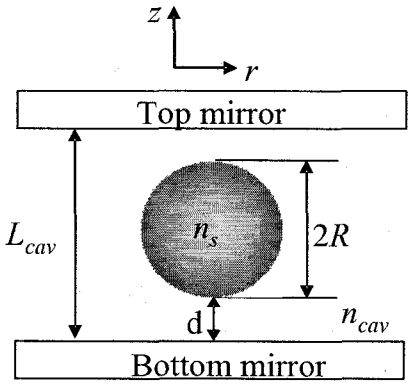

Figure 6.2 Schematic diagram of a high refractive index microsphere in a plane-plane resonator cavity. n_s is the refractive index of the microsphere, n_{cav} is the refractive index of the microfluidic cavity, and d is the distance of the outside of the sphere from the bottom planar mirror, and L_{cav} is the cavity length.

6.2.1 Cavity stability analysis

The stability of an optical resonator can be determined by the magnitude of the trace of the round trip ABCD matrix within the paraxial approximation [4]. For simplicity, the cavity described in this section is based on a single polystyrene sphere with a uniform refractive index of 1.59 submerged in a plane-plane FP resonator filled with water of

index 1.33. The microsphere is free to move within the cavity, and the sphere position alters the resonant modes of the cavity. The round trip ABCD matrix of a plane-plane FP cavity containing a microsphere is represented as $M_{RT} = M_{OW1} \cdot M_{OW2}$, where M_{OW1} and M_{OW2} represents the one-way (OW) matrix for going from one mirror to the other mirror. Treating the microsphere as a thick ball lens, $M_{OW1} = \begin{bmatrix} 1 & \frac{(1-\rho)(L_{cav}-2R)}{n_{cav}} \\ 0 & 1 \end{bmatrix} \begin{bmatrix} \frac{2n_{cav}-n_s}{n_s} & \frac{2Rn_{cav}}{n_s} \\ \frac{2(n_{cav}-n_s)n_{cav}}{Rn_s} & \frac{2n_{cav}-n_s}{n_s} \end{bmatrix} \begin{bmatrix} 1 & \frac{\rho(L_{cav}-2R)}{n_{cav}} \\ 0 & 1 \end{bmatrix}$, where the parameter $\rho = d/(L_{cav}-2R)$ is defined as a normalized fractional distance of the sphere from the first mirror to the vertex of the sphere, d. L_{cav} is the cavity length, R is the sphere radius, n_{cav}=1.33 and n_s=1.59 are the refractive indices of the fluid cavity and the microsphere respectively. Similarly, the one-way ABCD matrix from the second mirror to the first mirror can be calculated as $M_{OW2} = \begin{bmatrix} 1 & \frac{\rho(L_{cav}-2R)}{n_{cav}} \\ 0 & 1 \end{bmatrix} \begin{bmatrix} \frac{2n_{cav}-n_s}{n_s} & \frac{2Rn_{cav}}{n_s} \\ \frac{2(n_{cav}-n_s)n_{cav}}{Rn_s} & \frac{2n_c-n_s}{n_s} \end{bmatrix} \begin{bmatrix} 1 & \frac{(1-\rho)(L_{cav}-2R)}{n_{cav}} \\ 0 & 1 \end{bmatrix}$. The trace of the round trip ABCD matrix can be readily calculated as a function of the sphere refractive index and position. Numerical matrix computations show that short cavities can always be made stable for sphere positions throughout the cavity where the maximum cavity length for unconditional stability with respect to sphere position is a function of the sphere and cavity index. Based on numerical matrix computations, a stability phase diagram has been constructed for a polystyrene sphere loaded microfluidic cavity and is shown in Figure 6.3.

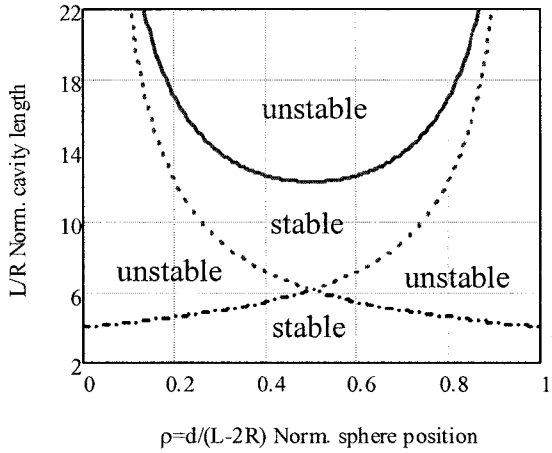

Figure 6.3 Stability diagram for a polystyrene microsphere (n_s=1.59) in a plane-plane resonator as a function of the normalized resonator configuration coordinate. The left side of horizontal axis corresponds to sphere at the bottom of the cavity and the right side corresponds to sphere close to the top planar mirror.

The above stability diagram shows the cavity length yielding a single point solution is approximately $L_{cav} = 6.05R$ for the refractive indices ($n_s = 1.59$) used here. Increasing the cavity length past this point starts again expanding the range of stable solutions until a cavity length of $L_{cav} = 12.3R$ gives a center point stability factor of $Tr(M_{RT}) = +1$, where $Tr(M_{RT})$ is the trace of the round trip ABCD matrix. Increasing the cavity length past this point will cause the center lens position to be unstable while some intermediate positions are stable, but the positions near the mirrors remain unstable. Increasing the cavity length to very large multiples of the radius then leaves only a decreasing, narrow range of stable lens separations near but not directly against the mirrors. Most importantly, for short cavities of length, $L_{cav} < 4R$, the cavity is stable for all microsphere positions. Therefore, the 10~20 μm deep cavities were used in this work to set the microfluidic unconditionally stable for ~10 μm diameter spheres.

6.2.2 Beam size calculation

Beam size calculations within sphere-loaded optofluidic cavities are needed to determine whether the paraxial approximation is appropriate. Movement of spheres within the microfluidic cavity changes the beam profile. For stable configurations, the beam size is finite while it becomes infinite for unstable configurations.

For the case of sphere centered in the cavity, the beam waist on both mirrors is identical and stability conditions for the round-trip are identical to the stability conditions for one-way propagation. The Gaussian beam waist, ω_0, is related to the round trip ABCD matrix through $\frac{1}{\tilde{q}} = \frac{D-A}{2B} - \frac{1}{B}\sqrt{\left(\frac{A+D}{2}\right)^2 - 1} = \frac{1}{R} - j\cdot\frac{\lambda}{\pi\omega_0^2}$, where λ is the wavelength of the light [A. E. Siegman]. Therefore, the size of the beam waist on the mirrors is given by $\sqrt{\frac{jB\lambda}{\pi n_{cav}\sqrt{[(A+D)/2]^2 - 1}}}$, where the fields fall off as at the beam waist on the mirrors. The size of the beam at the vertices of the sphere will be yet larger and may be computed from $\omega_{\max} = \omega_0\sqrt{1 + \left(\frac{z(\lambda / n_{cav})}{\pi\omega_0^2}\right)^2}$, where $z = \rho/(L_{cav} - 2R)$ for cases that the sphere is closer to the bottom mirror. Figure 6.4 shows the maximum beam radius as a function of the normalized sphere positions for 10 μm diameter polystyrene sphere-loaded cavities of different length.

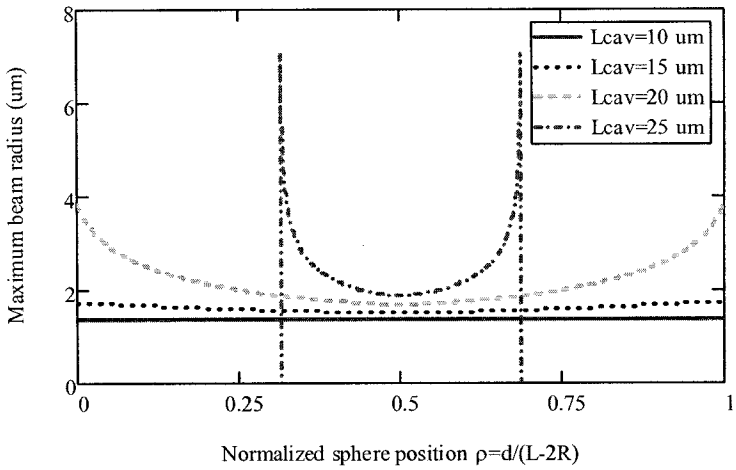

Figure 6.4 Maximum beam radius vs. the normalized sphere position for 10 μm diameter polystyrene sphere loaded cavities with different cavity depth.

In order to accurately model the sphere as a parabolic lens, the beam waist should also be significantly smaller than the sphere diameter. Symmetry consideration for a stable mode requires that beam waists occur at each flat mirror, thus making the phase curvature match the end mirror radius. For example, stability analysis in Figure 6.3 shows that the cavity is stable for all sphere positions when $L_{cav} < 4R$, which is 20 μm in this case. When the cavity length exceeds this limit, the maximum beam radius is larger than the sphere radius as shown in Figure 6.4 by the dash-doted curve corresponding to a cavity length of 25 μm. The relationship of the limit on L_{cav}/R vs. sphere refractive index shown in Figure 6.5 is also helpful to understand resonator stability range.

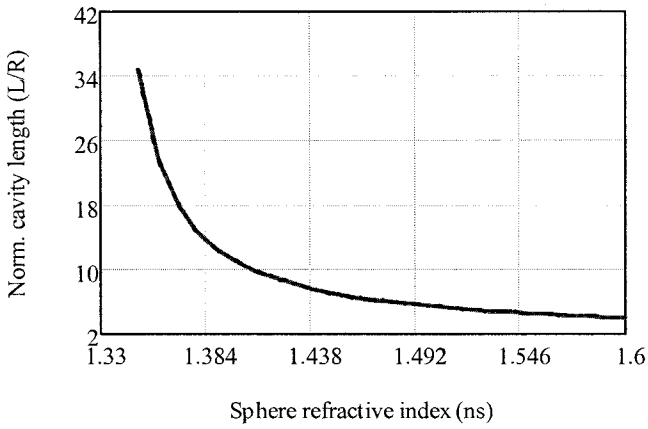

Figure 6.5 Limit on the normalized cavity length, L_{cav}/R, vs. sphere refractive index.

6.2.3 Transverse mode spacing from Guoy phase shift

It is well known that Laguerre-Gaussian or Hermite-Gaussian modes acquire a phase shift with respect to an on-axis plane wave if propagating along the optical axis [4]. This extra phase is usually called the Guoy phase shift, which has been shown to exist for any waves including acoustic waves that pass through a focus. A recent paper by researchers at University of Michigan shows explicitly that the well-known Guoy phase shift of any focused beam originates from transverse spatial confinement [5]. The Guoy phase describes a phase shift of the resonator wave solution which is purely determined by geometric optics and plays an important role in optics. For example, it determines the resonant frequencies of transverse modes in laser cavities, as presented in the following paragraphs.

Formally, the Guoy phase is the eigenphase of the round-trip ABCD matrix describing the stable ray orbit on which the paraxial cavity mode is built [6], and hence it measures the winding number of the off-axis rays corresponding to the transverse mode

profile. Therefore, transverse mode frequency spacing can be calculated from the amount of Guoy phase shift, ϕ_{Guoy} , acquired by the high order transverse modes as $\frac{c}{2[n_s 2R + n_{cav}(L_{cav} - 2R)]} \frac{\phi_{Guoy}}{\pi}$ [G. Machararian], where c is the speed of light, R is the radius of the sphere, and L_{cav} is the cavity length [4]. The Guoy phase shift of the nmth order transverse Laguerre-Gaussian mode of a sphere-loaded FP cavity can be calculated from $\phi_{Guoy} = -(n+m+1)\tan^{-1}(\frac{z}{z_R})$, where z_R is the Raleigh range and z is the distance from the beam waist. The other definition of Guoy phase shift is $\phi_{Guoy} = -(n+m+1)\cos^{-1}(\sqrt{g_1 g_2})$, where g_1 and g_2 are the resonator g parameters, which have explicit expressions for simple cavities with plane-plane, confocal, and convex configurations [4]. However, the calculation of Guoy phase shift of a sphere loaded plane-plane FP cavity using this formula is not straightforward. The Guoy phase can also be calculated from Φ_{Guoy} = -(n+m+1)arg $[(A+B/\tilde{q})^{-1}]$ [4], where A and B are the (0, 0) and the (0, 1) element of the round trip ABCD matrix respectively. Figure 6.5 shows the transverse mode spacing of a sphere-loaded plane-plane FP cavity with varying (a) cavity length, (b) sphere size, and (c) sphere refractive index as a function of the normalized sphere position ρ calculated using the third formula.

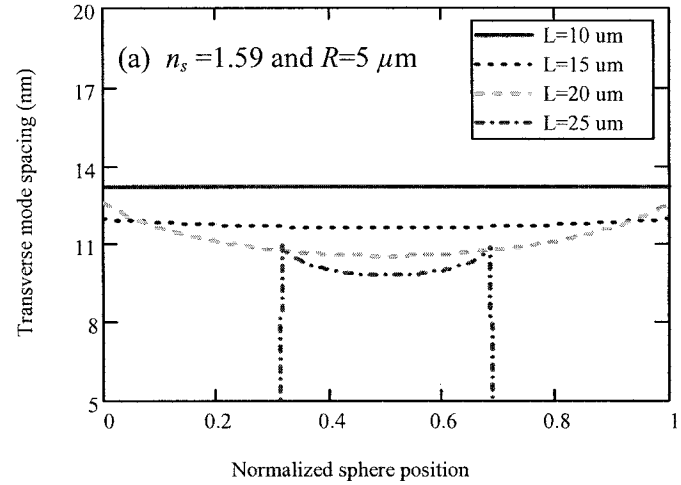

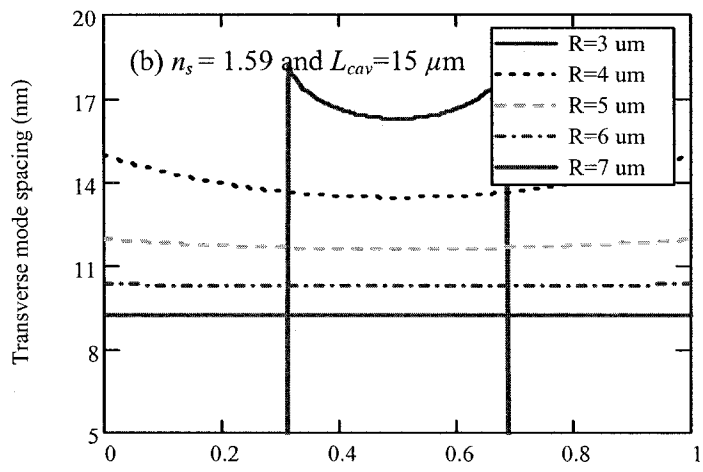

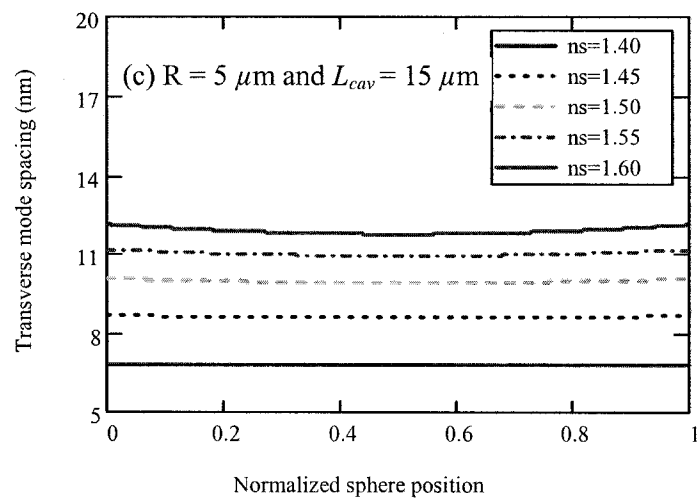

Figure 6.5 Transverse mode spacing calculated from the Guoy phase shift of microfluidic FP cavities with (a) different cavity length, (b) different sphere size, and (c) different sphere refractive index.

The above simulation results indicate that transverse mode spacing decreases with the increase in cavity length and sphere size, while the spacing increases as sphere refractive index increases. It also reveals that a small cavity length may decrease the variation of transverse mode spacing shift with the sphere position. Therefore, a short cavity is desired since it provides stable operations for all the possible sphere positions within the cavity and also minimizes the variation in the transverse mode spacing. The ability to detect high order transverse modes is also increased due to the greater transverse mode separation of a shorter cavity.

However, paraxial Gaussian analysis relies, by definition, on small angular spread in the local direction of wave front propagation. Limitations of the paraxial theory have long been recognized both in the context of macroscopic and microscopic high-finesse cavities when the relevant numerical aperture becomes sufficiently large. In non-paraxial resonator geometries, Gaussian beams become less suitable as a starting point, so that one retreats to more general approximation methods. Interested readers may refer to the reference paper [6] listed at the end of Chapter 6 for information on non-paraxial analysis of optical resonators.

6.3 Effective refractive index method

Wavelength shifts of high order transverse modes from the bare-fluid mode are related to the refractive indices and sizes of the objects in the cavity. The widely used

beam propagation method (BPM) has difficulty in modeling structures with large index differences in the beam propagation direction due to back reflections. This section presents an effective refractive index model for the optofluidic cavities followed by the introduction of a numerical mode solver for resonant modes.

6.3.1 Hadley's effective index model

The effective index method used in this work was based on the effective refractive index model developed by Hadley for explaining the waveguiding effects in vertical cavity surface emitting lasers (VCSELs) fabricated by selective oxidation [7]. The basic concept of his model is that the effective index responsible for waveguiding is dependent only on lateral changes in the FP resonance frequency. The mathematical representation is $\frac{\Delta n_{eff}}{n_{eff}} \approx \frac{\Delta \lambda_0}{\lambda_0}$, where n_{eff} is the effective index and λ_0 is the resonant wavelength. The two important implications conveyed by the model are (1) VCSEL's effective index profile is determined by local changes in the FP resonance frequency and (2) its variation within the cavity can be of either sign, depending on the direction of shift of the resonance. Similar concepts can be applied to the sphere/cell loaded FP cavities for calculating the effective index profile from the local resonant wavelength shift.

6.3.2 Effective index profile of sphere-loaded cavities

Placing a three dimensional object inside a plane-plane FP cavity shifts the resonance frequency of the cavity in that region. The cells and spheres within a microcavity serve as optical waveguides to confine light injected from the external LED. According to

Hadley's optical model, the effective index of such cavity is determined by the local changes in the FP resonance frequencies. The variations in the effective indices depend on the direction of frequency shift according to $\Delta n_{eff}/n_{eff} \approx \Delta\lambda_0/\lambda_0$, where n_{eff} and λ_0 are the effective refractive index and the resonance wavelength of the cavity with and without the 3D object, and Δn_{eff} and $\Delta\lambda_0$ are the changes of these two parameters due to the microsphere respectively. Figure 6.6 shows the calculated effective refractive index profile of different spheres in a 16 μm deep microfluidic cavity coated with hard mirrors.

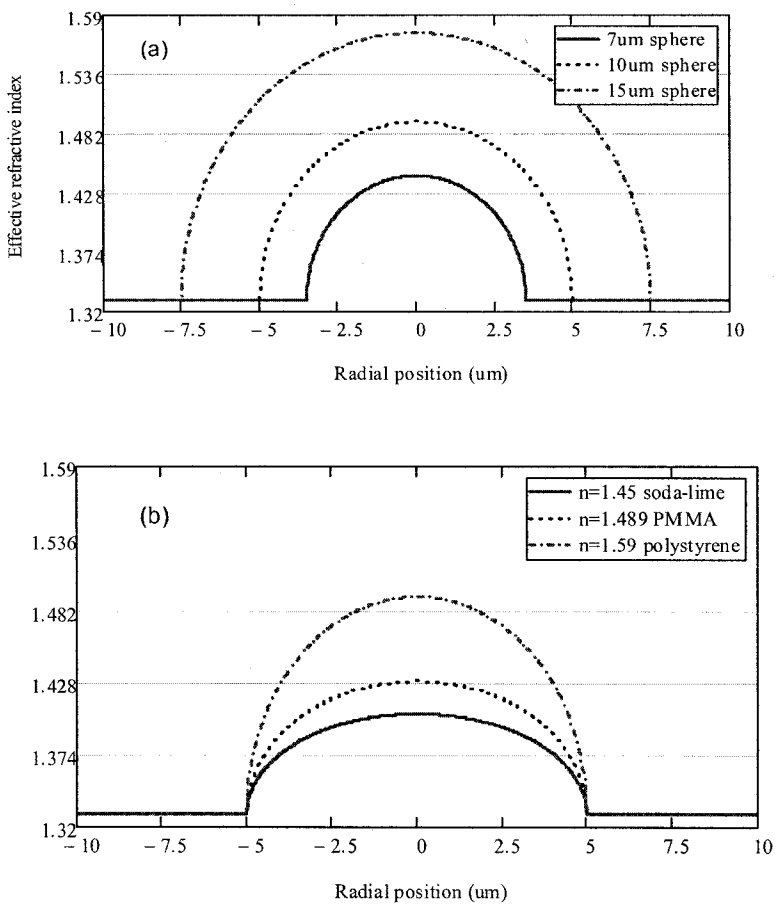

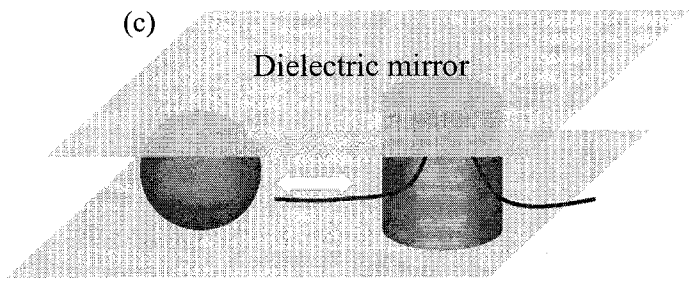

Figure 6.6 Effective refractive index profile of a 16 μm deep microfluidic FP cavity containing (a) n_s =1.59 microspheres of different size; (b) 10 μm diameter spheres with different refractive indices; (c) Equivalence of a sphere-loaded microfluididic cavity to a GRIN fiber loaded cavity.

6.3.3 Double sphere model for cells

The absence of exact mathematical models for real biological cells motivates the development of simplified cell models. A concentric double homogeneous refractive index sphere model, widely used in scattering spectroscopy [8, 9] and illustrated in Figure 6.7 (a), was employed in this work in order to quantitatively analyze the spectra and extract RI information of the cells. Figure 6.7 (b) shows the effective RI profile of a double sphere loaded cavity in cylindrical coordinates obtained using an effective index model where the radial dependence of the refractive index was calculated from the cavity's resonant wavelength using the refractive index distribution at each radius. Detailed calculation procedures are provided in Appendix D.

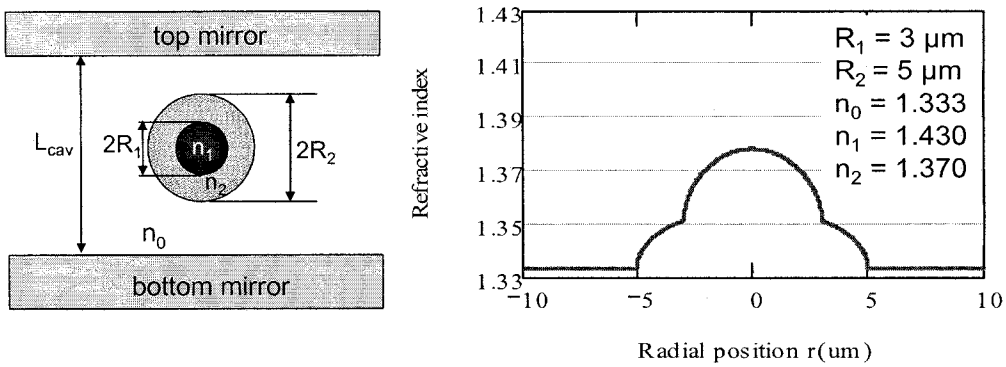

(a) (b)

Figure 6.7 (a) Illustration of the concentric spherical cell model in a microfluidic FP cavity; (b) Calculated effective RI profile of a concentric sphere loaded optofluidic micro-cavity.

6.3.4 Introduction of the WKB method

Once the effective index method has been applied, the microsphere/cell loaded cavity can then be treated as a graded-index (GRIN) waveguide with an index profile calculated in Section 6.3.2 and Section 6.3.3. Wentzel, Kramers, and Brillouin have found good approximate solutions can be derived in the case of a slowly varying index profile. Their so-called WKB approximation involves keeping the form of the uniform-medium wave equation, but using a plane wave *k*-vector that can vary transversely. The wave equation in the cylindrical coordinates for azimuthal order v is $\frac{d^2}{dr^2}U(r)+\frac{1}{r}\frac{d}{dr}U(r)+\left[k_0^2n^2(r)-\beta^2-\frac{v^2}{r^2}\right]U(r)=0$. Under the assumptions of uniform waveguide along the z-direction and slowly varying radial index, e.g. neglecting any backscaterring, the equation can be integrated to give $\int_{r_1}^{r_2}\sqrt{k_0^2n^2(r)-k_0^2n_{eff}^2-\frac{v^2}{r^2}}dr=(m+\frac{1}{2})\pi$, where the boundary conditions require that the accumulated phase change is an odd integer multiple of π/2, m is the radial mode order, and n_{eff} is the effective refractive index of the mode.

A rule of thumb for applying the WKB approximation is that the index difference between the waveguide core and the cladding, $\Delta = \frac{n_{max}^2 - n_{min}^2}{2n_{max}^2} \leq 2\%$. However, Δ for a 10 μm diameter soda-lime microsphere (n=1.45) loaded 16 μm deep microfluidic cavity is ~ 5.2%. The index difference for cavities with PMMA and polystyrene spheres is larger although it is smaller for cell loaded microcavities. For example, Δ for a 10 μm diameter cell with an effective index of 1.40 loaded cavity is 4.9%, indicating that the WKB method is not suitable for solving transverse modes of cell loaded microfluidic cavities. Approximate values, $\Delta_{lymphocyte}$= 2.8% and $\Delta_{lymphoma}$= 3.2%, were obtained for cells based on the refractive indices for cytoplasm and nucleus derived from the measured canine cell spectra. The procedures of deriving cellular indices from the experimental data will be presented in Section 6.3.6.2.

The following section briefly describes the basic mode solving procedures under the WKB approximation. Interested readers may refer to reference [10] for the details of this popular GRIN waveguide mode solver. The phase condition for confined modes, $\int_{r_1}^{r_2} \sqrt{k_0^2 n^2(r) - k_0^2 n_{eff}^2 - \frac{\nu^2}{r^2}}\, dr = (m + \frac{1}{2})\pi$, is an implicit function of n_{eff} and needs to be solved numerically for most of the index profiles except for several special cases, for example, the parabolic index profile, where analytical solutions exist. To simplify the computation, a parabolic profile (the solid curve in Figure 6.7 (a)), $n_{WKB}(r) = \begin{cases} n_{max}\sqrt{1 - 2\Delta\left(\frac{r}{R}\right)^2} & if \quad |r| \leq R \\ n_0 & if \quad |r| > R \end{cases}$, was used to approximate the index profile calculated using the effective index method (the dashed curve in Figure 6.7 (a)),

$n(r) = \begin{cases} n_0 + (n_{\max} - n_0)\sqrt{1-\left(\frac{r}{R}\right)^2} & if \quad |r| \le R \\ n_0 \; if \quad |r| > R \end{cases}$, where n_{max} is the maximum refractive index of the equivalent waveguide. The analytical mode solution of confine waveguide modes corresponding to the parabolic index profile is $n_{eff}(m, v, \lambda) = n_{\max}\left[1 - \frac{2\sqrt{2\Delta}}{n_{\max} k_0(\lambda) R}(2m + |v| + 1)\right]$, where m and v is the radial and the azimuthal mode number respectively, and R is the core radius of the GRIN waveguide. Finally, the FP cavity's longitudinal resonant condition $n_{eff} = \frac{q\lambda}{2L_{cav}}$, where q is the longitudinal mode order, was applied as shown by the dashed lines in Figure 6.8 (b). The dots in Figure 6.8 (b) correspond to the resonant modes of the overall sphere-loaded FP cavity.

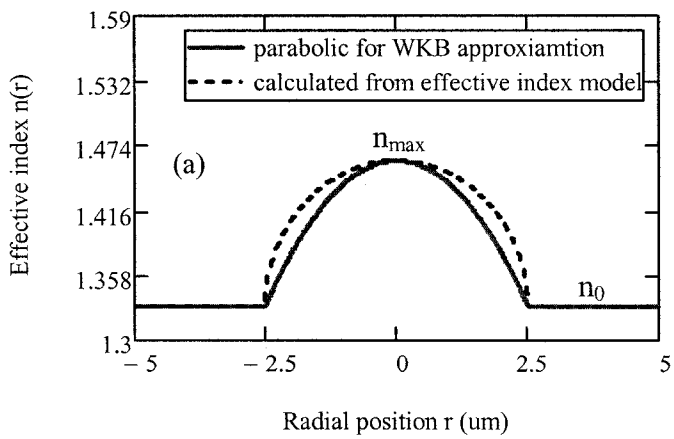

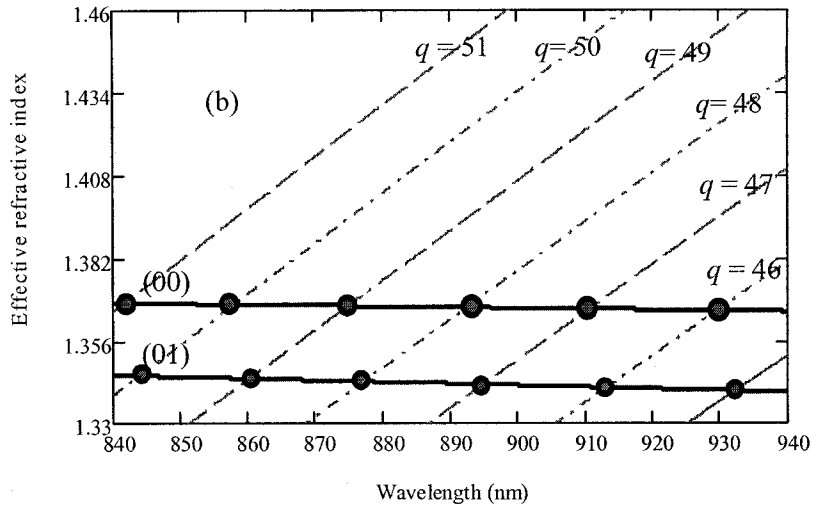

Figure 6.8 (a) Effective index profiles of a 5 μm diameter polystyrene sphere loaded microfluidic cavity calculated using the effective index model in Section 6.3.2 (dashed curve) and a parabolic approximation (solid curve). (b) Effective index of GRIN waveguide modes vs. wavelength under the WKB approximation.

Finite-difference beam propagation method (FD-BPM) is the other method useful for solving confined modes of waveguides with cylindrical symmetry. In this dissertation, the equivalent waveguide derived from the effective index mode was first defined using the CAD layout tool of RSoft. Parametric scans with respect to the wavelength were then performed to calculate the effective indices of all confined modes. It was found that the results generated by the commercial software lacked physical meaning. For example, the effective indices of confined modes can be simulated using FD-BPM, while the radial and azimuthal mode orders are unknown. Comparison of the modeling results using the WKB, RSoft-BPM, and the finite-difference numerical mode solver will be presented at the end of the chapter in Section 6. 5.

6.3.5 Finite-difference numerical mode solver

Another approach to solving for the eigenmodes of the equivalent waveguide derived from the effective index model is to compute solutions to the Helmholtz wave equation, $\nabla^2 E + \nabla(\frac{\nabla \varepsilon_r}{\varepsilon_r} E) + k_0^2 \varepsilon_r E = 0$, using a finite-difference method. The general solution to the scalar Helmholtz wave is taken as $E_t(r,\phi,z) = V(r)e^{iv\phi}e^{i(\omega t - \beta z)}$, where ν is the azimuthal mode number. Putting this general solution into the wave equation, it can be simplified to $\frac{d^2}{dr^2}V(r) + \frac{1}{r}\frac{d}{dr}V(r) + \frac{d}{dr}\left[\frac{1}{\varepsilon(r)}(\frac{d}{dr}\varepsilon(r)V(r))\right] + (k_0^2\varepsilon(r) - \beta^2 - \frac{v^2}{r^2})V(r) = 0$. A numerical mode solver was composed in MathCAD for this purpose. Figure 6.9 shows the calculated transverse mode profiles for a sphere loaded microfluidic cavity.

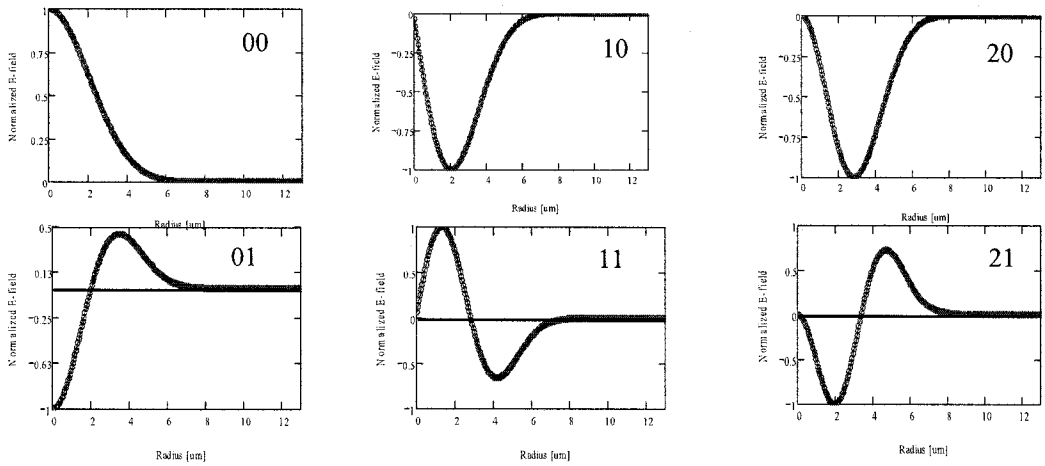

Figure 6.9 Transverse mode profiles calculated using the finite-difference numerical mode solver for an equivalent optical waveguide with cylindrical symmetry.

The numerical mode solver is able to find all the eigenmodes of the equivalent waveguide. The confined transverse modes have to satisfy a boundary condition, $n_{cav} \leq$

$n_{eff} \leq n_{max}$. Similar to the WKB and the FD-BPM methods, resonant modes of the overall sphere/cell-loaded FP cavity must satisfy the longitudinal mode condition, $n_{eff} = \frac{q\lambda}{2L_{cav}}$, to be satisfied. Detailed mathematical derivation and the numerical algorithm for the finite difference waveguide solutions are presented in Appendix D. The following section compares the modeling results on microsphere/cell loaded cavities from the various methods with the experimental results.

6.3.6 Comparison with experimental results

This section analyzes the spectral data presented in Chapter 5 and compares the modeling results using the effective index model and finite-difference numerical mode solver with the experimental results. The low repeatability of the transmission spectra of polystyrene spheres is explained and cellular refractive indices of canine lymphocytes and lymphoma are derived using the double sphere model introduced in Section 6. 3.3.

6.3.6.1 Sphere-loaded microfluidic cavities

As mentioned in Section 5.2 that the spectral repeatability of polystyrene spheres was not very good. For example, mode position and amplitude of similar sized polystyrene spheres varied greatly even within the same microfluidic cavity as shown in Figure 6.10.

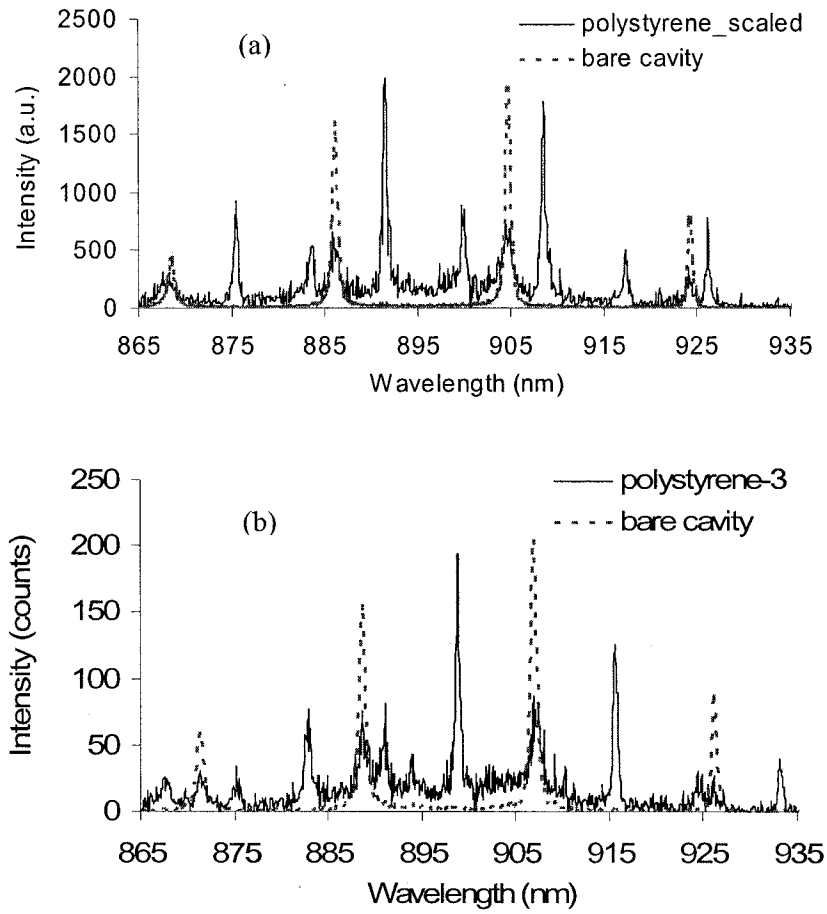

Figure 6.10 Measured cavity transmission spectra of a 10 μm diameter polystyrene sphere loaded 16 μm deep microfluidic cavity.

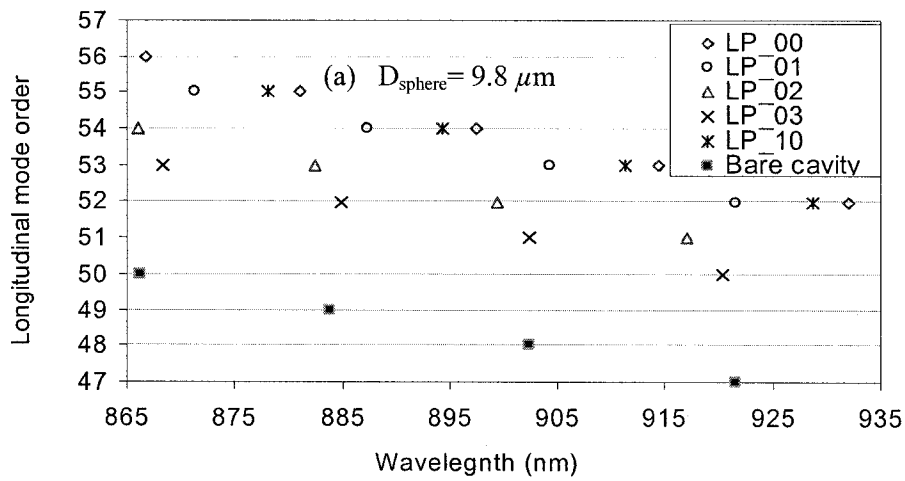

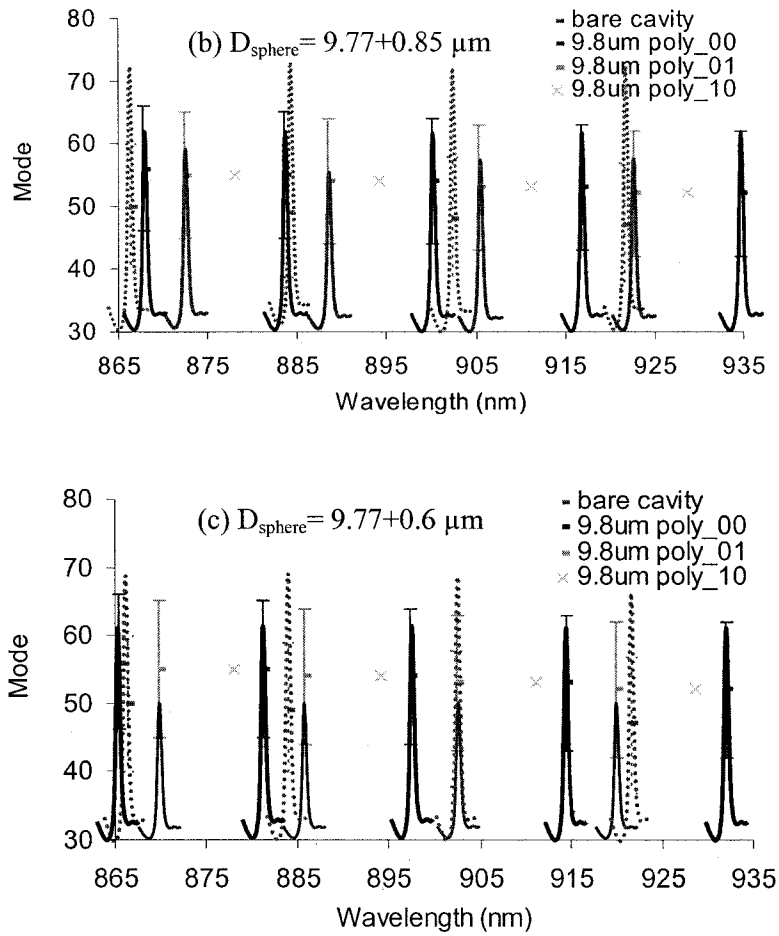

(c)

Figure 6.11 Simulated transmission spectrum of a 16 μm deep microfluidic cavity containing (a) 9.8 μm, (b) 9.77+0.85 μm, (c) 9.77+0.6 μm diameter polystyrene spheres.

The numerical calculations in Figure 6.11 show that transverse mode positions are very sensitive to the size change of the microsphere, especially for large refractive index spheres. For example, 11.58 ± 0.19 μm diameter soda-lime glass microspheres, ordered from Scientific Research Inc., have better spectral repeatability than 9.77 ± 0.85 μm diameter polystyrene spheres, ordered from Bangs Laboratory Inc. Figure 6.12 shows the measured and numerically calculated transmission spectra of a 11.58 μm diameter soda-lime glass sphere loaded microfluidic FP cavity. The spacing between bare cavity modes

and the neighboring transverse modes increase vs. wavelength, although only the lowest order transverse modes are measured in the experiments.

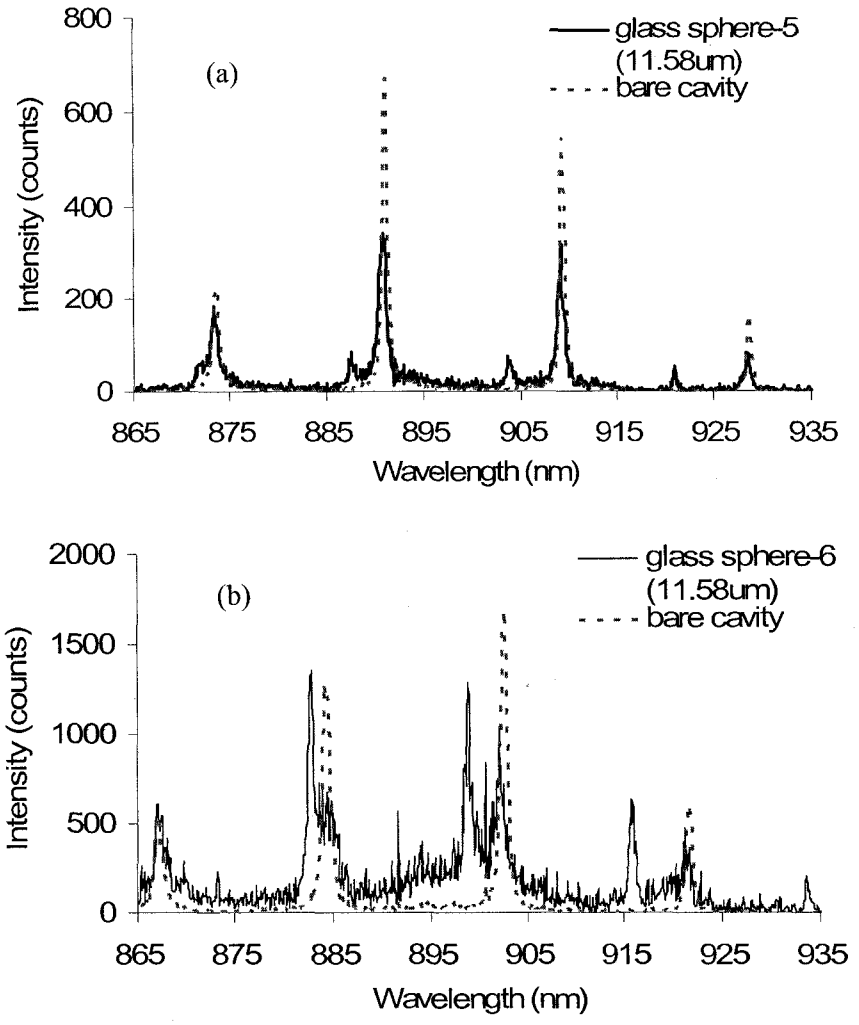

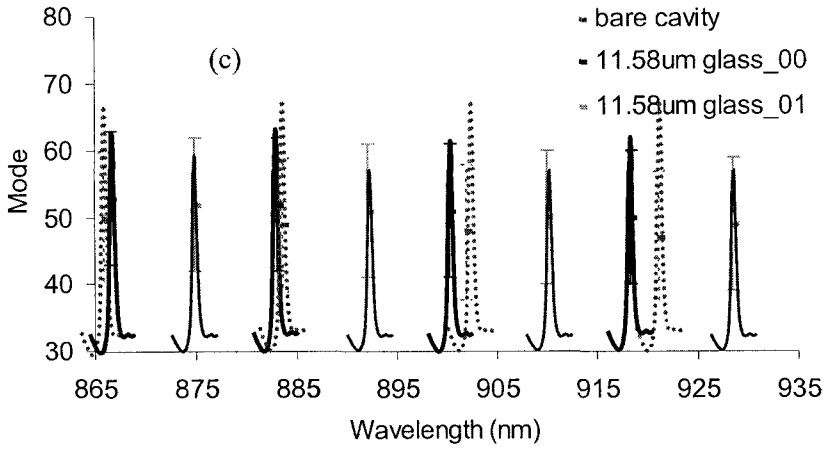

Figure 6.12 (a) and (b) measured, (c) simulated resonant mode spectra for a 11.58 ± 0.19 μm diameter soda-lime sphere loaded microfluidic cavity.

In summary, the effective index modeling shows that low refractive index spheres have larger transverse mode spacing than larger ones. The number of transverse modes that can be excited is related to both the refractive index difference and the size of the sphere or cell, which can be treated as an intracavity lens and thus affects the diffraction loss of the overall cavity. Theoretical modeling of cavity diffraction/scattering loss has not been done in this work. References [11] and [12] may provide insight into the modeling of losses induced by intracavity objects.

6.3.6.2 Cellular refractive indices calculation

The wavelength shift of cell modes from the bare cavity mode is related to the RIs and sizes of cellular features. Quantitative analysis of the spectra of canine lymphocytes and lymphoma was performed to extract RI information of cells with the help of the concentric double homogeneous RI sphere model shown in Figure 6.6 (a).

In the optical model, the overall cell radius was taken as R_2 = 6.5 μm based on microscopic measurements. The nuclear RI, n_1=1.3987, was first calculated from a 20.18 nm shift using a double sphere model with n_2 = 1.355 [13] as shown in Figure 6. 12 (b). And R_1 = 3.5 μm was used since the nuclear-to-cytoplasm volume ratio is approximately 1:5 for normal cells [14].

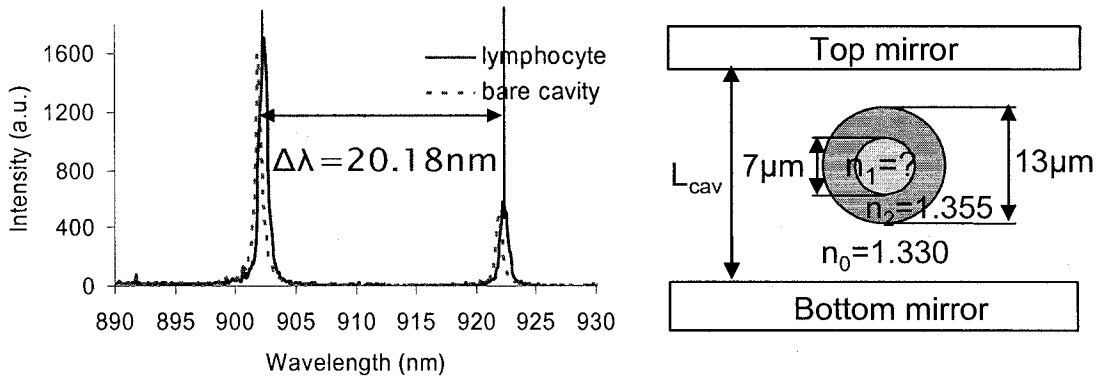

(a) (b)

Figure 6.12 (a) Spectral shift for a canine lymphocyte, and (b) The numerical model used for cellular RIs extraction. The numbers in blue color are measured from experiments and the numbers shown in red are taken from published literature.

Once the nuclear material RI was determined, the nuclear size of the cancerous lymphoma, R_1 = 4.457 μm, was calculated from the wavelength shift of 24.59 nm shown in Figure 6.13.

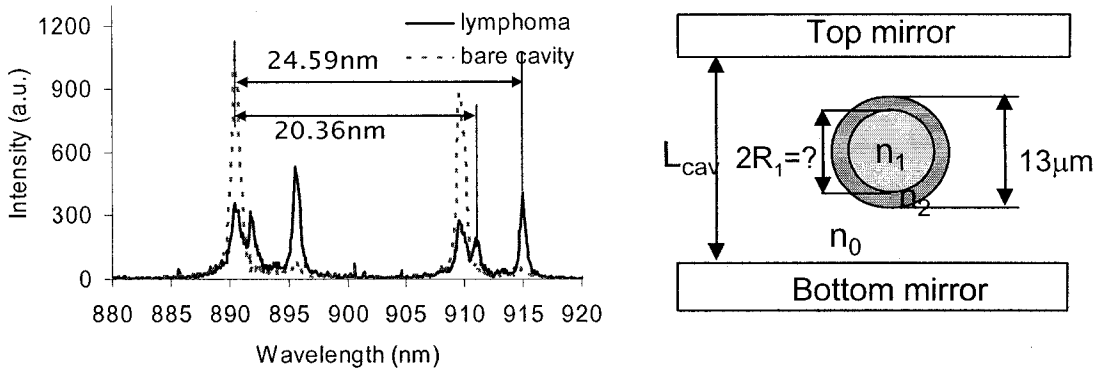

(a) (b)

Figure 6.13 (a) Spectral shift for a canine lymphoma cell, and (b) The numerical model used for cellular RIs extraction. The numbers in blue color are measured from experiments and the numbers shown in red are taken from published literature.

The effects of nuclear size and RI on the mode shift are illustrated in Figure 6.14 by computing the mode shift for varying nuclear radii, R_1, and RIs, n_1. Finally, the transverse modes were computed using the numerical mode solver discussed in Section 6.3.5 as shown by the solid lines in Figure 6.14 (a). For reference the wavelength shift calculated only on the axis of the cell while neglecting transverse mode confinement, referred to as the one-dimensional (1-D) model, is shown in dashed lines. Comparison of the two sets of curves highlights that transverse mode confinement effects are important for correctly interpreting mode shifts. The relationship between nuclear RI and size modeled for the experimentally observed nuclear mode shift of 24.59 nm is shown in Figure 6.14 (b).

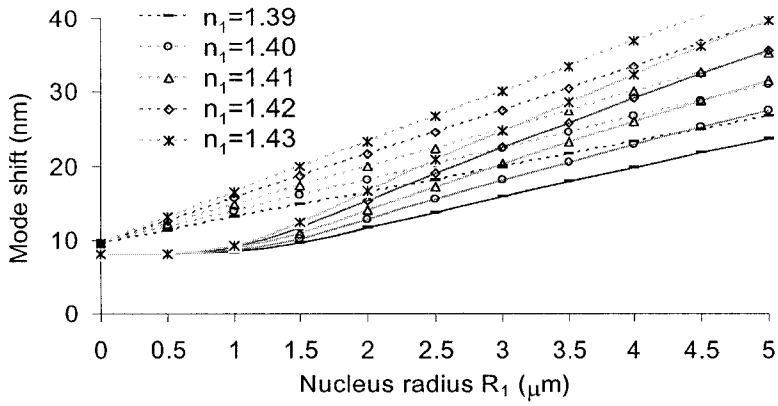

(a)

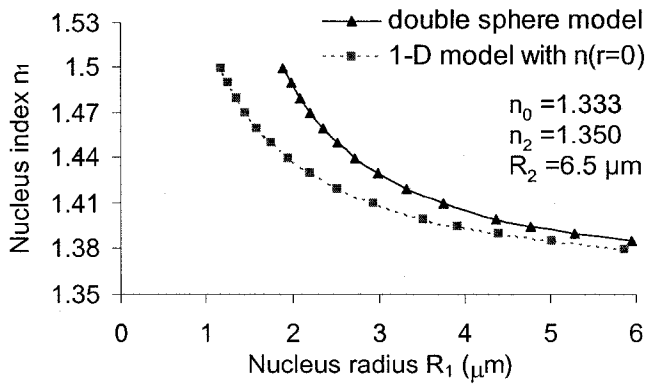

(b)

Figure 6.14 (a) Fundamental mode shift vs. nucleus size and refractive index calculated with lateral confinement (solid lines) and without lateral confinement using $n_{eff} = n(r=0)$ (dashed lines). (b) Nuclear index vs. radius by fitting the experimental spectrum of nuclear mode shift with the double-sphere model and the one-dimensional model.

The above results show that the double sphere model offers an improved estimate of nuclear RI, especially for cells with a small nucleus. If RIs are to be calculated, especially for cells with a small nucleus, lateral confinement effects should be considered as indicated by the double sphere effective index model.

6.4 Finite-difference time-domain simulation

Due to the 3D properties of the microsphere and the boundary conditions in the longitudinal direction determined by the interferometer, the exact solution of the cavity mode spectra is complex but can be solved by a full numerical method. The FDTD method, introduced by K. Yee in 1966 [15], appears to be one of the most widely used methods for optical waveguide applications. However, it also requires the most computer resources of any of the methods. In this work, numerical modeling of modal structures of sphere-loaded microcavities using FDTD method was performed. Preliminary simulation results using commercial software packages, Lumerical FDTD, OptiFDTD, and RSoft Fullwave, will be presented and discussed with a focus on RSoft Fullwave. Interested readers may refer to Appendix F for detailed parameter settings of specific simulations.

6.4.1 Assumptions

In order to simplify the simulation process and decrease the computing time, several assumptions were made. An assumption in the simulations presented below is made that the end mirrors are non-absorbing with a reflectivity of 95%. Replacing the gold or dielectric mirrors with hard mirrors simplified CAD layout within the FDTD software. This does not significantly change the resonant frequency of the FP cavity except setting the finesse or line width of the resonant modes, which was verified in RSoft Fullwave by a 10 μm deep bare fluidic cavity transmission spectrum shown in Figure 6.15 (a). The RSoft CAD layout tools use complex refractive indices to specify the dielectric properties of waveguides. Towards this goal, refractive index of the conductor is calculated. The reflectivity of a good conductor relates to its conductivity

through $R=\left[\left(1-\sqrt{\frac{2\omega\varepsilon_0}{\sigma}}\right)^2+1\right]/\left[\left(1+\sqrt{\frac{2\omega\varepsilon_0}{\sigma}}\right)^2+1\right]$, where ε_0 is the permittivity of free space and ω is the radial frequency of the light. σ also relates to the complex permittivity through $\varepsilon'=\varepsilon_r+i\sigma/\omega$. Therefore, σ of a 95% reflective good conductor at 890 nm is $5.697\cdot10^7\ S\cdot m^{-1}$. The propagation constant is $k=\omega\sqrt{\mu\varepsilon'}=\sqrt{\omega^2\mu\varepsilon_r+i\cdot\omega\mu\sigma}\cong\sqrt{i\cdot\omega\mu\sigma}$ and the complex refractive index is $n=k/k_0=(\beta+i\cdot\alpha)/k_0=\left(\sqrt{\omega\mu\sigma/2}+i\cdot\sqrt{\omega\mu\sigma/2}\right)/k_0$. Mathematical calculations showed that n = 38.993 + j·38.993 for a 95% reflective conductor.

FDTD simulations on the same structure using different grid size were performed until results did not change. This section will discuss the simulation results using RSoft Fullwave. Both FFT and DFT analysis can extract the cavity resonant spectra, except the simulation time and the spectral resolution are different. The spectral resolution, e.g. the line width of the resonant modes, is determined by the spatial grid size, which also determines the amount of simulation time. First, a bare fluidic cavity without any microsphere as shown in Figure 6.15 was laid out in the CAD window. A rectangular impulse (width=infinite, height=infinite, and length=1 μm located at (0, 0, -4.95)) was used to excite the cavity modes within the cavity. Periodic boundary conditions in the x and y direction allows the FDTD simulation to be performed on a small region, for example, 0.2 μm < x < 0.2 μm, -0.2 μm < y < 0.2 μm, -7 μm < z < +7 μm in this case. Figure 6.15 (a) and (b) shows the modeling results of FFT and DFT respectively. Identical simulation parameters, except the grid size in (a) $\Delta x = \Delta y = 0.05\ \mu$m and (b) $\Delta x = \Delta y = 0.01\ \mu$m, were used for FFT and DFT simulations respectively. However,

decreasing grid size for the FFT simulations did not change the wavelength of the resonant modes.

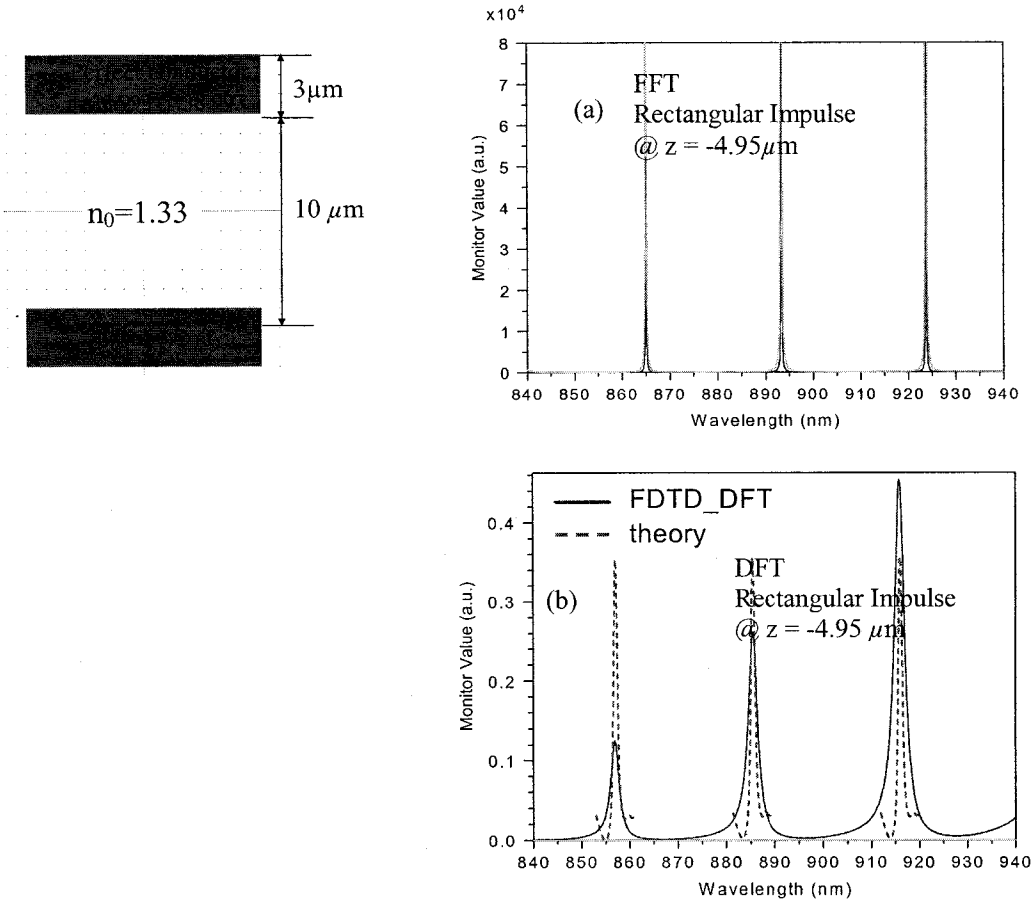

Figure 6. 15 FDTD simulation of the bare fluidic cavity spectrum using RSfot Fullwave. (a) FFT simulation computation grid $\Delta x = \Delta y = 0.05$ μm. Periodic boundary condition in the xy plane. (b) DFT simulation excited by the same rectangular impulse. Computation grid $\Delta x = \Delta y = 0.01$ μm. The dashed lines correspond to the theoretical calculations.

Surprisingly, the above results indicated that the bare cavity longitudinal mode wavelength calculated from DFT were different from those of the FFT although theoretically they should agree with each other. Figure 6.15 (b) shows that the theoretical calculation (dashed curve) agrees well with the DFT simulation results (solid curve).

Reasons for the discrepancy between the DFT and the FFT simulations are still unknown even with the help of the technical support from RSoft Inc.

6.4.2 RSoft Fullwave simulation results

Extensive FDTD simulations have been performed to study the effects of sphere position, refractive index, and size on the cavity transmission spectra. Both FFT and DFT analysis were performed in order to confirm the simulation results. Figure 6.16 shows FFT simulation results on a 5 μm diameter polystyrene sphere-loaded 10 μm deep fluidic cavity with (a) sphere at the center of the cavity and (b) sphere at the bottom of the cavity. The red bars correspond to the bare cavity longitudinal modes, which are consistent with the mode positions in Figure 6. 15 (a), although they do not agree with the theoretical and DFT simulation results shown in Figure 16.15 (b).

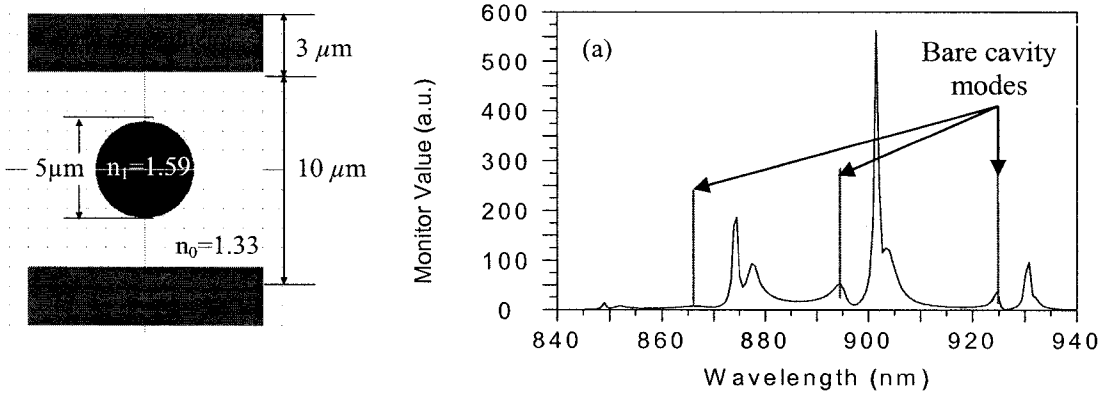

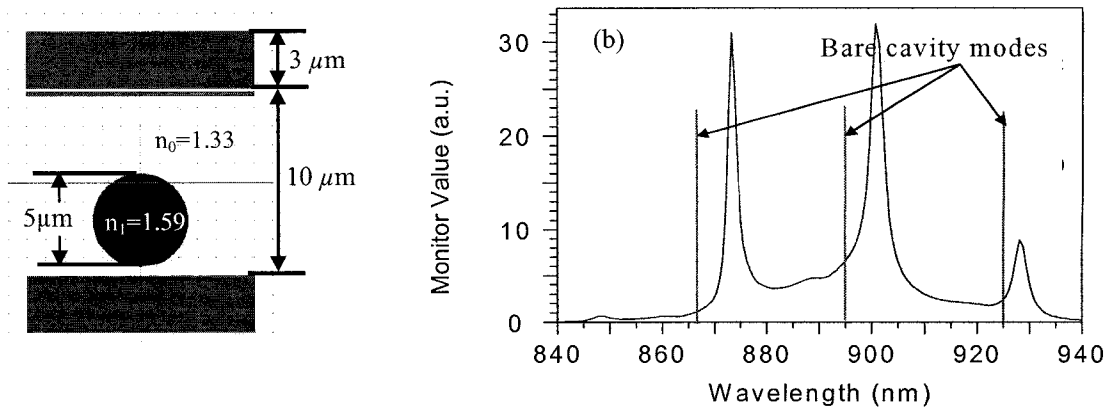

Figure 6.16 FDTD simulation results of a 5 μm diameter polystyrene sphere loaded FP cavity spectra (a) sphere at the center of the microfluidic cavity, (b) sphere at the bottom of the cavity. FFT analysis was used for both cases.

The above simulation results also indicate that the number of modes in the transmission spectrum is affected by sphere positions. Putting the sphere in the center of the microfluidic cavity is desirable in order to see more transverse modes. However, gravity of the sphere or cell pulls them to the bottom mirror if they stabilize inside the cavity naturally. Therefore, designing of microfluidic cavities capable of controlling the longitudinal position of the sphere or cell is critical. One possible solution is to pattern the negative DEP traps presented in Section 4. 6 on the superstrate of the microfluidic cavity to help place the sphere/cell in the center of cavity by balancing the gravity force.

In this work, simulations were repeated on the same structure until the results did not change. FDTD simulation time should be long enough in order to see all the transverse modes.

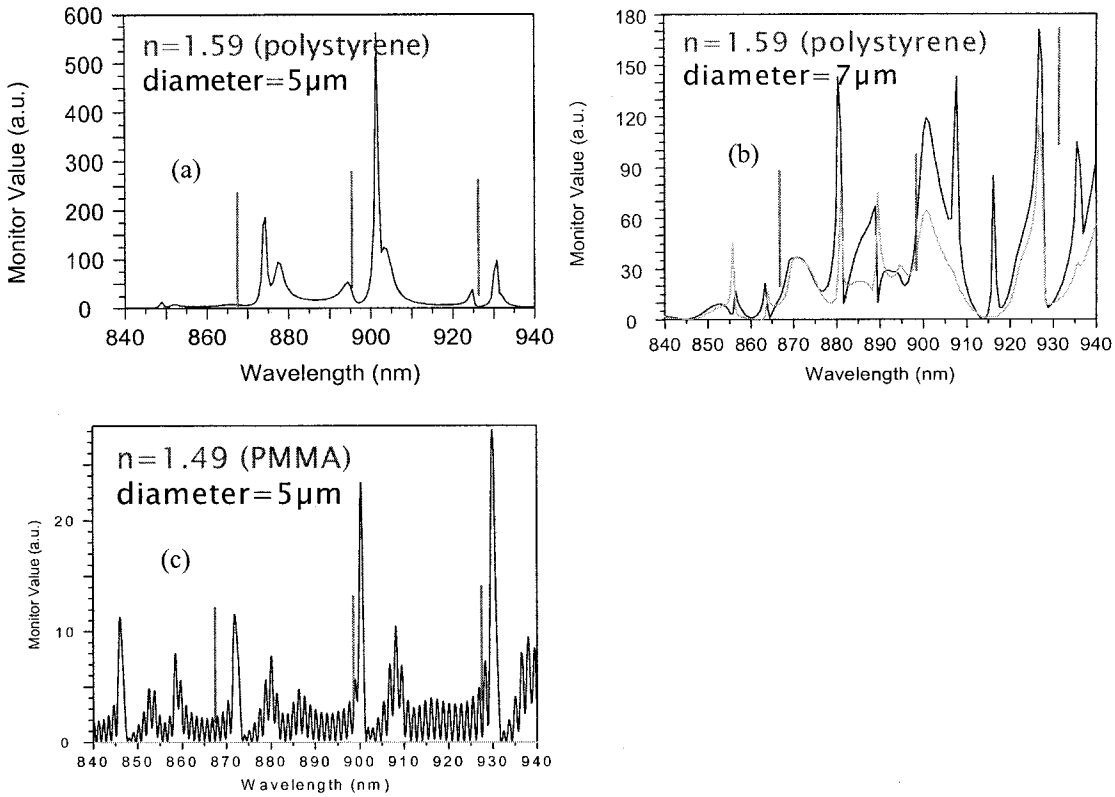

Figure 6.16 FDTD simulation results of a 5 μm diameter sphere, with different refractive indices, loaded FP cavity spectra.

It is difficult to interpret the trends in transverse mode number and wavelength shift from the above simulations. FDTD also requires large computer memory, for example, 2GB memory or a computer cluster is recommended by RSoft Inc., to simulate large spheres.

6.4.3 Lumerical FDTD simulation results

FDTD simulations were performed on a 2.45 GHz Pentium IV computer with 768 MB memory, which took ~28 hours. Figure 6.6 shows the transmission spectra of a 10 μm diameter polystyrene microsphere in the center of a 12 μm deep microfluidic cavity.

The rough agreement with the measured results in Figure 5.3 (b) indicates that the numerical models can be extended to analyze the refractive index profile of cells in FP micro cavities. Further analysis and testing of the boundary conditions and model accuracy should be done in the future work.

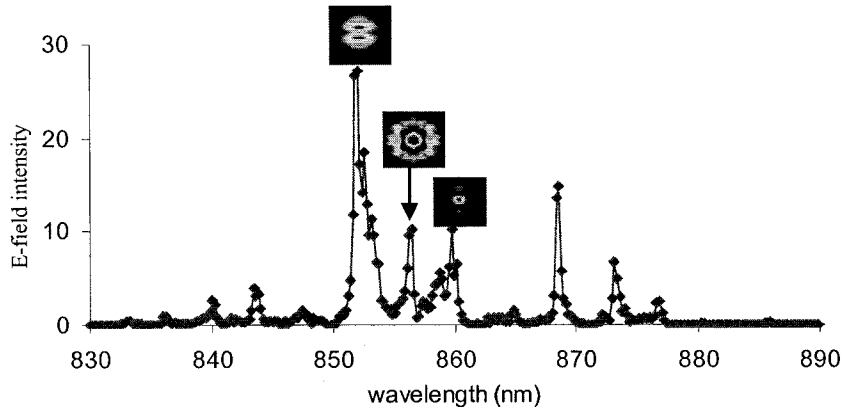

Figure 6.17 FDTD simulations of the transmission spectra of a 10 μm diameter polystyrene microsphere with refractive index of 1.59 in a 12 μm deep microfluidic cavity with refractive index of 1.33. The inserted plots show the mode patterns of the corresponding resonant modes.

6.4.4 OptiFDTD simulation results

Another commercial FDTD simulator tried in this work is made by OptiFDTD Inc. in Canada. A typical cavity configuration, a 10 μm diameter polystyrene sphere loaded 12 μm deep microfluidic cavity, was simulated by OptiFDTD Inc.'s technical staff since our group does not buy the license of this software package. A pulse was launched inside to the cavity to excite the transverse modes and propagates back and force between the etalons until resonant patterns were formed in the z-direction. The resonant mode spectrum can then be obtained by applying a FFT analysis and is shown in Figure 6.19. However, this result is quite different from that of the Lumerical FDTD simulation.

Resonant mode pattern may be obtained by running the simulation at a specific resonant wavelength once the resonant mode spectrum is calculated. No further efforts were devoted on OptiFDTD simulations after a month's communication with its technical support since the simulation results were not consistent.

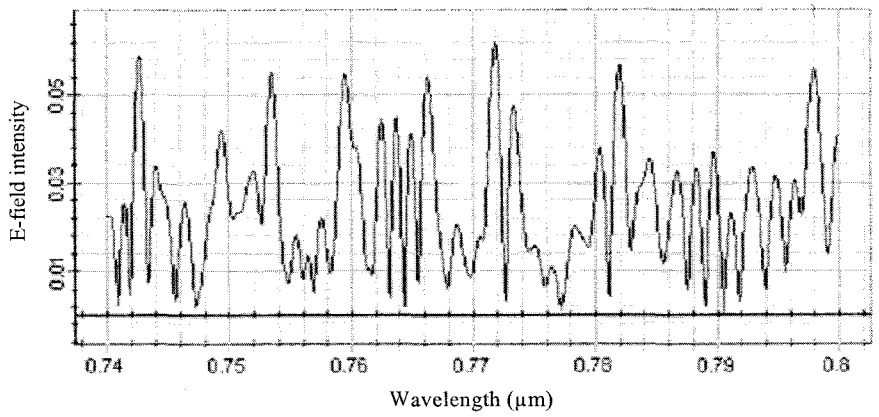

Figure 16.19 FDTD simulation of transmission spectrum of a 10 μm polystyrene sphere loaded 12 μm deep microfluidic cavity using the OptiFDTD simulator.

In summary, FDTD method provides a useful way to solve this type of problem since it directly solves the wave equations. However, FDTD has limited applications on large structures, >10 μm^3 due to the extensive computer resources for the implementation. Therefore, developing a computationally efficient, approximate theoretical model is important.

6.5 Comparison of different models

This section compares the simulation results using different models presented in this chapter. Table 6.1 summarizes the advantages and disadvantages of each method.

Table 6.1 Summary of advantages and disadvantages of various models.

Method	Advantages	Disadvantages
Paraxial Gaussian beam propagation method	1. Requires the least computational resources; 2. Allows resonator stability analysis; 3. Capable of modeling beam profiles and beam divergence angles; 4. Allows modeling the effects of sphere position changes; 5. Capable of calculating the transverse mode spacing & wavelegnth from Guoy phase shift.	1. Not suitable for non-paraxial cases; 2. Cannot predict cavity transmission spectrum; 3. Rough model that can provide only general trends of the transverse mode changes w.r.t. sphere index, position, and size.
Effective index method	1. Simple numerical algorithm that can simplify the dimension of waveguides from 3-D to 2-D.	1. Ignore the effects of lateral index change; 2. Does not allow diffraction loss calculations.
WKB method	1. Allows the prediction of cavity transmission spectrum; 2. Approximate analytical solutions allow easy understanding of transverse mode positions;	1. Work for waveguide with gradual and small lateral index changes; 2. Analytical solutions exist for special index profiles. 3. Requires lots of computational resources to solve the implicit phase function numerically.
RSoft finite difference BPM	1. Computational ly efficient; 2. Allows effective index calculation together with a scanning on wavelength; 3. Allows the prediction of cavity transmission spectrum; 4. Allows quick plotting of transverse mode pattern.	1. Not suitable for waveguides with big refractive index contrast in the beam propagation direction; 2. Cannot provide information on transverse mode orders.
Finite difference numerical mode solver	1. Computationally efficient; 2. Allows extraction of transverse mode order; 3. Allows quick plotting of transverse mode pattern.	
FDTD method	1. Full numerical method that can provide accurate results; 2. No other assumptions are needed except replacing dielectric mirrors with hard mirrors.	1. Requires the most computational resources; 2. Need >2GB computer memory or computer cluster for large 3-D structures. 3. Requires lots of practices on setting the simulation windows of the RSoft Fullwave; 3. Simulation results are not consistent for different cavity configurations; 4. Hard to interpret simulation results and needs to rerun the simulation at the resonant wavelength to generate transverse mode patterns;

Due to the large computational efforts of FDTD simulations, a 5 μm diameter polystyrene sphere loaded 10 μm deep microfluidic cavity was chosen to demonstrate differences in various models. Table 6.2 compares the mode positions predicted by each model. Figure 6. 21 shows the simulation results using various models discussed above.

Table 6.2 Comparison of simulated transverse mode $\lambda_{q,m,v}$ spectrum for a 5 μm diameter polystyrene sphere loaded 10 μm deep optofluidic FP cavity.

Method	Transverse mode spacing	Transverse mode position	Number of transverse modes exist	Variation with sphere position
Paraxial Gaussian BPM (sphere centered)	~ 21 nm	$\lambda_{33,0,1}$=874 nm $\lambda_{33,0,0}$=895 nm $\lambda_{32,0,1}$=901 nm $\lambda_{32,0,0}$=923.7 nm	N/A	Optimal sphere position is in the center of the cavity.
Paraxial Gaussian BPM (sphere at bottom ρ=0.1)	~ 23.2 nm	$\lambda_{33,0,1}$=872 nm $\lambda_{33,0,0}$=895 nm $\lambda_{32,0,1}$=898.7 nm $\lambda_{32,0,0}$=923.7 nm	N/A	
Effective index model & WKB with parabolic approximation	Not suitable due to the large refractive index contrast in the core and the cladding of the equivalent waveguides as shown in Figure 6.21 (b).			
Effective index model & finite difference BPM	~ 14 nm	$\lambda_{33,0,1}$=857 nm $\lambda_{33,0,0}$=871 nm $\lambda_{32,0,1}$=884 nm $\lambda_{32,0,0}$=898 nm	N/A Higher order modes have greater loss than fundamental modes.	No
Effective index model & numerical mode solver	~ 24 nm	$\lambda_{33,0,1}$=850 nm $\lambda_{33,0,0}$=874 nm $\lambda_{32,0,1}$=877 nm $\lambda_{32,0,0}$=902 nm	N/A	No
FDTD using RSoft Fullwave (sphere centered)	~ 24.5 nm	$\lambda_{?,?,?}$ = 874 nm $\lambda_{?,?,?}$ = 877.5 nm $\lambda_{?,?,?}$ = 902 nm $\lambda_{?,?,?}$ = 904 nm	2	Optimal sphere position is in the center of the cavity.
FDTD using RSoft Fullwave (sphere at bottom)	N/A	$\lambda_{?,?,?}$ = 874 nm $\lambda_{?,?,?}$ = 902 nm	1	Some of the transverse modes disappear.

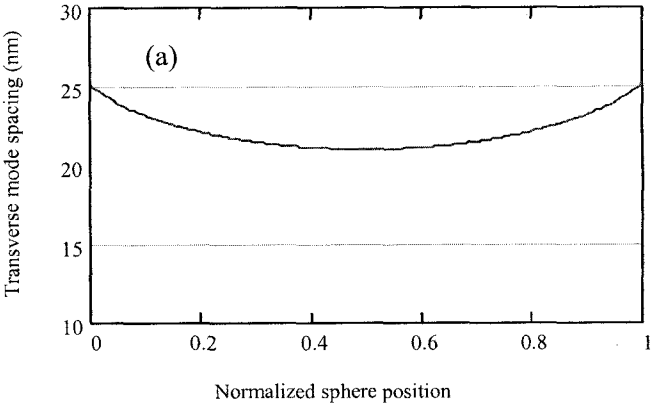

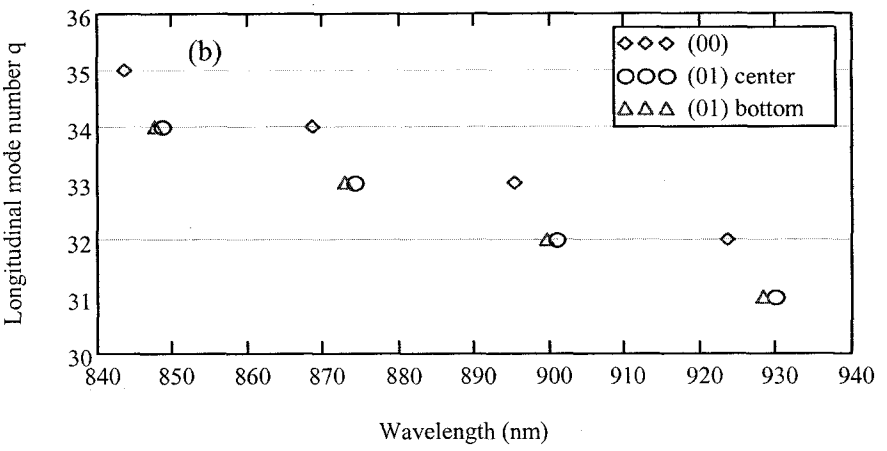

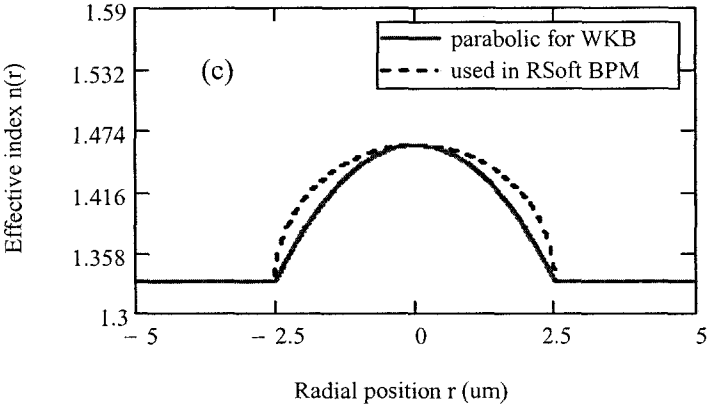

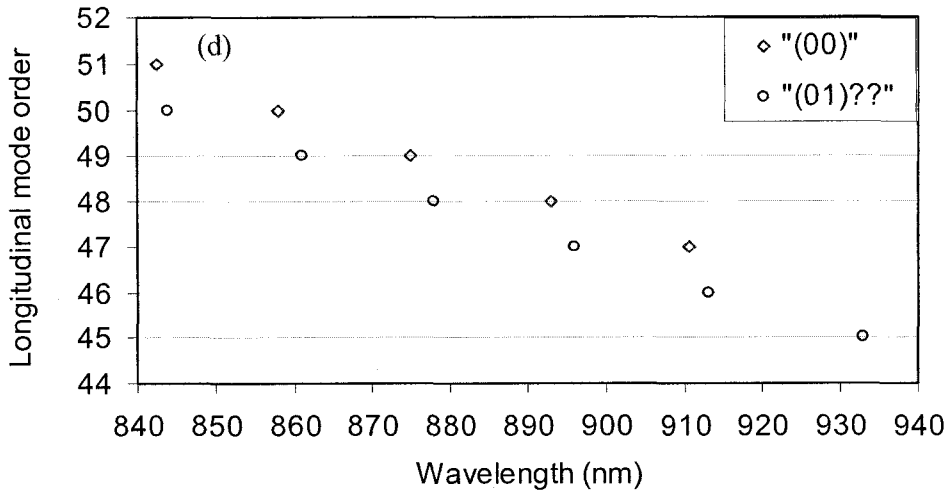

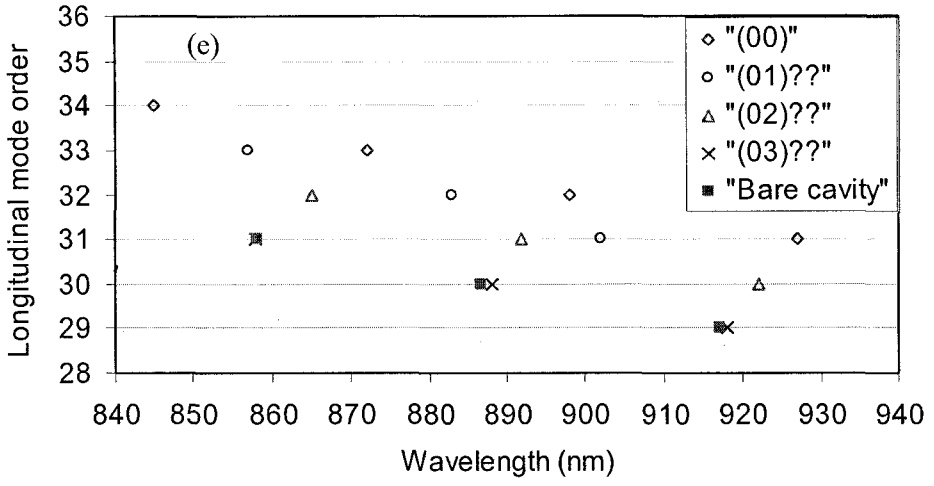

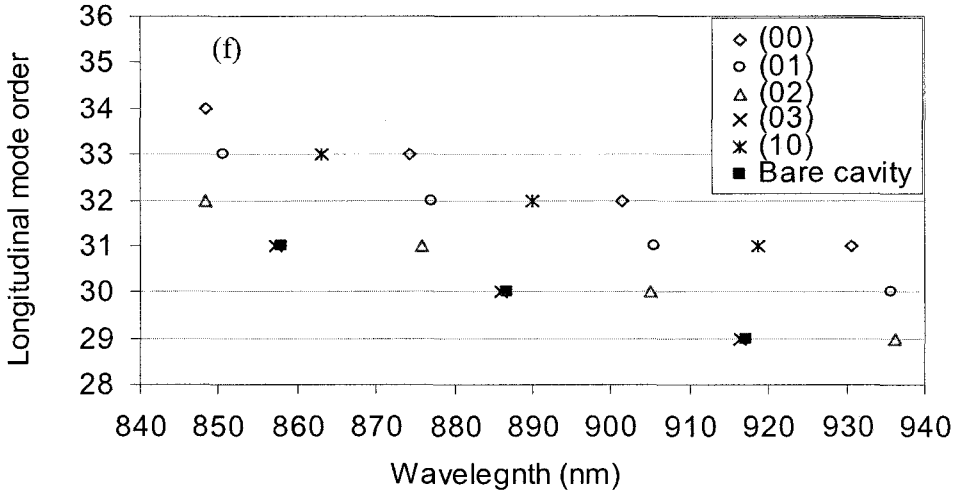

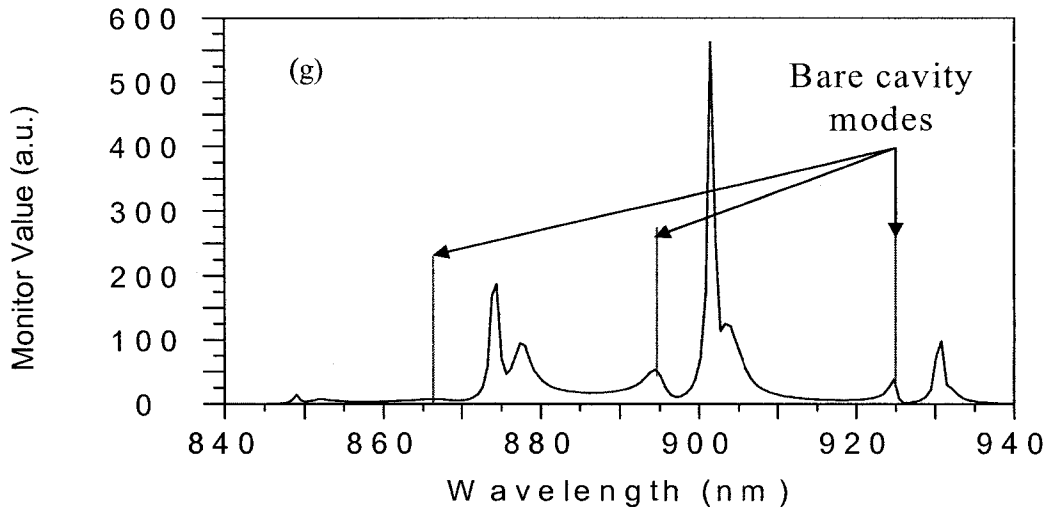

Figure 6.21 (a) Transverse mode spacing calculated using paraxial Gaussian BMP; (b) The wavelength of transverse modes calculated from $q2\pi = \phi_{Guoy} + \frac{2\pi}{\lambda} 2[n_s 2R + n_{cav}(L_{cav} - 2R)]$; (c) Effective index profile calculated from Hadley's effective index model; (d) Result of the WKB method; (e) Result of the effective index model and the RSoft finite-difference BPM; (f) Result of the effective index model and the finite-difference numerical mode solver; (g) Result of FDTD simulation using RSoft Fullwave.

In summary, multiple types of theoretical modeling of the transmission spectra have been studied. Rough agreement between the experimental and the theoretical modeling results indicates that the method developed here may be useful in analyzing the refractive index profile of biological cells in interferometer based biosensors.

References

[1] P. L. Gourley, "Biocavity laser for high-speed cell and tumour biology", *J. Phys. D: Appl. Phys.*, vol. 36, R228–R239, 2003.

[2] K. E. Meissner, P. L. Gourley, and T. M, Brennan, et al., "Intracavity spectroscopy in vertical cavity surface-emitting lasers for micro-optical-mechanical systems", *Appl. Phys. Lett.*, vol. 69, no.11, pp.1517-1519, 1996.

[3] G. Q. Zhou, K. C. Zhu, F. Q. Liu, "Analytical structure of the TE and TM terms of paraxial Gaussian beam in the near field", *Optics Communications*, vol. 276, no.1, pp. 37-43, 2007.

[4] A. E. Siegman, *Lasers.* Mill Valley, CA: University Science, 1986.

[5] J. Yang and H. G. Winful, "Generalized eikonal treatment of the Guoy phase shift", *Opt. Lett.*, vol. 31, no. 1, pp. 104, 2007.

[6] J. U. Nöckel, "Modified Guoy phase in optical resonators with mixed boundary conditions, via the Born-Oppenheimer method", *Optics Express*, vol. 15, no. 9, pp. 5761, 2007.

[7] G. R. Hadley, "Effective-index model for vertical-cavity surface emitting lasers", *Opt. Lett.*, vol. 20, no. 13, 1995.

[8] K. W. Keohane and W. K. Metcalf, "The cytoplasmic refractive index of lymphocytes, its significance and its changes during active immunization", *Q J Exp Physiol. Cogn. Med. Sci.*, vol. 44, pp. 343, 1959.

[9] P. M. A. Sloot, A. G. Hoekstra, and C. G. Figdor, "Osmotic response of lymphocytes measured by means of forward light scattering: theoretical considerations", *Cytometry*, vol. 9636, pp. 636, 1988.

[10] S. W. Corzine and L. A. Coldren, Diode Lasers and Photonic Integrated Circuits. John Wiley and Sons Inc. 1996.

[11] E. R. Hegblom, D. I. Babic, B. J. Thibeault, and L. A. Coldren, "Estimation of scattering losses in dielectrically apertured vertical cavity lasers", *Appl. Phys. Lett.*, vol. 68, no. 13, pp. 1757, 1996.

[12] B. J. Thibeault, E. R. Hegblom, P. D. Floyd, R. Naone, Y. Akulova, and L. **A.** Coldren, "Reduced optical scattering loss in vertical-cavity lasers using a thin (300 A*)* oxide aperture", *IEEE Photon. Tech. Lett.,* vol. **8,** no. 5, pp.593, 1996.

[13] A. N. Shvalov, I. V. Surovtsev, A. V. Chernyshev, J. T. Soini, and V. P. Maltsev, "Particle classification from light scattering with the scanning flow cytometer", *Cytometry*, vol. 37, no. 3, 1999.

[14] C. Liu and C. E. Capjack, "Effects of cellular fine structure on scattered light pattern", *IEEE Trans. on Nanobioscience*, vol. 5, no. 2, pp. 76, 2006.

[15] K. Yee, "Numerical solution of initial boundary value problems involving Maxell's equations in isotropic media", *IEEE Transactions on Antennas and Propagation,* vol. 14, pp. 302, 1966.

[16] D. C. O'Shea, "Elements of Modern Optical Design", *Wiley-Interscience*, New York, pp. 247–252, 1985.

[17] A. Yariv, "Optical Electronics in Modern Communications", *Oxford U. Press*, New York, 5th ed., 1997, Chapter 2.

[18] G. Machavariani, N. Davidson, A. A. Ishaaya, and A. A. Friesem, "Improving the stability of longitudinal and transverse laser modes", *Optics Communications*, vol. 239, pp. 147-151, 2004.

Chapter 7

Summary and Future Work

This chapter summarizes contributions of this dissertation to developing optofluidic intracavity spectroscopic biosensing systems for single biological cell identification. Section 7.1 summarizes achievements related to the fabrication and the testing of optofluidic Fabry-Pérot (FP) cavities as well as the optical modeling of cavity transmission spectra. Section 7.2 presents suggestions for future work in the quest of lab-on-a-chip and automatic optofluidic intracavity spectroscopic biosensors.

7.1 Contributions of the dissertation

A label-free and low-cost single biological cell identification system, employing optofluidic intracavity spectroscopy, is proposed and developed in this dissertation. The developed biosensor structure allows the integration of dielectric mirrors into microfluidic cavities and on-chip single cell dielectrophoretic (DEP) trapping. Below is a summary of contributions of this dissertation. Much of the work has been published in journals [1-3] and conference presentations [4-12].

Complete fabrication processes for gold-coated and dielectric mirrors coated optofluidic cavities were developed using low cost transparency photomasks, which can be easily performed using simple fabrication equipment. For the 1st generation gold coated devices, the fabrication takes advantage of using Cr/Au layers both as a wet etching mask and as intermediate bonding layers, requiring only one lithography step for the entire process. The 2nd generation devices utilizing HfO_2/SiO_2 dielectric mirrors,

which are compatible with water and also stable during thermo compressive gold bonding processes.

Critical fabrication steps that affect the performance of the optofluidic cavities were studied with scanning electronic microscopy, atomic force microscopy, and optical spectroscopy. Theoretical modeling of cavity finesse due to mirror roughness and tilt shows good agreement with the measured value. An optofluidic cavity with a finesse of above 40 and a mirror tilt $< 1^0$ was demonstrated.

A customized, low-cost and multi-functional optical spectroscopic system was designed to measure the transmission spectra of optofluidic cavities. The customized microscope system allows fluorescence imaging with suitable filters, which help identify.

Transmission spectra of different types of biological cells and microspheres were measured and analyzed. The order of each mode was identified experimentally and verified this theoretically. The lateral optical confinement of cancerous cells within passive microfluidic FP cavities was thoroughly investigated. Numerical models using Gaussian beam propagation method (BPM) and effective refractive index method were developed to simulate the transmission spectra of sphere and cell-loaded optofluidic cavities. An effective index model has been developed to explain the multimode spectra of cancerous cells and explore the nuclear size vs. refractive index relationship. This label-free technique provides a tool for studying the nuclear status of cancerous cells, which is beyond the capability of conventional flow cytometry relying on light scattering and cell staining.

Initial DEP trapping of single microspheres and biological cells within an optofluidic cavity were demonstrated with 10Vpp AC voltages, which allows single cell identification in a more controllable format.

7.2 Future work and discussion

Overall, passive optofluidic FP cavities are proven to meet the needs for recognizing single biological cells in a fluidic environment. The work reported in this dissertation can be extended to realize an automatic sensing system by integrating DEP traps and electronic control circuits into the optofluidic cavities. This section proposes some future work that can be implemented onto OFIS sensors to improve their overall performance.

1) Pursue fluid flow control with the help of syringe pumps to realize uniform flow rate of the micro particles;
2) Design mechanical clamps to for thermal compressive gold-to-gold diffusion bonding of large glass chips;
3) Design new DEP traps to decrease single particle trapping time by guiding micro-particles to flow near the DEP traps;
4) Design a particle trapping feedback control system to realize automatic cell trapping and releasing. For example, a trap release signal can be generated from the transmitted optical intensity with the help of a fiber splitter and a photodiode. The release signal can be triggered after the particle being trapped for certain amount of time, which allows the spectrometer to record the transmission spectra of the cells.

5) Combine DEP trapping with optofluidic intracavity spectroscopy to identify single biological cells in a more controllable way. Cell properties such as impedance may be detected and used for cell recognition as well;
6) Bury DEP micro-electrodes beneath the dielectric mirror to prevent the contamination of the electrodes;
7) Investigate different illumination schemes, such as tilted illumination apparatus with a better control over the tilt angle, to study the effects of tilt on the excitation of high order transverse modes of cells;
8) Scan the cavity with a tunable laser to decide the order of high order modes by observing the mode patterns with a CCD camera or an imaging spectrometer;
9) Integrate the LED and the spectrometer into microfluidic chips for lab-on-a-chip biosensors.
10) Simulate double homogeneous sphere loaded FP cavity spectral using RSoft Fullwave.

References

[1] H. Shao, W. N. Wang, S. E. Lana, and K. L. Lear, "Optofluidic intracavity spectroscopy of canine lymphoma and lymphocytes", submitted to *IEEE Photonics Technology Letters*, July 2007, in revision.

[2] H. Shao, D. Kumar, and K. L. Lear, "Single cell detection using optofluidic intracavity spectroscopy", *IEEE Sensors Journal,* 6 (6): 1543-1550, December 2006.

[3] H. Shao, D. Kumar, S. A. Feld, and K. L. Lear, "Fabrication of a Fabry-Pérot cavity in a microfluidic channel using thermocompressive gold bonding of glass substrates", *IEEE Journal of MEMS*, 14 (4): 756-762, August 2005.

[4] H. Shao, W. N. Wang, S. E. Lana and K. L. Lear, "Optofluidic intracavity spectroscopy of single cells in a passive Fabry-Perot resonator", to be presented at *2007 APS March Meeting*, paper B38.00006 , Denver, Colorado, March 5, 2007.

[5] W. N. Wang, H. Shao and K. L. Lear, "Lab-on-a-chip single particle dielectrophoretic traps", to be presented at *2007 APS March Meeting*, paper L30.00006, Denver, Colorado, March 6, 2007.

[6] H. Shao, S. E. Lana, and K. L. Lear, "Intracavity Spectroscopy of Canine Lymphoma Cells in a Microfluidic Channel", oral presentation in the Biophotonics I: Multimodal Imaging / Spectroscopic Techniques, *IEEE LEOS 19th Annual Meeting*, Montreal, QC, Canada. Oct. 30-Nov. 2, 2006.

[7] H. Shao and K. L. Lear, "Optofluidic Intracavity Spectroscopic Characterization of Standard Microparticles", oral presentation in the Nonlinear Microscopy and Spectroscopy session, *IEEE LEOS 19th Annual Meeting*, Montreal, QC, Canada. Oct. 30- Nov. 2, 2006.

[8] D. Kumar, H. Shao, and K. L. Lear, "Microfluidic interferometer", *LACSEA*, February 2006.

[9] H. Shao, D. Kumar, and K. L. Lear, "Single cell detection capability of an optofluidic spectroscopic biosensor", oral presentation in the microfluidic devices & systems lecture session A2L-C, *IEEE Sensors Conference,* Irvine, California, Oct 31- Nov 1, 2005.

[10] H. Shao, D. Kumar, and K. L. Lear, "Micro-fluidic passive cavity interferometer based biosensor", oral presentation in the microfluidics, flow cytometry, and biosensing session CFF-3, *CLEO/QELS*, Baltimore, Maryland, May 22-27, 2005.

[11] H. Shao, D. Kumar, S. A. Feld and K. L. Lear, "Micro-fluidic passive cavity interferometer based biosensor", oral presentation in the optical fluidic devices & bio sensors session MM, *IEEE LEOS 17th Annual Meeting,* vol. 1, pp. 120-121, November 7-11, 2004.

[12] H. Shao, D. Kumar and K. L. Lear, "Micro-fluidic passive cavity interferometer based biosensor", oral presentation at the *49th Annual SPIE Conference*, Denver, August 4-8, 2004.

Appendix A

Experiments on Optical Tweezers

Section A.1 of this appendix covers the general background of optical tweezers followed by their applications in Section A.2. Section A.3 goes on to present the fundamental operation principle of the optical tweezers. Features of modern optical tweezers are presented in Section A.4. Section A.5 discusses about the experimental setup of the optical tweezers in our lab together with the movie clip of the optical trapping of polystyrenes. The major reference for this appendix is the optical tweezers website of Stanford University [1].

A.1 Background of optical tweezers

A strongly focused laser beam has the ability to catch and hold particles ranging in size from nm to μm were first demonstrated by A. Ashkin *et al.* in 1984 at Bell laboratories [2]. This technique, also called optical tweezing or trapping, makes it possible to study and manipulate particles like atoms, molecules (even large) and small dielectric spheres.

A.2 Applications

Optical tweezers have been used to trap dielectric spheres, viruses, bacteria, living cells, organelles, small metal particles, and even strands of DNA. Applications include confinement and organization (e.g. for cell sorting) [3], tracking of movement (e.g. of

bacteria) [4], measurement of small forces [5], and altering of larger structures (such as cell membranes) [6]. Combined with a laser scalpel (use of lasers for cutting and ablating biological objects), optical tweezers have been used to study cell fusion [7] and DNA-cutting [8]. A review on uses of optical tweezers can be found in A. Ashkin's paper tilted "Optical trapping and manipulation of neutral particles using lasers" [9].

The most basic form of an optical trap is diagramed in Figure A.1 (a). A laser beam is focused by a high-quality microscope objective to a spot in the specimen plane. This spot creates an optical trap, which is able to hold a small particle at its center. The forces felt by this particle consist of the light scattering and gradient forces due to the interaction of the particle with the light as illustrated in Figure A.1 (b). Most frequently, optical tweezers are built by modifying a standard optical microscope.

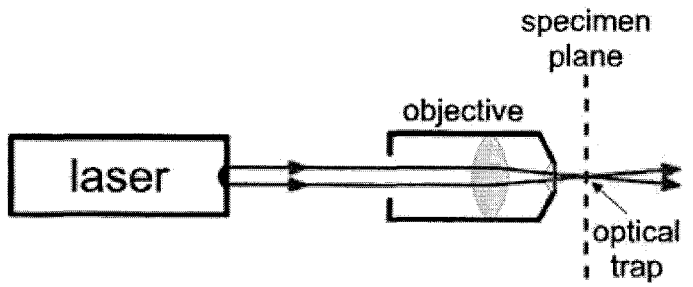

(a)

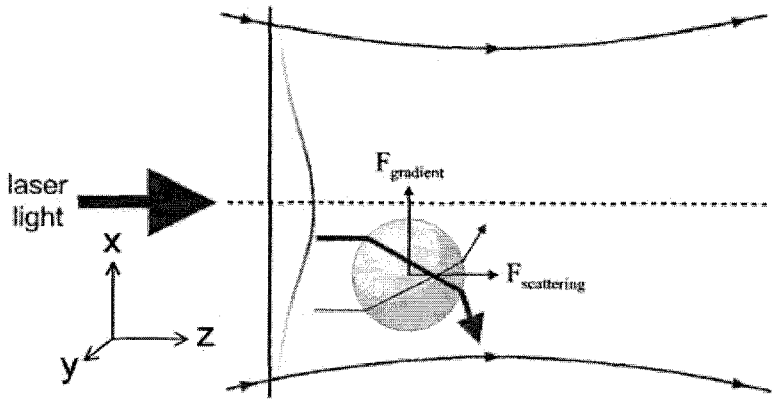

(b)

Figure A.1 (a) Schematic diagram of a simple optical tweezer. (b) Optical forces in an optical tweezer. (Reproduced from Reference [1])

A.3 Principle of operation

The basic principle behind optical tweezers is the momentum transfer associated with bending light. Figure A.1 (b) shows a more detailed look at how an optical trap works. Light carries momentum that is proportional to its energy and in the direction of propagation. Any change in the direction of light, by reflection or refraction, will result in a change of the momentum of the light. If an object bends the light, changing its momentum, conservation of momentum requires that the object must undergo an equal and opposite momentum change. This gives rise to a force acting on the object.

In a typical optical tweezers setup the incoming light comes from a laser which has a "Gaussian intensity profile". Basically, the light at the center of the beam is brighter than the light at the edges. When this light interacts with a bead, the light rays are bent according the laws of reflection and refraction as shown in Figure A.1 (b). The sum of the forces from all such rays can be split into two components: $F_{scattering}$, the scattering force, pointing in the direction of the incident light, and $F_{gradient}$, the gradient force, arising from the gradient of the Gaussian intensity profile and pointing in x-y plane towards the center of the beam. The gradient force is a restoring force that pulls the bead into the center. If the contribution to $F_{scattering}$ of the refracted rays is larger than that of the reflected rays then a restoring force is also created along the z-axis, and a stable trap will exist. Detailed analysis of the forces in an optical trap could be found in references [10-12].

A.4 Modern optical tweezers

In practice, optical tweezers are very expensive, custom-built instruments. These instruments usually start with a commercial optical microscope but add extensive modifications. In addition, the capability to couple multiple lasers into the microscope poses another challenge. High power infrared laser beams are often used to achieve high trapping stiffness with minimal photo-damage to biological samples. Precise steering of the optical trap is accomplished with lenses, mirrors, and acousto/electro-optical devices that can be controlled via computer.

A.5 Experiments on optical trapping of polystyrene spheres

This section talks about the optical design of the optical tweezer in our lab. The photographic picture and a representative diagram of the optical setup of the laser tweezer are shown in Figure A.3 (a) and (b) respectively. The optical beam (~1 mm in diameter) from a frequency doubled Nd_YAG laser (λ=513 nm, peak power 500 mW) was expanded by a factor of 6 using two biconvex lens before reaching the microscope objective lens. A microscope objective (40x, 0.65NA) with an effective focal length of ~ 2.8 mm was used to focus the laser beam onto the microfluidic cavity plane. The expansion of the laser beam is necessary in order to fulfill the back aperture of the microscope objective lens and produce the tightly focused incident light to create a stable optical trap.

The focused beam was then used to trap the polystyrene spheres inside the microfluidic cavity. Here, the microfluidic cavity is formed between a cover slip substrate (125 μm thick) and a glass slide (1 mm thick) superstrate without wafer

bonding. The use of a thin cover slip instead of a glass slide as the substrate is necessary in order to move the focal point of the excitation light within the fluidic cavity. The customized microscope system on top of the microlfuidic cavity is the same as that used in the intracavtiy spectroscopy experiments. A 570 nm long pass filter was inserted in front of the CCD camera to prevent the saturation of the camera.

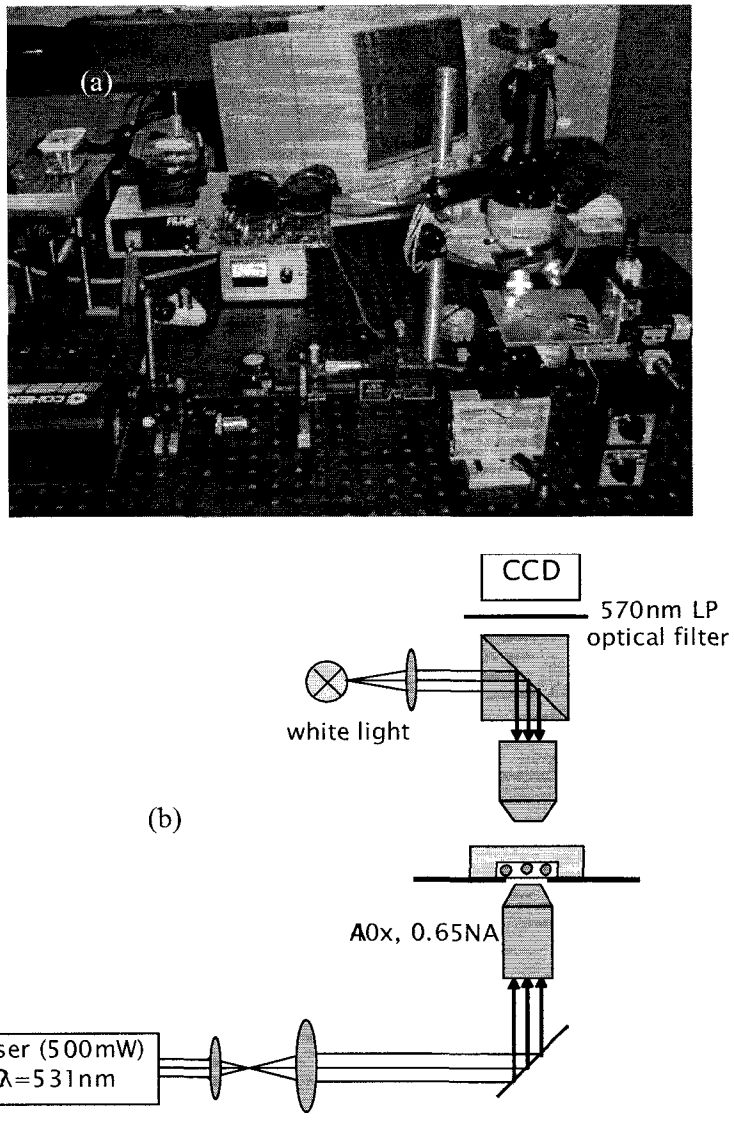

Figure A. 3 (a) The photographic image of the optical tweezer, and (b) Schematic diagram of the optical tweezer.

With the experimental setup shown in Figure A. 3 (a), we successfully trapped 2 μm, 5 μm, and 10 μm diameter polystyrenes. Figure A. 4 shows the movie clips of the optical trapping of the 5μm diameter polystyrene sphere.

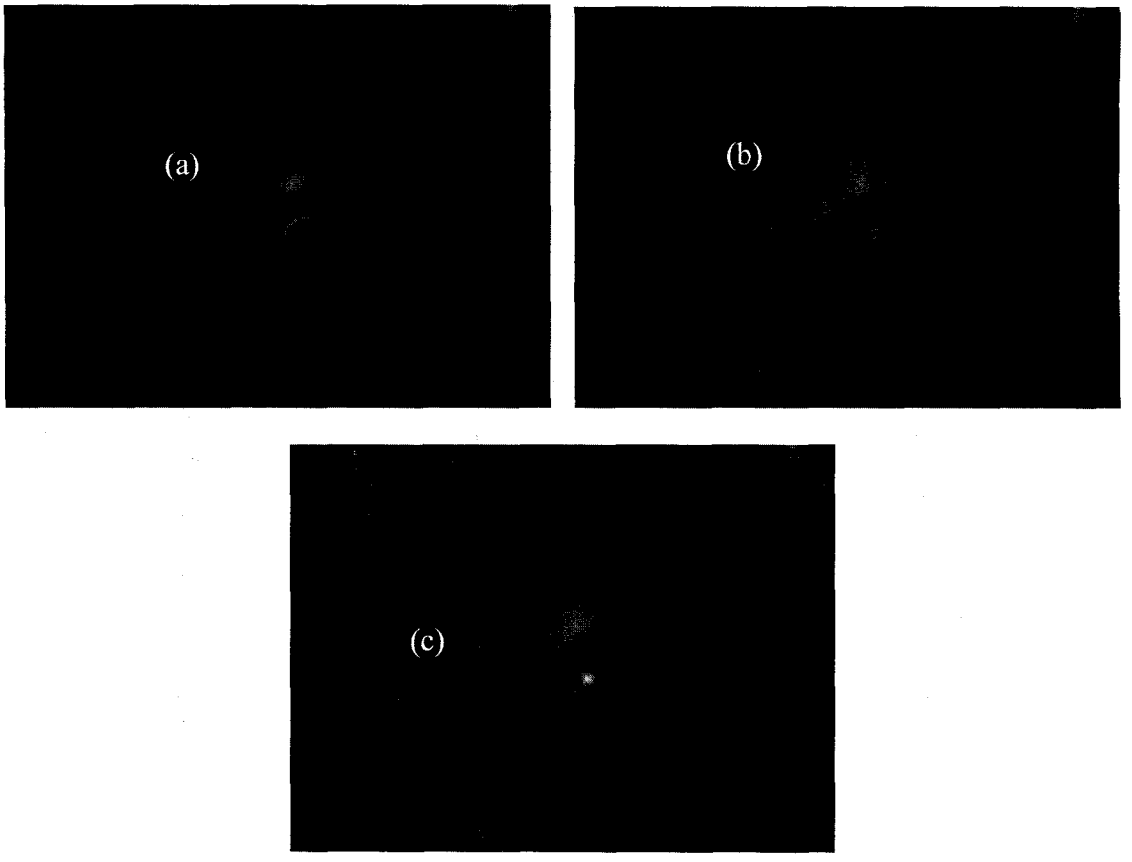

Figure A.4 Movie clips of the optical trapping of polystyrene spheres. (a) Before trapping, (b) 5 μm diameter polystyrene sphere was trapped by the laser beam, (c) 5 μm polystyrene sphere escaped from the trap when the fluid flow rate increased due to fluid evaporation.

References

[1] http://www.stanford.edu/group/blocklab/Optical%20Tweezers%20Introduction.htm

[2] A. Ashkin, J. M. Dziedzic, J. E. Bjorkholm and S. Chu, "Observation of a single-beam gradient force optical trap for dielectric particles", *Opt. Lett.*, vol.11, no.5, pp.288-290, 1986.

[3] S. C. Grover, A. G. Skirtach, R.C. Gauthier, and C. P. Grover, "Automated single-cell sorting system based on optical trapping", J. of Biomedical Optics, vol. 6, no.1, pp.14-22, 2001.

[4] Y. Sako, A. Nagafuchi, S. Tsukita, M. Takeichi, and A. Kusumi, "Cytoplasmic regulation of the movement of E-cadherin on the free cell surface as studied by optical tweezers and single particle tracking: Corralling and tethering by the membrane skeleton", *J. of Cell Biology*, vol.140, no.5, pp.1227-1240, 1998.

[5] E. Fallman, S. Schedin, J. Jass, M. Andersson, B.E. Uhlin, and O. Axner, "Optical tweezers based force measurement system for quantitating binding interactions: system design and application for the study of bacterial adhesion", *Biosensors & Bioelectronics*, vol.19, no.11, pp.1429-1437, 2004.

[6] Y. Liu, G. J. Sonek, M. W. Berns, and B. J. Tromberg, "Physiological monitoring of optically trapped cells: Assessing the effects of confinement by 1064-nm laser tweezers using microlfuorometry", *Biophysical J.*, vol. 71, no. 4, pp. 2158-2167, 1996.

[7] R. W. Steubing, S. Cheng, W. H. Wright, Y. Numajiri, and M. W. Berns, "Laser-induced cell-fusion in combination with optical tweezers- the laser cell-fusion trap", *Cytometry*, vol. 12, no. 6, pp. 505-510, 1991.

[8] T. Yamamoto, O. Kurosawa, H. Kabata, N. Shimamoto, and M. Washizu, " Molecular surgery of DNA based on electrostatic micromanipulation", *IEEE Trans. on Industry Applications,* vol. 36, no. 4, pp.1010-1017, 2000.

[9] A. Ashkin "Optical trapping and manipulation of neutral particles using lasers", *Proc. Natl. Acad. Sci. USA*, vol. 94, pp. 4853-4860, May 1997.

[10] A. Ashkin, "Forces of a single-beam gradient laser trap on a dielectric sphere in the ray optics regime", *Biophysical J.,* vol. 61, no.2, pp.569-582, 1992.

[11] W. H. Wright, G. J. Sonek, and M. W. Berns, "Radiation trapping forces on microspheres with optical tweezers", *App. Phys. Lett.*, vol.63, no.6, pp.715-717, 1993.

[12] W. H. Wright, G. J. Sonek, and M. W. Berns, "Parametric study of the forces on microspheres held by optical tweezers", App. *Opt.*, vol. 33, no. 9, pp.1735-1748, 1994.

Appendix B

Dielectrophoretic single cell trapping

As presented in Section 2.5.4, DEP trapping has many advantages of positioning cells, which typically uses stationary traps that can be turned ON or OFF in time. Fundamental theory of DEP forces has been presented in many literatures [1]. This appendix presents the popular electrode geometries with a focus on microwell electrode design and the corresponding fabrication procedures used in this work to trap single cells in the optofluidic cavities. Figure B.1 shows some of the popular electrode geometries for patterning single cells.

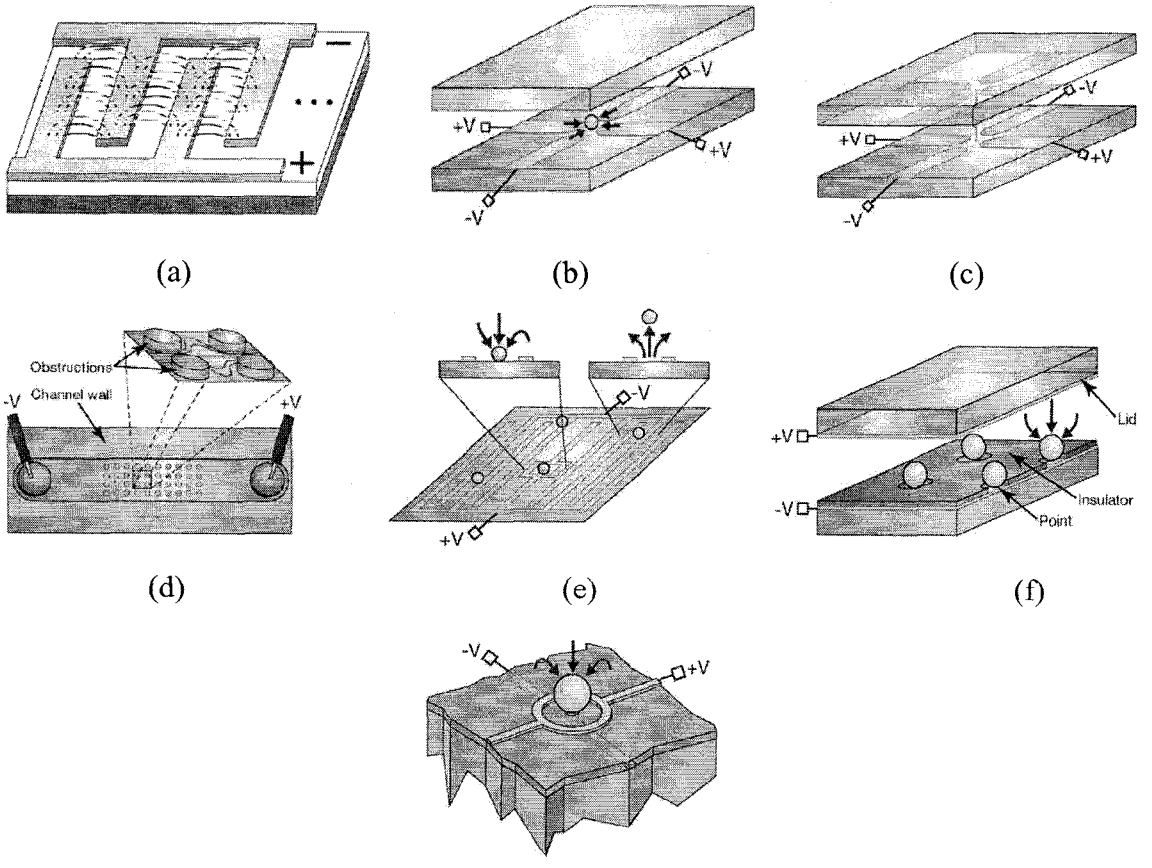

Figure B.1 Schematics of (a) interdigitated electrode geometry, (b) planar quadrupole geometry, showing voltage polarity and trapped cell, (c) opposed octopole geometry, showing the two quadrupoles from which it is constructed. The top quadrupole is excited with opposite polarity from the bottom quadrupole, (d) insulating-post geometry, showing how insulating obstructions create field nonuniformities, (e) DEP microwell, showing how cells are repelled from substrate except inside the trap, where the DEP force points downward, (f) point-lid geometry, and (g) ring-dot geometry.

1) Interdigitated electrodes

Interdigitated electrodes are one of the simplest geometries for patterning cells. Its primary advantages are that they are easy to model and easy to create large arrays. Interdigitated electrodes are useful for patterning many cells where subsequent washes are not necessary. One drawback of this technique is that increasing the field only pushes particles away farther out of the trap and does not necessarily increase confinement since the interdigitated electrode trap is strongest at the voltage just before the cells are levitated.

2) Quadrupole electrodes

Quadrupole electrodes are four electrodes with alternating voltage polarities applied to every other electrode. Both planar and extended quadrupole traps have been developed as shown in Figure B.1 (a) and (b). The first type is easy to fabricate but suffers from the same drawback as the interdigitated electrode and thus is not commonly used for handling cells. The 2nd type, although much more difficult to fabricate than planar quadruples, is orders of magnitude stronger and can successfully hold single cells against significant liquid flows. Extruded quadrupole is most appropriate for observing cells rather than patterning cells because it can position cells above the substrate.

3) Octopole electrodes

Octopole electrodes increase the strength of quadrupole electrode traps by putting another quadrupole on the chamber ceiling to provide further particle confinement. These opposed octopole traps are significantly stronger than planar quadrupoles, and are routinely used for single-cell trapping. Octopole electrodes are much easier to fabricate than the extruded quadruples can be arrayed just like planar quadrupoles. The primary challenge of octopole electrodes is that they require precise alignment of the two opposed quadrupoles, and that limit the overall chamber height because the chamber height must be about the same as the electrode spacing to ensure that the two quadrupoles act in concert; if the chamber height is increased significantly, the fields from the two quadrupoles will not interact and the strength benefits of the octopole will go away.

4) Insulating-post geometry

Insulating-post geometry uses insulating cylindrical posts etched into a channel to create the field obstructions necessary for DEP [2]. By applying a large DC voltage to the device, DEP will dominate and trap particles because DEP is quadratic with electric field, whereas electrokinetic phenomena are linear with electric field. A distinct advantage of this approach is that the channel is completely passive and can be made out of plastic.

5) nDEP microwell

As noted above, the majority of nDEP-based traps are not suitable for cell patterning because they do not position cells against the substrate. This is fundamentally due to the fact that nDEP traps push cells away from electrodes, so if electrodes are on the substrate, they will tend to push the cells off the substrate. To circumvent this, an nDEP trap shown in Figure B.1 (e) was developed by researchers at MIT specifically for patterning single cells. This trap confines cells within the fringing fields of two electrodes. Importantly, the strength of this trap increases with higher voltages and is strong enough to withstand reasonable washes. Additionally, the planar electrode patterns can be created using inexpensive printing technology.

Due to the strong trapping strength and ease in electrode fabrication, nDEP microwell has been used to trap single cells in the optofluidic cavities in this dissertation. The detailed theory of trapping mechanisms of the nDEP microwell was presented in reference [1]. The photomask of the nDEP microwell was designed using commercial software packgage, FREEHAND, and printed onto transparency sheet at Photoplot Store in Colorado Springs.

6) Points-and-lid geometry

Points-and-lid geometry, which traps cells using pDEP, is a useful geometry for patterning cells. This geometry can tolerate exposure to low-conductivity liquids. Although several variations exist, all use a uniform top "lid" conductor, typically thin transparent gold or indium tin oxide (ITO), and a bottom conductor patterned into "points" using some type of insulator as shown in Figure B.1 (f). Importantly, this is one

of the few DEP geometries where researchers have positioned cells and then had them attach; most other geometries have thus far only been used for positioning.

7) Ring-dog geometry

The ring-dot geometry consists of an outer ring electrode and an inner round "dot" electrode on a separate metal layer. Cells are attracted via pDEP to the field maximum at the dot. The distinct advantages of this geometry are that it is planar yet strong and that the number of control electrodes scales as $2\sqrt{n}$, where n is the number of traps. This scaling is improved as compared with standard passive architectures where the number of connections scales linearly with the number of trapping sites [3].

References

[1] J. Voldman, "Electrical forces for microscale cell manipulation", *Annu. Rev. Biomed. Eng.*, vol. 8, pp.425-454, 2006.

[2] B. H. Lapizco-Encinas, B. A. Simmon, E. B. Cummings, et al., "Dielectrophoretic concentration and separation of live and dead bacteria in an array of insulators", *Anal. Chem.*, vol. 76, no. 6, pp. 1571-1579, 2004.

[3] J. Voldman, M. Toner, M. L. Gray, et al., "Design and analysis of extruded quadrupolar dielectrophoretic traps", *J. of Electrostatics*, vol. 57, no. 1, pp. 69-90, 2003.

Appendix C

Paraxial Gaussian Beam Resonator Analysis

This appendix is a MathCAD sheet, which presents calculations of the stability diagram beam profile, and transverse mode spacing of a sphere-loaded optofluidic cavity using classical paraxial Gaussian beam resonator analysis. The results obtained from this shee used as a guidance to the optofluidic cavity design. The author greatly acknowledge the help and guidance provided by Dr. Lear in presenting these calculations.

Numerical calculations were performed on a plane-plane Fabry-Pertor cavity containing single microsphere with uniform refractive index submerged in water as shown in Figur C.1.

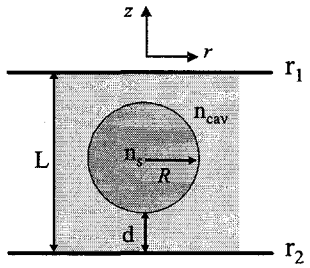

Figure C.1 Schematic diagram of a high refractive index microsphere in a plane-plane resonator cavity. r1 and r2 are end mirror reflection coefficients, R is the radius of the sphere, L and d is the cavity length and the distance between the microsphere and the bottom mirror, respectively. ns and ncav is the refractive index of the microsphere and the fluid respectively.

Section C1 presents cavity stability analysis determined by the magnitude of the trace of the round trip ABCD matrix within the paraxial approximation [A.E. Siegman]. Section presents the calculation of transverse mode profile. The results obtained from this sectic can be used to check the accuracy of the paraxial approximation, which requires the bea waist is much bigger than the wavelength [G. Q. Zhou]. Section C3 presents the transve mode spacing calculated from the Guoy phase shift.

C.1 Cavity stability diagram

The stability of an optical resonator can be determined by the magnitude of the trace of round trip ABCD matrix within the paraxial approximation [1].

Refractive index of the sphere and the fluid: $n_s := 1.59$ $n_{cav} := 1.33$

Radius of the microsphere: $R := 5\ \mu m$

In order to find the round-trip ABCD matrix of a sphere-loaded cavity, we divide an OFIS cavity into 3 sections with theABCD matrix of each section being calculated strai; forwardly. Here, we treated the sphere as a ball lens,

1) ABCD matrix of a ball lens: $M_{ball}(R,n_s) := \begin{pmatrix} 1 & 0 \\ \frac{n_s - n_{cav}}{-R} & 1 \end{pmatrix} \begin{pmatrix} 1 & \frac{2\cdot R}{n_s} \\ 0 & 1 \end{pmatrix} \cdot \begin{pmatrix} 1 & 0 \\ \frac{n_{cav} - n_s}{R} & 1 \end{pmatrix}$

$$M_{ball} = \frac{1}{n_L} \cdot \begin{bmatrix} 2\cdot n_{cav} - n_s & 2\cdot R \\ \frac{2\cdot (n_{cav} - n_s)\cdot n_c}{R} & 2\cdot n_{cav} - n_s \end{bmatrix}$$

In order to make the calculation application to the general cases, define a normalized sphere position $\rho = \frac{d}{(L - 2R)}$

2) ABCD matrix for free space propagation from the bottom mirror to the vertex of the ball lens: $M_1(\rho,L,R) := \begin{bmatrix} 1 & \frac{\rho\cdot (L - 2\cdot R)}{n_{cav}} \\ 0 & 1 \end{bmatrix}$

3) ABCD matrix for free space propagation on the other side of the ball lens to the other mirror: $M_2(\rho,L,R) := \begin{bmatrix} 1 & \frac{(1-\rho)\cdot (L - 2\cdot R)}{n_{cav}} \\ 0 & 1 \end{bmatrix}$

The round-trip ABCD matrix can be derived by multiplying the above 3 matrices:

$$M_{RT}(\rho,L,R,n_s) := M_1(\rho,L,R)\cdot M_{ball}(R,n_s)\cdot M_2(\rho,L,R)^2\cdot M_{ball}(R,n_s)\cdot M_1(\rho,L,R)$$

The matrix element of the round-trip matrix is calculated as the following way as the nan of this method indicates and will be used in further derivation of the stability diagram.

$$A(\rho,L,R,n_s) := M_{RT}(\rho,L,R,n_s)_{0,0} \qquad B(\rho,L,R,n_s) := M_{RT}(\rho,L,R,n_s)_{0,1}$$

$$C(\rho,L,R,n_s) := M_{RT}(\rho,L,R,n_s)_{1,0} \qquad D(\rho,L,R,n_s) := M_{RT}(\rho,L,R,n_s)_{1,1}$$

From refrence [1], the stability of an optical resonator can be found by parameter m_{RT}, which is trace of $M_{RT}(\rho,L)$

$$m_{RT}(\rho,L,R,n_s) := \frac{A(\rho,L,R,n_s) + D(\rho,L,R,n_s)}{2}$$

For stable operation, the absolute value of m_{RT} should be less than one. Therefore, we need to solve the following equations:

$\rho := 0, 0.005 .. 1$

$stability1(\rho,L,R,n_s) := m_{RT}(\rho,L,R,n_s) - 1$ and $stability2(\rho,L,R,n_s) := m_{RT}(\rho,L,R,n_s) + 1$

Solving the above equations, we have

$\text{stability1a}(\rho) := \text{root}(\text{stability1}(\rho, L, R, 1.59), L, 0.001, 120)$

$\text{stability2a}(\rho) := \text{root}(\text{stability2}(\rho, L, R, 1.59), L, 0.001, 30.4)$

$\text{stability2b}(\rho) := \text{root}(\text{stability2}(\rho, L, R, 1.59), L, 30.4, 120)$

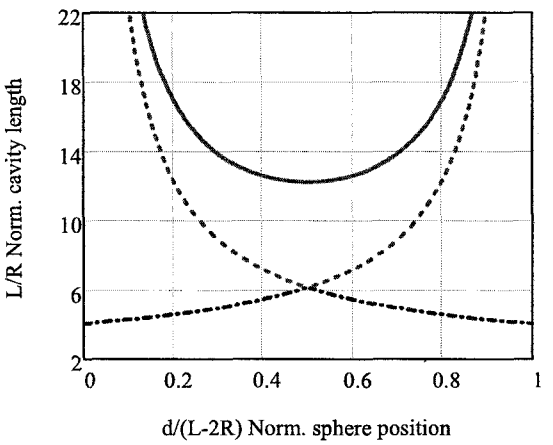

Figure C2. Stability diagram of a polystyrene sphere inside a planar-planar Fabry-Perot cavity.

Plot L/R vs. sphere refractive index for the unconditional stable cases r=0 or 1

$n_{s1} := 1.33, 1.34 .. 1.60 \qquad R_1 := 5$

$\text{ST1}(\rho_1, L_1, R_1, n_{s1}) := m_{RT}(\rho_1, L_1, R_1, n_{s1}) - 1 \qquad \text{ST2}(\rho_1, L_1, R_1, n_{s1}) := m_{RT}(\rho_1, L_1, R_1, n_{s1}) + 1$

The solutions to the above equations are:

$$\text{ST1a}(n_{s1}, \rho_1) := \text{root}(\text{ST1}(\rho_1, L_1, R_1, n_{s1}), L_1, 10, 100)$$
$$\text{ST2a}(n_{s1}, \rho_1) := \text{root}(\text{ST2}(\rho_1, L_1, R_1, n_{s1}), L_1, 10, 200)$$

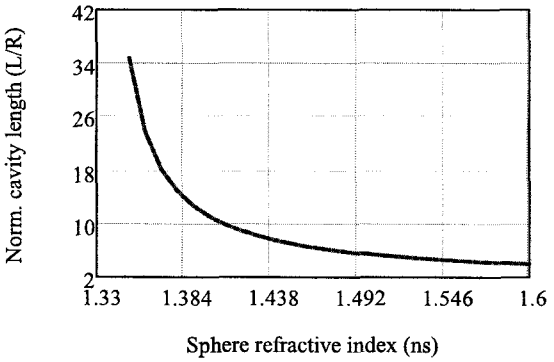

Figure C3. Normalized cavity length vs. sphere refractive index for the unconditionally stable cases.

C.2 Beam profile calulation

The maximum beam radius inside the cavity is calculated to confirm the stability calculat since the maximum beam radius should be well confined within the microsphere. In oth words, the maximum beam radius should be smaller than the sphere radius.

In the case of a sphere-loaded FP cavity, the maximum beam radius always occurs at tge ball vertice that is closer to the planar mirror and can be computed from the beam waist using

$$\omega(z) = \omega_0 \cdot \sqrt{1 + \left(\frac{z}{z_R}\right)^2} = \omega_0 \cdot \sqrt{1 + \left(\frac{z \cdot \lambda}{\pi \cdot \omega_0^2}\right)^2}$$ <------- Siegman p.664 (5)

where ω_0 is the beam waist size, z is the distance from the beam waist, and z_R is the Rayleigh range. For stable operation, the beam waist should be at the planar mirror. According to Siegman that Gaussian beam waist is related to the round trip ABCD matrix as indicated in the following formula,

$$\frac{1}{q} = \frac{D-A}{2B} - \frac{1}{B} \cdot \sqrt{\left(\frac{A+D}{2}\right)^2 - 1} = \frac{1}{R} - j \cdot \frac{\lambda}{\pi \cdot \omega^2}$$ <--------- Siegman p. 816 (reference plane dependent)

$$\frac{-1}{B} \cdot \sqrt{m_{RT}^2 - 1} = -j \cdot \frac{\lambda}{\pi \cdot \omega_0^2}$$ <---------- Siegman p.817-(4)

where m_{RT} is the round trip ABCD matrix starting from the reference planar

$$\omega_0(\rho, L, R, n_s, \lambda) := \sqrt{\left|\frac{i \cdot B(\rho, L, R, n_s) \cdot \lambda}{\pi \cdot n_{cav} \cdot \sqrt{m_{RT}(\rho, L, R, n_s)^2 - 1}}\right|}$$ <--------- Siegman p.820-(15)

For our case, the maximum beam radius occurs at the bottom vertice of the ball if r<0.5, we have

$$\omega_{BallEdge}(\rho, L, R, n_s, \lambda) := \omega_0(\rho, L, R, n_s, \lambda) \sqrt{1 + \left[\frac{\rho \cdot (L - 2 \cdot R)}{\frac{\pi \cdot \omega_0(\rho, L, R, n_s, \lambda)^2}{\frac{\lambda}{n_{cav}}}}\right]^2}$$

For ρ>0.5, the maximum beam radius occurs at the top vertice of the ball, which can be readily calculated using the above formula by replacing r with 1-r. Comning these two ca the maximum beam radius for the overall cavity is:

$$\omega_{max}(\rho, L, R, n_s, \lambda) := \begin{cases} \omega_{BallEdge}(\rho, L, R, n_s, \lambda) & \text{if } \left|m_{RT}(\rho, L, R, n_s)\right| \le 1 \wedge 0 \le \rho < 0.5 \\ \omega_{BallEdge}(1 - \rho, L, R, n_s, \lambda) & \text{if } \left|m_{RT}(1 - \rho, L, R, n_s)\right| \le 1 \wedge 0.5 \le \rho \le 1 \\ -1 \text{ otherwise} \end{cases}$$

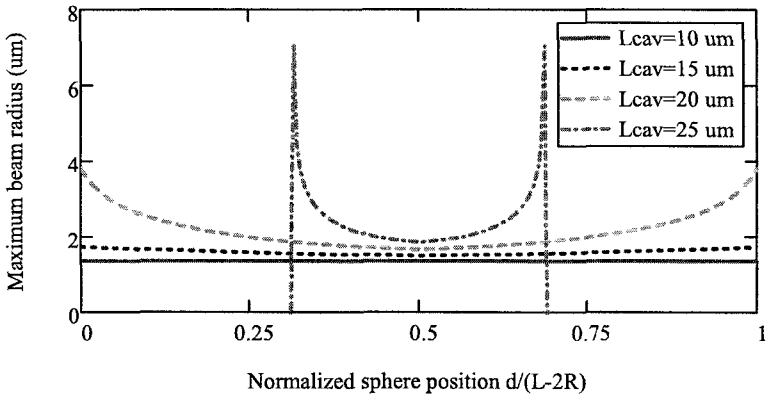

Figure C.4 Maximum beam radius vs. normalized sphere position for 10 μm diameter polystyrene sphere loaded planar-planar Fabry-Peort cavities with different cavity lengths.

In order generate the contour plot of the maximum beam radius as a function of cavity length and the normalized sphere position, we need to put r and L matrix format,

$maxindex := 200$ $\quad mm := 0..maxindex$ $\quad nn := 0..maxindex$

$$pos_{mm} := \frac{mm}{maxindex} \qquad LL_{nn} := 10 + \frac{nn}{maxindex} \cdot (120 - 10)$$

$$\omega_{mm,nn} := \omega_{max}(pos_{mm}, LL_{nn}, 5, 1.59, 0.89)$$

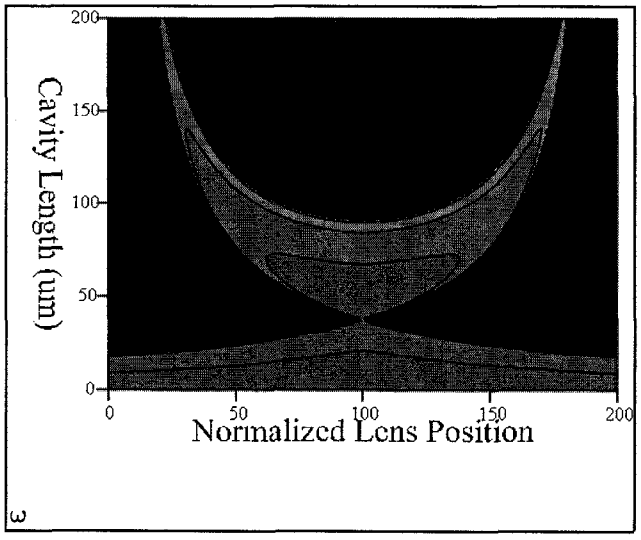

<---------- In order for this figure to show up properly, you need to open the MathCAD sheet using MathoCAD 14.

Figure C.5 Maximum beam radius contour plot as a function of normalized sphere position and the cavity length for a 10 μm diameter polystyrene sphere inside a planar-planar Fabry-Peort cavity.

C.3 Transverse mode spacing vs. Guoy phase shift

Transverse mode spacing is calculated from the Gouy phase shift when the beam passin through the OFIS cavity according to a formula given in reference [1]. Gouy phase is defined as the phase shift occurring in the propagation of a Gaussian beam. Along its propagation direction, a Gaussian beam acquires a phase shift, which somewhat differs from that for a plane wave with the same optical frequency. This difference is called the Gouy phase shift.

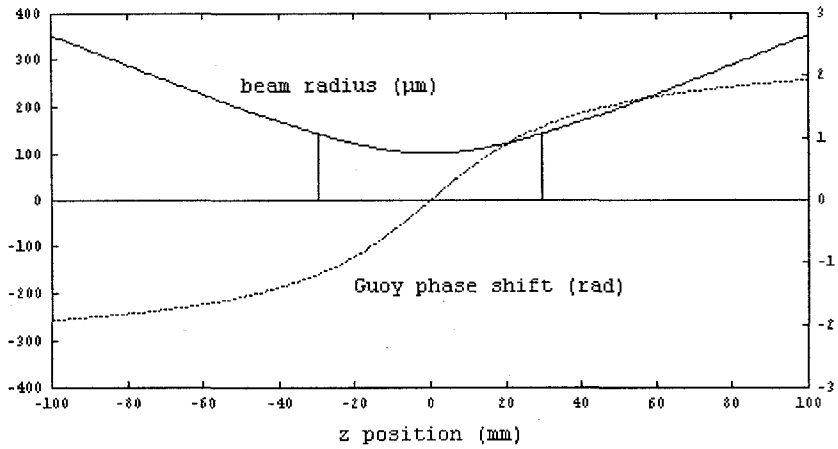

Figure C.4 Beam radius and Gouy phase shift along the propagation direction for a beam in air with 1064 nm wavelength and 100 mm radius at the waist. The positions at plus and minus the Rayleigh length are marked.

$$j := \sqrt{-1} \qquad \lambda_0 := 890\ \text{nm} \qquad \frac{1}{q} = \frac{D-A}{2\cdot B} - \frac{j}{B}\cdot\sqrt{1-\left(\frac{A+D}{2}\right)^2} \qquad \text{(Siegman P.816)}$$

$$q_a(\rho,L,R,n_s) := \left[\frac{D(\rho,L,R,n_s)-A(\rho,L,R,n_s)}{2\cdot B(\rho,L,R,n_s)} - \frac{j}{B(\rho,L,R,n_s)}\cdot\sqrt{1-\left(\frac{A(\rho,L,R,n_s)+D(\rho,L,R,n_s)}{2}\right.}\right.$$

According to Siegman's book, Guoy phase shift of the (n,m) order transverse mode is

$$\frac{A+\frac{B}{q_1}}{\left|A+\frac{B}{q_1}\right|} = \exp(j\cdot\psi_1) \qquad \text{<------ Siegman pp.785 (26)}$$

$$\frac{\alpha_{2,nm}}{\alpha_{1,nm}} = \left(\frac{1}{A+\frac{B}{q_{a,b}}}\right)^{n+m+1} \qquad \text{<------ Siegman pp.836 (30)}$$

Therefore Guoy phase shift of the first high order transverse modes w.r.t. the fundamenta

mode is

$$\phi_{guoy}(\rho,L,R,n_s) := \begin{cases} \arg\left[\left(A(\rho,L,R,n_s) + \frac{B(\rho,L,R,n_s)}{q_a(\rho,L,R,n_s)}\right)^{-1}\right] & \text{if } \left|m_{RT}(\rho,L,R,n_s)\right| \le 1 \\ 0 \quad \text{otherwise} \end{cases}$$

Therefore, the corresponding transverse mode frequency shift [2] is

$$\Delta\nu(\rho,L,R,n_s) := \frac{\phi_{guoy}(\rho,L,R,n_s)}{\pi} \cdot \frac{3\cdot 10^8}{2\cdot\left[n_s\cdot 2R + n_{cav}\cdot(L-2R)\right]\cdot 10^{-6}} \cdot 10^{-12} \quad \text{in THz}$$

Express the above result in wavelength form: $\Delta\lambda = \lambda_2 - \lambda_1 = \frac{c}{\upsilon_2} - \frac{c}{\upsilon_1} = \frac{c\cdot\Delta\upsilon}{\upsilon_1\cdot\upsilon_2} = \Delta\upsilon\cdot\frac{\lambda^2}{c}$

$$\Delta\lambda(\rho,L,R,n_s) := \Delta\nu(\rho,L,R,n_s)\cdot 10^{12}\cdot\frac{\left(0.89\cdot 10^{-6}\right)^2}{3\cdot 10^8}\,10^9 \quad \text{in nm}$$

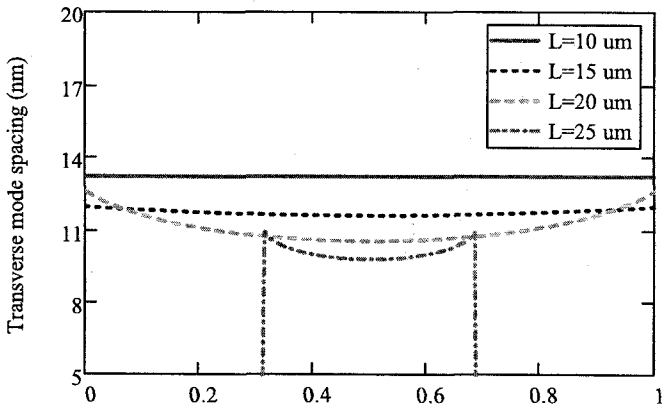

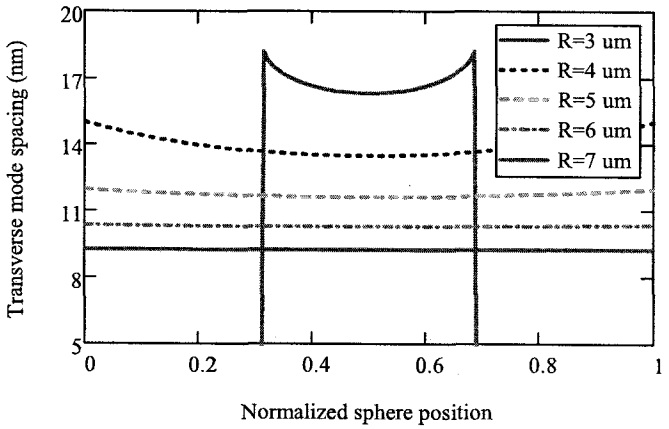

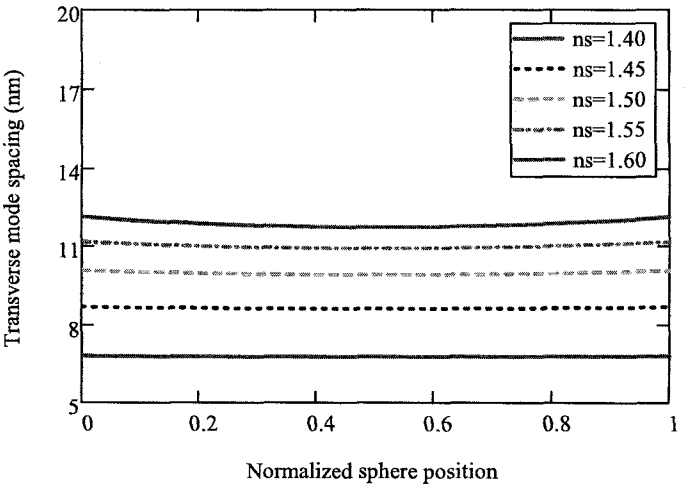

Figure C.5 Transverse mode spacing as a function of normalized sphere position for a 10 μm diameter polystyrene sphere inside a planar-planar Fabry-Perot cavity.

The following calculations were done for a 5 μm diameter polystyrene sphere loaded 10 μm deep microfluidic FP cavity, which was cited by the model comparison section of the dissertation.

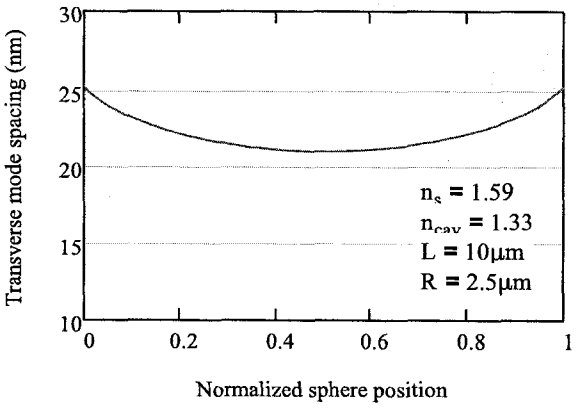

Figure C.6 (same as Figure 6.21 (a) in the dissertation) Transverse mode spacing calculated using the paraxial Gaussian BMP for a 5 μm diameter polystyrene sphere loaded 10 μm deep FP cavity.

The absolute wavelength of transverse modes can be calculated from

$$\lambda_{00}(\rho, L, R, n_s, q) := \frac{2\left[n_s \cdot 2R + n_{cav} \cdot (L - 2R)\right]}{q - \frac{\phi_{guoy}(\rho, L, R, n_s)}{(2\pi)}} \cdot 10^3 \quad \text{in nm}$$

The wavelength of the 01 order transverse mode can be calculated by substracting the

mode spacing calculated from the Guoy phase shift is

$$\lambda_{01}(\rho,L,R,n_s,q) = \lambda_{00}(\rho,L,R,n_s,q) - \Delta\lambda(\rho,L,R,n_s)$$

$$\lambda_{01}(\rho,L,R,n_s,q) := \lambda_{00}(\rho,L,R,n_s,q) - \Delta\nu(\rho,L,R,n_s)\cdot 10^{12}\cdot\frac{\left(\lambda_{00}(\rho,L,R,n_s,q)\cdot 10^{-9}\right)^2}{3\cdot 10^8}\,10^9$$

Define the longitudinal mode order q as $q := 30,31..36$

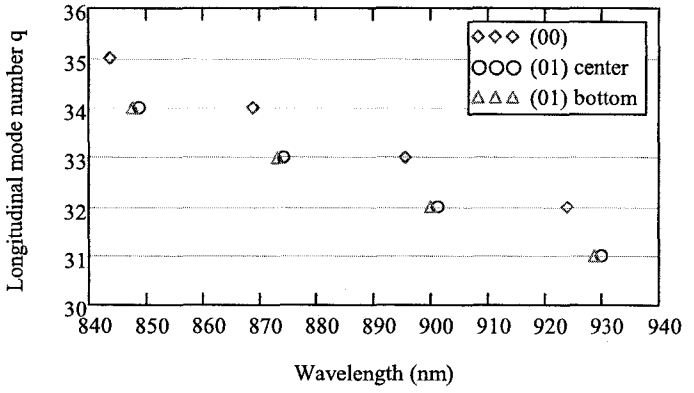

Figure C.7 Wavelength of transverse modes calculated from the Guoy phase shift. The fundamental mode wavelength is not affected by the sphere position.

C.4 High order transverse mode excitation and matching

Higher order transverse modes have larger diffraction angle and can be excited more effectively with tilt excitation than the fundamental modes. Nemerical aperture of transv modes at the bottom mirror can be calculated from the geometric ray tracing. Beam divergence angle is

$$\theta = \frac{\omega_0}{z_R} = \frac{\omega_0}{\frac{\pi\cdot\omega_0^2}{\lambda}} = \frac{\lambda}{\pi\cdot\omega_0} \qquad \omega(z) = \omega_0\cdot\sqrt{1+\left(\frac{z}{z_R}\right)^2} = \omega_0\cdot\frac{z}{z_R}$$

The numerical aperture of the fundamental mdoes can then be calculated as shown below

$$NA(\rho,L,\lambda) := \begin{cases} \sin\left(\dfrac{\lambda}{\omega_0(\rho,L,R,n_s,\lambda)\cdot\pi}\right) & \text{if } \left|m_{RT}(\rho,L,R,n_s)\right| \le 1 \\ 0 \quad \text{otherwise} \end{cases}$$

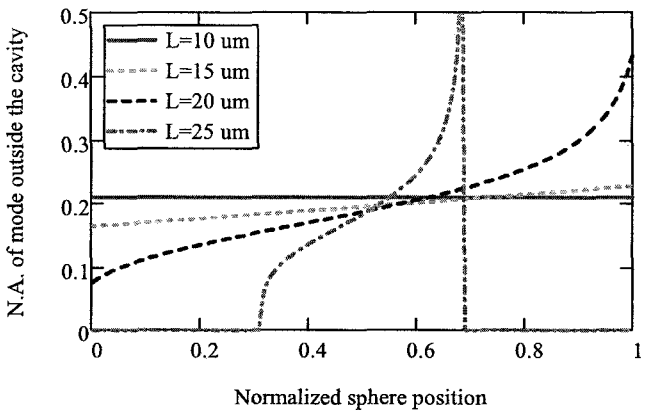

Figure C.8 Numerical aperture of the fundamental mode as a function of the normalized sphere position.

Divergence angle of confined modes inside the cavity

$$\theta_2(\rho,L,\lambda) := \operatorname{atan}\left[\frac{\omega_{max}(\rho,L,R,n_s,\lambda) - \omega_0(\rho,L,R,n_s,\lambda)}{\rho \cdot (L - 2 \cdot R)}\right]$$

$$NA2(\rho,L,\lambda) := \begin{cases} \sin(\theta_2(\rho,L,\lambda)) & \text{if } |m_{RT}(\rho,L,R,n_s)| \le 1 \\ 0 & \text{otherwise} \end{cases}$$

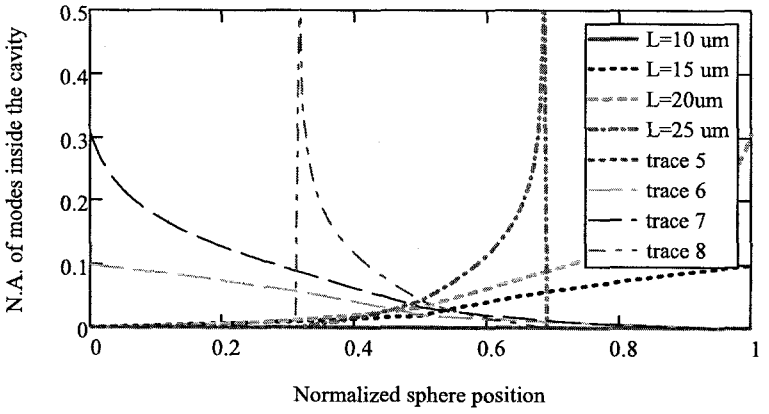

Figure C.9 Divergence angle of the fundamental modes within the microfluidic cavity.

References

[1] A. E. Siegman, "Lasers", Mill Valley, CA: University Science, 1986.
[2] G. Machavariani, N. Davidson, A.A. Ishaaya, A.A. Friesem, "Improving the stability of longitudinal and transverse laser modes", *Optics Communications*, vol. 239, pp.147, 2004.

Appendix D

WKB method and optical waveguides

This appendix provides the numerical algorithm to calculate optical modes in graded-ind (GRIN) waveguides under the Wentzel, Kramers, and Brillouin (WKB) approximations. this dissertation, transmission spectra of microsphere/cell loaded Fabry-Perot (FP) cavity were calculated using this algorithn once the effective index profile of the cavity was calculated from Hadley's effective index model.

Example: a 15 μm diameter polystyrene sphere-loaded 16 μm deep microfluidic FP cavi with cavity configurations described below:

$L_{cav} := 16 \cdot 10^3$ nm $\qquad R := 7.5 \cdot 10^3$ nm

$n_{cav} := 1.33$ $\qquad n_{max} := 1.57375$ calculated from Hadley's model

The effective index profile of the cavity calculated from Hadley's effective index model i

$$n(r) := \begin{cases} n_{cav} + (n_{max} - n_{cav}) \cdot \sqrt{1 - \frac{r^2}{R^2}} & \text{if } |r| \le R \\ n_{cav} & \text{if } |r| > R \end{cases}$$

The WKB method has found good approximate solutions can be derived in the case of a slowly varying index profile. It involves keeping the form of the uniform-medium wave equation, but using a plane wave k-vector that can vary transversely. The wave equation i the cylindrical coordinates for azimuthal order ν is

$$\frac{d^2}{dr^2}U(r) + \frac{1}{r}\frac{d}{dr}U(r) + \left[k_0^2 n^2(r) - \beta^2 - \frac{\nu^2}{r^2}\right]U(r) = 0$$

Under the assumptions of uniform waveguide along the z-direction and slowly varying ra index, e.g. neglecting any backscaterring, the equation can be integrated to give ,

$$\int_{r_1}^{r_2} \sqrt{k_0^2 n^2(r) - k_0^2 n_{eff}^2 - \frac{\nu^2}{r^2}}\, dr = (m + \frac{1}{2})\pi$$

where the boundary conditions require that the accumulated phase change is an odd integ multiple of π/2, and m is the radial mode order, and neff is the effective refractive index the mode.

The bove phase condition for confined modes is an implicit function of neff and needs to solved numerically for most of the index profiles except for several special cases, for example, the parabolic index profile, where analytical solutions exist. The following cod are written for solving the above implicit equation directlly, which requires lots of compu

resources.

$$f(n_{eff}, \lambda_0, m, \nu) := \left(m + \frac{1}{2}\right)\cdot\pi - \int_{-2R}^{2R} \left[\left(\frac{2\pi}{\lambda_0}\right)^2 \cdot n(r)^2 - \left(\frac{2\pi}{\lambda_0}\right)^2 \cdot n_{eff}^2 - \frac{\nu^2}{r^2}\right]^{0.5} dr$$

$$f_{00}(\lambda_0) := root(f(n_{eff}, \lambda_0, 0, 0), n_{eff}, 1.55, 1.6) \qquad f_{10}(\lambda_0) := root(f(n_{eff}, \lambda_0, 1, 0), n_{eff}, 1.40, 1.6)$$

$$f_{01}(\lambda_0) := root(f(n_{eff}, \lambda_0, 0, 1), n_{eff}, 1.40, 1.6) \qquad f_{11}(\lambda_0) := root(f(n_{eff}, \lambda_0, 1, 1), n_{eff}, 1.40, 1.6)$$

$$f_{02}(\lambda_0) := root(f(n_{eff}, \lambda_0, 0, 2), n_{eff}, 1.40, 1.6) \qquad f_{20}(\lambda_0) := root(f(n_{eff}, \lambda_0, 2, 0), n_{eff}, 1.40, 1.6)$$

Note: The bove root finding procedure may take ~10 minutes!

Note that the above root solving code requires a small range for neff in order for the computer to find the correct values. Multiple root solving equations need to be used to calculate the complete set of effective indices of all supported modes. To simplify the computation, a parabolic profile could be used as described below,

$$n_{clad} := n_{cav} \qquad \Delta := \frac{n_{max}^2 - n_{clad}^2}{2\cdot n_{max}^2} \qquad \Delta = 0.143 \qquad k_0(\lambda) := \frac{2\pi}{\lambda}$$

The above value is much larger than the normal range 1~2% for graded index fiber. Therefore, the WKB method is not suitable for our case. The calculation results are quite different from those of more accurate methods such as the finite difference method.

$$n_{WKB}(r, g) := \begin{cases} n_{max}\cdot\left[1 - 2\cdot\Delta\cdot\left[\left(\frac{|r|}{R}\right)^g\right]\right]^{0.5} & \text{if } |r| \le R \\ n_{cav} & \text{if } |r| > R \end{cases}$$

conventional GRIN fiber profile used in WKB

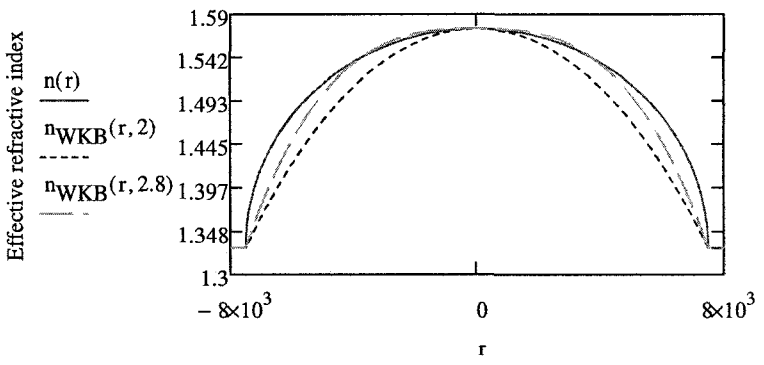

Figure D.1 effective index profiles of the sphere-loaded microfluidic FP cavity.

Treating the effective cavity index profile as a parabolic graded-index fiber profile, the

calculation of higher order transverse modes can be easily calculated from the analytical solution presented below,

$$n_{eff1}(m,\nu,\lambda) := n_{max}\left[1 - \frac{2\cdot(2\Delta)^{0.5}}{n_{max}\cdot k_0(\lambda)\cdot R}\cdot(|\nu| + 2\cdot m + 1)\right]^{0.5}$$

where m is the radial mode order and ν is the azimuthal mode order. For the resonant mo of the overall cavity, the longitudinal resonant mode condition needs to be applied as sho

$$n_{FP}(q,\lambda) := \frac{q\cdot\lambda}{2\cdot L_{cav}}$$

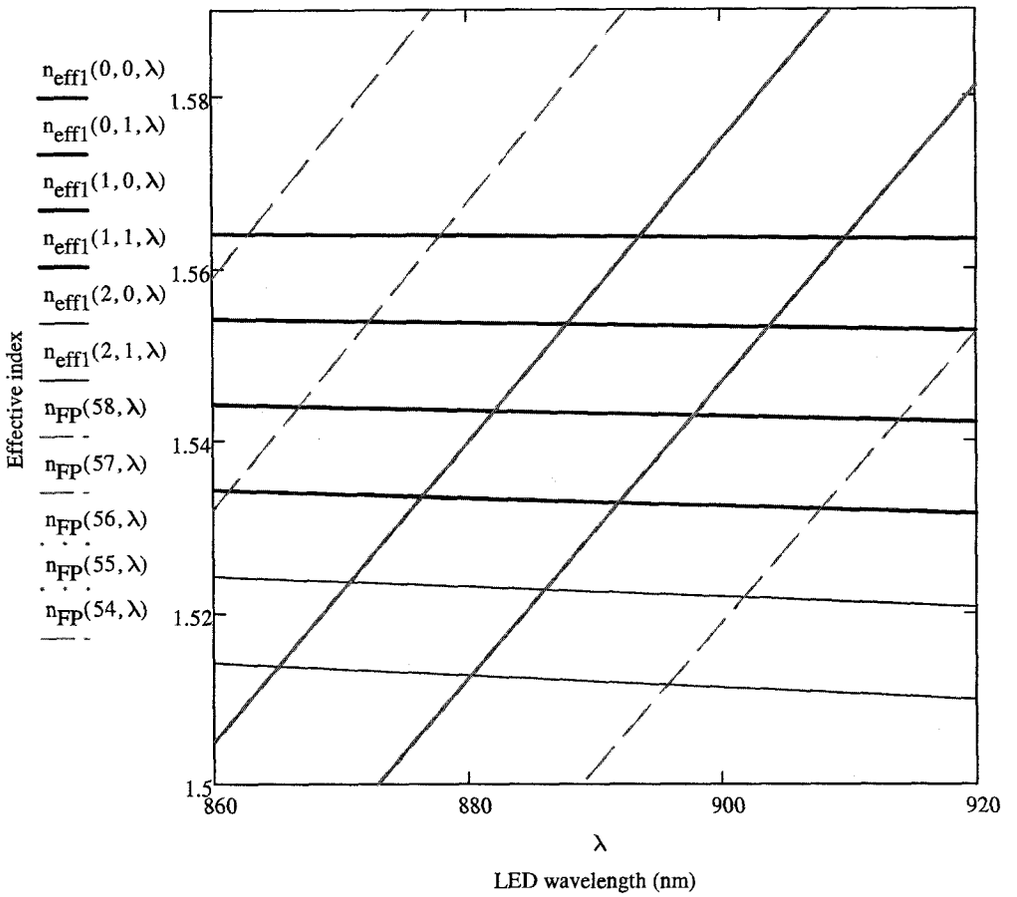

Figure D.2 Effective indice of resonant modes of the sphere-loaded microfluidic FP cavity. The dashed lines corresponds to the longitudinal resonant condition.

Appendix E

Effective index model and finite difference mode solver

1. Derive effective index model using Hadley's method
2. Solve for fundamental modes using cylindrical FD mode solver written by Dr. Lear
3. Applying the longitudinal mode resonant condition to find l of fundamental mode
4. Vary the size of the ball, plot D as function of sphere size

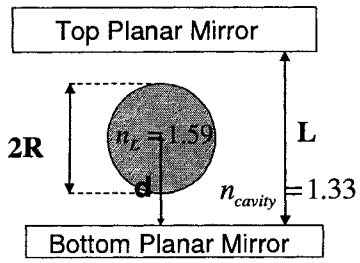

Figure E.1 Schematic of a sphere-loaded microfluidic FP cavity.

$L_{cav} := 10\ \mu m$ $R := 2.5\ \mu m$ $n_{cav} := 1.33$ $n_{ball} := 1.43$

E. 1 Transfer matrix method for multilayer waveguide

Using trnasfer matrix method to calculate the resonance frequency of the FP cavity (longitudinal mode frequency). In this part, we perform the simualtion on the case where the microsphere is centered inside the cavity.

Now we consider the 2-D case (in X-Z plane) and at postion x>0, the cavity contains 3 regions and 2 end reflectors, which are described in sequence from top to bottom as follows:

(1) propagates through top high reflective mirror (DBR or hard mirror)

(2) propagation through the fluid for distance:

$$d_1(r) := \frac{L_{cav}}{2} - \sqrt{R^2 - r^2} \qquad n_1(r) := n_{cav}$$

(3) propagation through the microsphere for distance:

$$d_2(r) := 2\cdot\sqrt{R^2 - r^2} \qquad n_2(r) := n_{ball}$$

(4) propagation through the fluid for distance:

$$d_3(r) := \frac{L_{cav}}{2} - \sqrt{R^2 - r^2} \qquad n_3(x) := n_{cav}$$

(5) propagtes through bottom high reflectivity mirror (DBR or hard mirror)

Here, we need to consider the reflectivity at the interface of the ball and liquid and using transfer matrix method to get the resonant frequency at each part of the cavity. (For the c: of the ball centered in the FP cavity)

We need to calculate the transfer matrix of each region separately and then multiply them sequency in order to get the resonant conditions. (see ref. EE773-HW#3 and Coldren's book). I'm lazy here to only consider the effective cavity length change, therefore the solution is independent on the sphere position within the fluidic cavity.

Guided modes of multiayer waveguides: assuming the top and bottom mirrors are hard mirrors with reflectivities r1 and r2 respectively. Now apply the transverse resonance technique to obtain

For the simple case of lossless cavity, we have

$i := 20, 21 .. 70$

$$\lambda(i,r) := \begin{cases} \dfrac{2\cdot\left(n_1(|r|)\cdot d_1(|r|) + n_2(|r|)\cdot d_2(|r|) + n_3(|r|)\cdot d_3(|r|)\right)}{i} & \text{if } |r| \le R \wedge 20 < i < 70 \\ \dfrac{2\cdot n_{cav}\cdot L_{cav}}{i} & \text{if } |r| > R \wedge 20 < i < 70 \\ 0 \text{ otherwise} \end{cases}$$

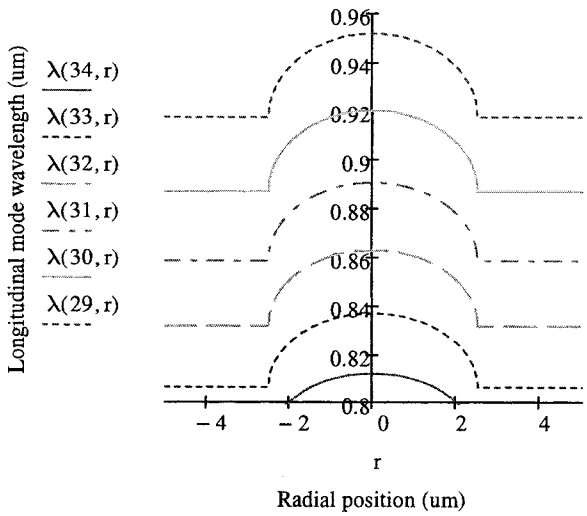

Figure E.2 Longitudinal mode wavelength vs. radial position for different mode orders.

$\Delta r := 10^{-?}\,\mu m$ $\quad n_{eff0} := n_{cav}$ (another possiblity can be obtained from TFCalc)

$$\Delta\lambda(i,r) := \lambda(i,r) - \frac{2 \cdot n_{cav} \cdot L_{cav}}{i} \quad \mu m$$

$$\Delta n_{eff}(i,r) := n_{eff0} \cdot \frac{\Delta\lambda(i,r)}{\lambda(i,10)} \quad \text{from Hardley's paper}$$

$$n_{eff}(i,r) := \begin{cases} n_{eff0} & \text{if } |r| > R \wedge 30 < i < 60 \\ n_{eff0} + \Delta n_{eff}(i,r) & \text{if } |r| \le R \wedge 30 < i < 60 \\ 0 & \text{otherwise} \end{cases}$$

$$n_{cav1}(r) := n_{eff}(50,r)$$

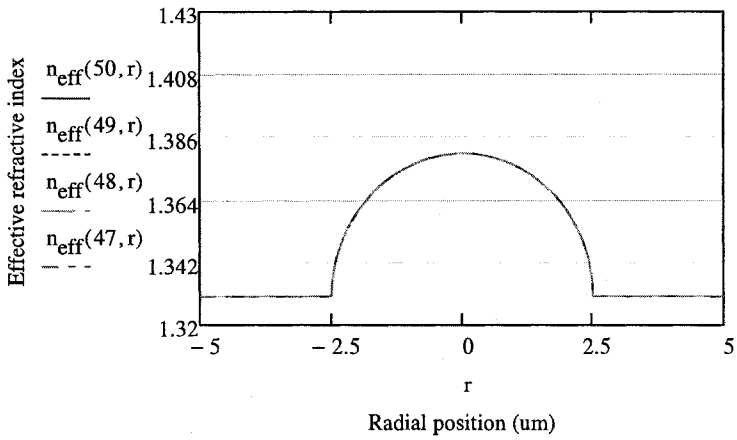

Figure E.3 Effective refractive index profile of the sphere-loaded microfluidic FP cavity calculated from Hadley's effective index model.

Method II. conventional effective index method

$$d_{ball}(r) := (|r| < R) \cdot 2R \cdot \sqrt{1 - \left(\frac{r}{R}\right)^2}$$

$$n_{cav2}(r) := \begin{cases} \dfrac{n_{ball} \cdot d_{ball}(r) + 1.33 \cdot \left(L_{cav} - d_{ball}(r)\right)}{L_{cav}} & \text{if } |r| \le R \\ 1.33 & \text{otherwise} \end{cases}$$

This is the same result as that using the transfer matrix method.

$$\varepsilon(r) := n_{cav2}(r)^2$$

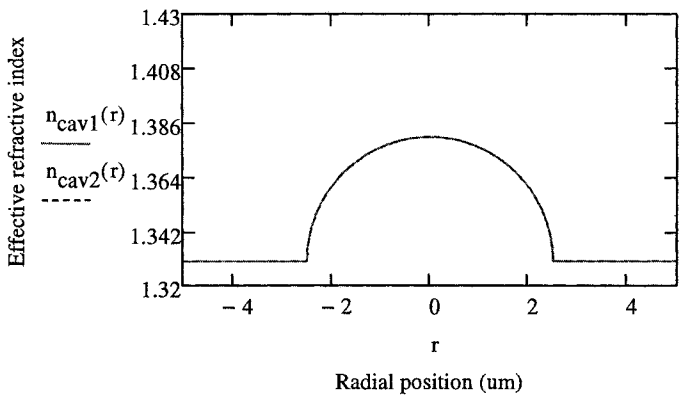

Figure E.4 Effective refractive index profile of the sphere-loaded microfluidic FP cavity calculated from conventional multilayer waveguide thoery.

E.2 Finite-difference numerical mode solver by Linda

$\lambda_0 := 0.85\ \mu m$ $\quad k_0(\lambda_0) := \frac{2\cdot\pi}{\lambda_0}$

$r\_min := -10\ \mu m$ $\quad r\_max := 10\ \mu m$ $\quad i\_max := 1001$

$\Delta r := \frac{r\_max - r\_min}{i\_max}$ $\quad \Delta r = 0.02\ \mu m$ (should choose i_max to prevent meeting r=0 point since r is in the denominator of Mjj's coefficient)

Vectorial wave equation: $\nabla^2 E + \nabla(\frac{\nabla \varepsilon_r}{\varepsilon_r}\cdot E) + k_0^2 \varepsilon_r E = 0$ ----------(1)

Assume the transverse component of the linearly polarized electric field of the LP modes

$E_t(r,\phi,z) = V(r)\, e^{i\cdot l\cdot\phi}\cdot e^{i\cdot(\omega\cdot t-\beta\cdot z)}$

Eq.(1) can be written as:

$$\frac{d^2}{dr^2}V(r) + \frac{1}{r}\cdot\frac{d}{dr}V(r) + \frac{d}{dr}\left[\frac{1}{\varepsilon(r)}\cdot\left(\frac{d}{dr}\varepsilon(r)\cdot V(r)\right)\right] + \left(k_0{}^2\cdot\varepsilon(r) - \beta^2 - \frac{l^2}{r^2}\right)\cdot V(r) = 0 \quad \text{----------(2)}$$

Now we can write the above equation in finite difference form

$$\left(\frac{d}{dr}V(r)\right)_i = \frac{V_{i+1} - V_{i-1}}{2\cdot\Delta r}$$

$$\left(\frac{d^2}{dr^2}V(r)\right)_i = \frac{V_{i+1} - 2\cdot V_i + V_{i-1}}{\Delta r^2}$$

$$\left[\frac{d}{dr}\left[\frac{1}{\varepsilon(r)}\cdot\left[\frac{d}{dr}(\varepsilon(r)\cdot V(r))\right]\right]\right]_i = \frac{1}{\Delta r^2}\cdot\left[\left(\frac{\varepsilon_{i+1}-\varepsilon_i}{\varepsilon_{i+1}+\varepsilon_i}\right)\cdot\left(V_{i+1}-V_i\right)-\left(\frac{\varepsilon_i-\varepsilon_{i-1}}{\varepsilon_i+\varepsilon_{i-1}}\right)\cdot\left(V_i-V_{i-1}\right)\right]$$

$$\frac{V_{i+1}-2\cdot V_i+V_{i-1}}{\Delta r^2}+\frac{V_{i+1}-V_{i-1}}{2\cdot r_i\cdot\Delta r}+\frac{1}{\Delta r^2}\cdot\left[\left(\frac{\varepsilon_{i+1}-\varepsilon_i}{\varepsilon_{i+1}+\varepsilon_i}\right)\cdot V_{i+1}-\left(\frac{\varepsilon_{i+1}-\varepsilon_i}{\varepsilon_{i+1}+\varepsilon_i}+\frac{\varepsilon_i-\varepsilon_{i-1}}{\varepsilon_i+\varepsilon_{i-1}}\right)\cdot V_i-\left(\frac{\varepsilon_i-\varepsilon_i}{\varepsilon_i+\varepsilon_i}\right.\right.$$

V_{i-1} term:

$$\begin{cases}\dfrac{1}{\Delta r^2}-\dfrac{1}{2\cdot r_i\cdot\Delta r}-\dfrac{1}{\Delta r^2}\cdot\dfrac{\varepsilon(r_i)-\varepsilon(r_{i-1})}{\varepsilon(r_i)+\varepsilon(r_{i-1})} & \text{if } i\neq 0\\ 0 \quad \text{otherwise}\end{cases}$$

Dirichlet boundary condition

V_i term:

$$\frac{-2}{\Delta r^2}-\frac{1}{\Delta r^2}\cdot\frac{\varepsilon(r_{i+1})-\varepsilon(r_i)}{\varepsilon(r_{i+1})+\varepsilon(r_i)}-\frac{1}{\Delta r^2}\cdot\frac{\varepsilon(r_i)-\varepsilon(r_{i-1})}{\varepsilon(r_i)+\varepsilon(r_{i-1})}+k_0{}^2\cdot\varepsilon(r_i)-\frac{l^2}{(r_i)^2}$$

V_{i+1} term:

$$\begin{cases}\dfrac{1}{\Delta r^2}+\dfrac{1}{2\cdot r_i\cdot\Delta r}+\dfrac{1}{\Delta r^2}\cdot\dfrac{\varepsilon(r_{i+1})-\varepsilon(r_i)}{\varepsilon(r_{i+1})+\varepsilon(r_i)} & \text{if } i\neq i\_max\\ 0 \quad \text{otherwise}\end{cases}$$

Define the azimuthal mode order $l := 1$

The user needs to set the azimuthal mode number

$M :=$ for $i \in 0..i\_max$

$M_{i,i} \leftarrow 0$

for $j \in 0..i\_max$

$r_j \leftarrow r\_min + j\cdot\Delta r$

$$M_{j,j} \leftarrow M_{j,j}+\left[\frac{-2}{\Delta r^2}-\frac{1}{\Delta r^2}\cdot\frac{\varepsilon(r_j+\Delta r)-\varepsilon(r_j)}{\varepsilon(r_j+\Delta r)+\varepsilon(r_j)}-\frac{1}{\Delta r^2}\cdot\frac{\varepsilon(r_j)-\varepsilon(r_j-\Delta r)}{\varepsilon(r_j)+\varepsilon(r_j-\Delta r)}+k_0(\lambda_0)^2\cdot\varepsilon(r_j)\right.$$

$$M_{j,j-1} \leftarrow M_{j,j-1}+\frac{1}{\Delta r^2}-\frac{1}{2\cdot r_j\cdot\Delta r}-\frac{1}{\Delta r^2}\cdot\frac{\varepsilon(r_j)-\varepsilon(r_j-\Delta r)}{\varepsilon(r_j)+\varepsilon(r_j-\Delta r)} \quad \text{if } 1\le j\le i\_max$$

$$M_{j,j+1} \leftarrow M_{j,j+1}+\frac{1}{\Delta r^2}+\frac{1}{2\cdot r_j\cdot\Delta r}+\frac{1}{\Delta r^2}\cdot\frac{\varepsilon(r_j+\Delta r)-\varepsilon(r_j)}{\varepsilon(r_j+\Delta r)+\varepsilon(r_j)} \quad \text{if } 0\le j\le i\_max-1$$

M

$\lambda := \text{eigenvals}(M)$

$DIM := \text{rows}(\lambda)$

$$\beta := \left| \begin{array}{l} \text{for } i \in 0..DIM-1 \\ \quad \beta_i \leftarrow 0 \\ \text{for } i \in 0..DIM-1 \\ \quad \beta_i \leftarrow \beta_i + \max\left(\sqrt{\lambda_i}\right) \text{ if } Im\left(\lambda_i\right) = 0 \wedge Re\left(\lambda_i\right) \geq 0 \\ \beta \end{array} \right.$$

$\beta 1 := \text{reverse}(\text{sort}(\beta))$

$\beta 1_0 = 10.096$

$\max(\beta) = 10.096$

$n_{eff} := \dfrac{\max(\beta)}{k_0(\lambda_0)}$ $\quad n_{eff} = 1.36574$

$f_0(x) := 1.424118 - 0.000006 \cdot (x - 850)$

$f_1(x) := 1.417623 - 0.000014 \cdot (x - 850)$

$f(q,x) := \dfrac{q \cdot x}{12 \cdot 10^3 \cdot 2}$

$\beta 1 =$

	0
0	10.096
1	9.981
2	9.917
3	9.822
4	9.821
5	9.8
6	...

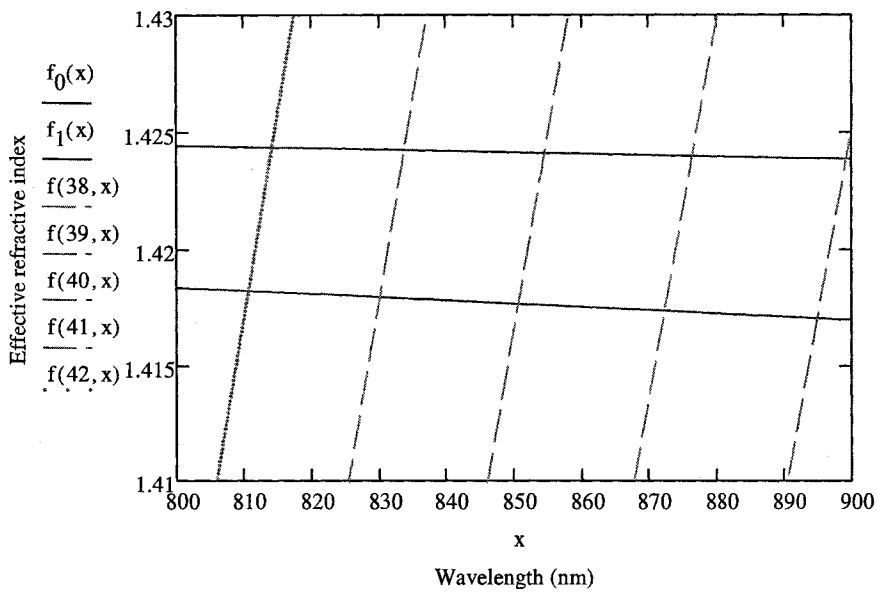

Figure E.5 Effective refractive indices of confined modes calculated by solving the Hemholtz wave equation using the finite difference method (code written by Linda).

E.3 Numerical mode solver by Dr. Lear

$a := R$ $\quad n_r(r) := n_{cav2}(r)$ $\quad \nu := 1$ $\quad k_0 := \dfrac{2 \cdot \pi}{\lambda_0}$

solve it using r as the coordinate. The equation to be solved is

$$\frac{d^2}{dr^2} f_r(r) + \frac{1}{r}\cdot\frac{d}{dr} f_r(r) + n(r)^2\cdot k_0^{\,2}\cdot f_r(r) + \frac{-\nu^2}{r^2}\cdot f_r(r) = k_z^{\,2}\cdot f_r(r)$$

Now set up the grid: $r_{max} := 4a$ grid_pts := 200 (this is really one less than # of points)

$$\Delta r := \frac{r_{max}}{grid\_pts} \qquad i := 0..grid\_pts \qquad r_i := (i+1)\cdot\Delta r$$

Now start loading the matrix — can't start from i=0 since can't include r=0 or else have div/0

Diagonal term of eqn 55 not including the 2nd derivative operator:

$$C_i := n_r(r_i)^2\cdot k_0^{\,2} - \left(\frac{\nu}{r_i}\right)^2$$

The differential operators are discretized as

$$\frac{d^2}{dr^2} f_r(r) + \frac{1}{r}\cdot\frac{d}{dr} f_r(r) = \frac{-2\cdot f_i + f_{i+1} + f_{i-1}}{\Delta r^2} + \frac{f_{i+1} - f_{i-1}}{r_i\cdot 2\cdot\Delta r}$$

Could use 2nd order difference if this is better (makes M 5-diagonal).

$$A_{i,i} := \frac{-2}{\Delta r^2} + C_i$$

$j := 0..(grid\_pts - 1)$

$$A_{j,j+1} := \frac{1}{\Delta r^2} + \frac{1}{r_j\cdot 2\cdot\Delta r} \qquad A_{j+1,j} := \frac{1}{\Delta r^2} - \frac{1}{r_{j+1}\cdot 2\cdot\Delta r}$$

We will ignore the large r boundary condition since we expect an attenuated solution ther For r=0, the boundary condition depends on n. If n=0, then df/dr=0. Thus f[i-1]=2f[i]-f[i+1]. Also, (1/r)(df/dr)=(f[1]-f[0])/(r[0.5]Dr) would have about the same value it would have at the next grid point. Thus add a term to A[0,0] and A[0,1].

$$A_{0,0} := A_{0,0} + (\nu = 0)\cdot\left(\frac{2}{\Delta r^2} - \frac{1}{\Delta r\cdot 0.5\cdot r_0}\right)$$

Yes I realize this does nothing. $\nu = 0 \rightarrow 0$ It is here for documentation.

$$A_{0,1} := A_{0,1} + (\nu = 0)\cdot\left(\frac{-1}{\Delta r^2} - \frac{1}{r_0\cdot 2\cdot\Delta r} + \frac{1}{\Delta r\cdot 0.5\cdot r_0}\right)$$

$\lambda := reverse(sort(eigenvals(A)))$

$\lambda =$

	0
0	100.637
1	96.791
2	96.416
3	95.87
4	95.051
5	93.982
6	...

The maximum eigenvalue is the fundamental

$\max(\lambda) = 100.637$ $\quad \lambda\_to\_plot\_index := 0$

$V := eigenvec(A, \lambda_{\lambda\_to\_plot\_index})$

$Vnorm := V \cdot \frac{1}{\max(|\overrightarrow{V}|)}$ $\quad k_z := \sqrt{\lambda_{\lambda\_to\_plot\_index}}$

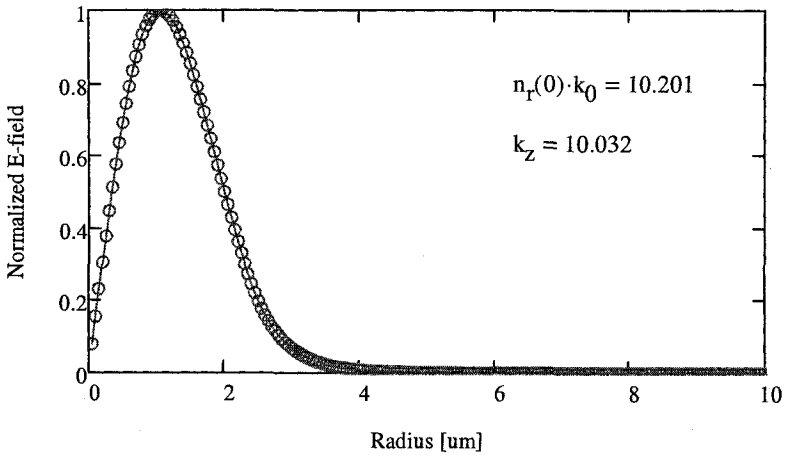

Figure E.6 Mode profile calculated by solving the Hemholtz wave equation using the finite difference method (code written by Dr. Lear).

Appendix F

Photomask design with FREEHAND

This appendix provides guidance for designing photomasks using the commercial software package, MICROMEDIA FREEHAND. Two types of photomasks, plastic transparency masks and chromium glass masks, can be used for fabricating microfluidic devices developed in this dissertation. The major differences between plastic and glass photomasks are the resolution and prices. Section G. 1 and G.2 summarize the features of the two printing services used by this work. Section G. 3 provides detailed mask design procedures using FREEHAND.

G.1 Printing service at the old Fort Collins high school

- ✓ Feature size and price
  - Feature size $\geq 50\mu m$
  - Printer resolution:1200 dpi (dots per inch)
  - $10 for an A4 sized transparency sheet
- ✓ Acceptable file format
  - PDF or EPS (enhanced post script), PDF is more convenient for the printing service center staff.
  - How to convert your design into PDF format?
    - Depends on the software packages used for the design. You may design your photomasks with LASI, L-Edit, or Micromedia Freehand.
    - In Freehand 10, please choose Export → PDF file

G.2 Printing service at Photoplot Store in Colorado Springs

✓ Features sizes and prices

- Feature sizes ≥ 12 μm features ($50 on A4 sized transparency sheet)
- Feature sizes ≥ 12 μm features ($80 on glass substrates)
- More pricing info is available on www.photoplotstore.com. Price varies with mask type, resolution, soda lime size/thickness, etc.

G. 3 Mask design using FREEHAND

Since the minimum feature size for the microfluidic devices, e.g. the dielectrophoretic (DEP) traps, is ~10 μm, Freehand was used in designing the photomasks used in this work. This section provides the detailed design procedures for using this commercial software package. Trial version of FREEHAND 10 with one month temporary license was used for our designs.

- Choose the size of the masks. Squares can be used to divide the A4 transparency into different areas, which may be labeled for different purposes. For example, lift-off mask, etching mask, and DEP trap designs. Figure G.1 shows the dimension of the mask holders of the Karl Suss mask aligner in the CSU cleanroom. The user may design their masks based on their own applications.

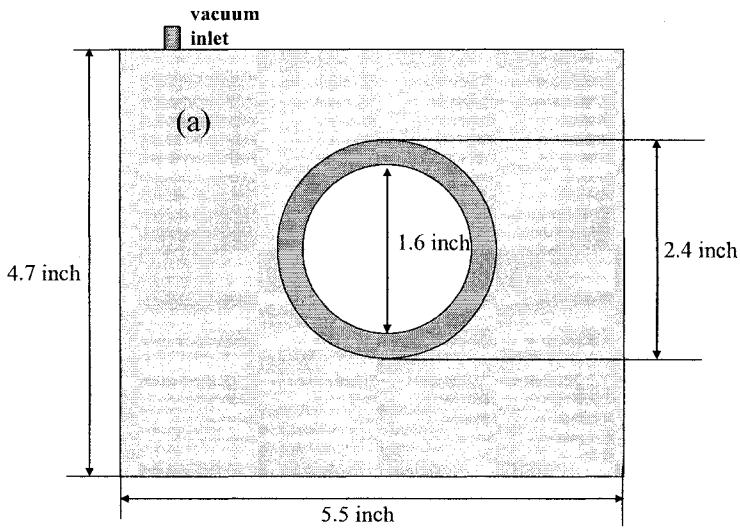

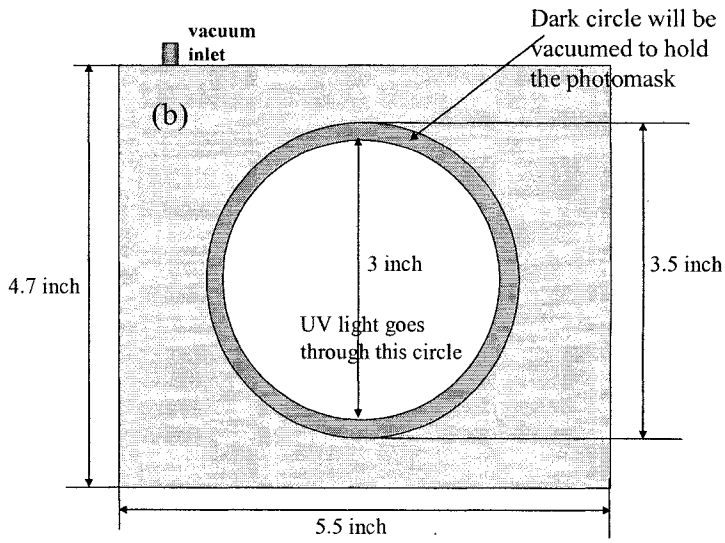

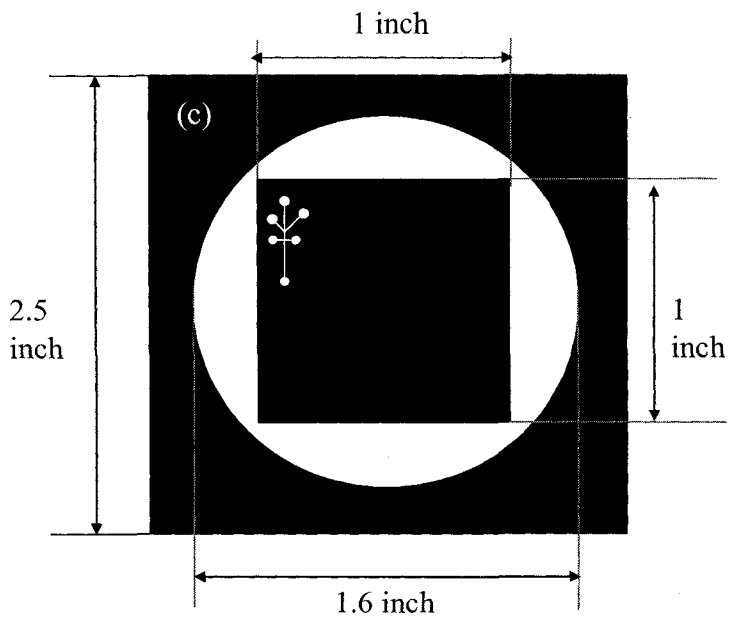

Figure G.1 Geometric dimensions of the (a) small and (b) large mask holders of the Karl Suss mask aligner in the CSU cleanrrom; (c) Example of a photomask compatible with the mask holder shown in (a).

- Set design grids in the bottom-left window. 0.001 mm grid size is used for design the DEP masks. Toggle through different grid sizes are helpful for designing masks that contain both big features (> 50 μm) and small features (~10 μm).
- Layout basic structures, for example, rectangles and circles through the drawing tool bar on the left the design window. Feature dimension can be changed in feature setting window on the right hand side of the layout window. Attention needs to be paid for proper setting the strobe line width for features such as rectangles and circles. Try setting the line width to be as small as possible. For example, drawing a 200 μm wide microfluidic channels can be done by either drawing a 200 μm rectangle with almost zero strobe line width or draw a 200 μm wide line.

- The fill-in color can be set within the feature setting window as well. Please choose solid black or white for corresponding areas of the masks.
- Since minimum grid size of FREEHAND is 1μm, designing masks that require accurate alignment is difficult. LASI provides multilayer mask design functions that are more convenient than FREEHAND. However, "Copy" and "Paste" may make things a little easier.
- Turning on the ruler will also help position the features at the desired locations. For example, setting the DEP square traps 500 μm away from each other could be done by shifting a copy of the 1st trap to ($x_1 \pm 100\ \mu$m, $y_1 \pm 100\ \mu$m) in the feature setting window with the help the ruler.
- Features are allowed to overlap with each other and the printed version is exactly what you seen on the layout window.
- Suitable labels for each portions of the photomask are highly recommended to help keep track of previous design and reduce the mistakes of applying the wrong photomasks during the photolithographic process.